# 4. PLASMA PHYSICS AND ENGINEERING

F. Najmabadi, C. G. Bathki, Y. Y. Chu, R. W. Conn,
P. I. H. Cooke, C. E. Kessel, R. A. Krakowski, R. L. Miller,
R. A. Nebel, and K. A. Werley

CONTENTS

# 4. PLASMA PHYSICS AND ENGINEERING

## 4.1. INTRODUCTION

The objectives of the fusion-core physics effort is to identify and study fusion-core plasma physics parameters of the TITAN RFP reactor, to develop operational scenarios (e.g., start-up, burn), to analyze the fusion-core plasma behavior and performance (e.g., equilibrium and stability, transport), and to study key plasma support subsystems (e.g., current drive, fueling, impurity control and particle exhaust system). As a whole, the fusion-core physics activity provides a detailed description of the fusion core for all engineering activities and design efforts. Feedback is also provided to the system analysis activity to improve parametric system models which are then used to generate new, cost-optimized "strawman" designs for further conceptual engineering design.

This activity starts with the TITAN "strawman" designs, given in Table 4.1.-I, which are provided by the parametric system analysis (Sec. 5). Then, magnetic calculations produce a realistic design for magnet coil sets needed for confinement, equilibrium, and start-up of the fusion core. Also, fusion-core plasma/circuit simulations result in detailed evaluation of key plasma parameters. These data are used to study and design the plasma support subsystems.

In this section, the work of the fusion-core physics activity during the scoping phase of the TITAN study is presented. Because of its impact on the design, the impurity-control and particle-exhaust subsystem is discussed in a separate section (Sec. 6). The theoretical and experimental principles of the RFP confinement scheme are presented in Sec. 4.2 and 4.3, respectively.

Section 4.4 contains the magnet configuration analysis. The design of the Oscillating-Field Current Drive (OFCD) coil set and that of the divertor coil set are not finalized and await engineering analysis of the design point as suggested by the work performed to date. At this time, two options for the toroidal-field (TF) coil set are pursued: (a) normal copper TF coils and (b) the integrated blanket-coil (IBC) concept. The poloidal-field (PF) coil set features normal copper ohmic-heating (OH) coils and superconducting equilibrium-field (EF) coils.

The fusion core simulation effort is discussed in Sec. 4.5. Strong emphasis is placed on the question of plasma start-up from gas breakdown and RFP

TABLE 4.1.-I

SUMMARY OF 1000-MWe TITAN STRAWMAN DESIGN-POINT

| | |
|---|---|
| Neutron Wall Loading, $I_w(MW/m^2)$ | 18.1 |
| First-wall minor radius, $r_w(m)$ | 0.65 |
| Plasma minor radius, $r_p(m)$ | 0.60 |
| Plasma major radius, $R_T(m)$ | 3.90 |
| Plasma volume, $V_p(m^3)$ | 27.7 |
| Plasma density, $n(10^{20}/m^3)$ | 4.35 |
| Plasma temperature, T(keV) | 20.0 |
| Poloidal beta, $\beta_\Theta$ | 0.20 |
| Plasma current, $I_\phi(MA)$ | 17.75 |
| Toroidal current density, $j_\phi(MA/m^2)$ | 15.7 |
| Energy confinement time, $\tau_E(s)$ | 0.25 |
| Thermal diffusivity, $\chi_E(m^2/s)$ | 0.27 |
| Pinch Parameter, $\Theta$ | 1.55 |
| Reversal parameter, F | -0.10 |
| Poloidal field at plasma surface, $B_\Theta(T)$ | 5.2 |
| Reversed-toroidal field during burn, $-B_{\phi R}(T)$ | 0.36 |
| Fusion power density, $P_F/V_p(MW/m^3)$ | 81.6 |
| Plasma ohmic dissipation, $P_\Omega(MW)$ | 8.0 |
| Engineering Q-value, $Q_E = 1/\varepsilon$ | 7.84 |
| Fusion power, $P_F(MW)$ | 2,261.0 |
| Total thermal power, $P_{TH}(MW)$ | 2,866.0 |
| System power density, $P_{TH}/V_{FPC}(MWt/m^3)$ | 12.8 |
| Mass power density, $1000P_E/M_{FPC}$ = MPD(kWe/tonne) | 644.0 |
| Cost of electricity, COE(mills/kWeh) | 35.2 |

formation leading to the slow current ramp phase and eventually a steady state burn. It is found that the TF and PF coil design limits are more affected by the plasma breakdown, RFP formation, and subsequent current-ramp transients than by the steady-state burn phase. Furthermore, the desire to eliminate on-site power supplies for start-up and use the power grid for this purpose strongly impact the start-up sequence. Section 4.5 discusses these tradeoffs in detail.

A current-drive system is required for steady-state operation. Various options for this system are discussed in Sec. 4.6. The primary current-drive

option for the TITAN design is based on the OFCD scheme. The circuit modeling and simulation effort used to guide the OFCD design is also presented.

One-dimensional fusion-core simulations are also performed to supplement the zero-dimensional simulations in order to examine 1-D aspects of local transport assumptions, impurity radiation with beta limits, pellet fueling, RFP dynamo, and current drive. These 1-D simulations are also coupled to edge-plasma models (described in Sec. 6) to provide a self-consistent picture of edge-plasma/core-plasma interface. These 1-D simulations are included in Sec. 4.7.

Conclusions of the fusion-core physics activities during the first phase of the TITAN program, as well as the future directions, are discussed in Sec. 4.8.

## 4.2. RFP THEORY

The theoretical principles and understanding of RFP confinement scheme are described in this section. Those features that are relevant to a fusion reactor are emphasized. The experimental data base is summarized in Sec. 4.3. A more detailed description of the RFP confinement concept is given in Ref. 1 and references contained therein.

The RFP, like tokamak, belongs to a class of axisymmetric, toroidal confinement systems that utilizes both toroidal ($B_\phi$) and poloidal ($B_\theta$) magnetic fields to confine the plasma. In the tokamak, stability is provided by a strong toroidal field ($B_\phi >> B_\theta$) such that the safety factor exceeds unity, that is, $q > 1$. Here, q is defined as $q(r) \equiv rB_\phi/R_T B_\theta$, and $R_T$ and $r_p$ are respectively, the major and minor radii of the plasma. In the RFP, on the other hand, strong magnetic shear produced by the radially varying (and decreasing) toroidal field stabilizes the plasma with $q < 1$ and relatively modest $B_\phi$. Theoretically, an electrically conducting shell surrounding the plasma is required to stabilize the long-wave-length MHD modes. In both the RFP and tokamak, equilibrium may be provided by either an externally produced vertical field, a conducting toroidal shell, or a combination of both. Figures 4.2.-1.a, b, and c respectively show, the radial variation of the poloidal and toroidal field and also the safety factor for tokamaks and RFPs.

The RFP relies strongly on the poloidal field generated by the current in the plasma. This feature has several reactor-relevant advantages. The poloidal field decreases inversely with the plasma radius outside the plasma. The toroidal field is also rather weak outside the plasma. The magnetic field

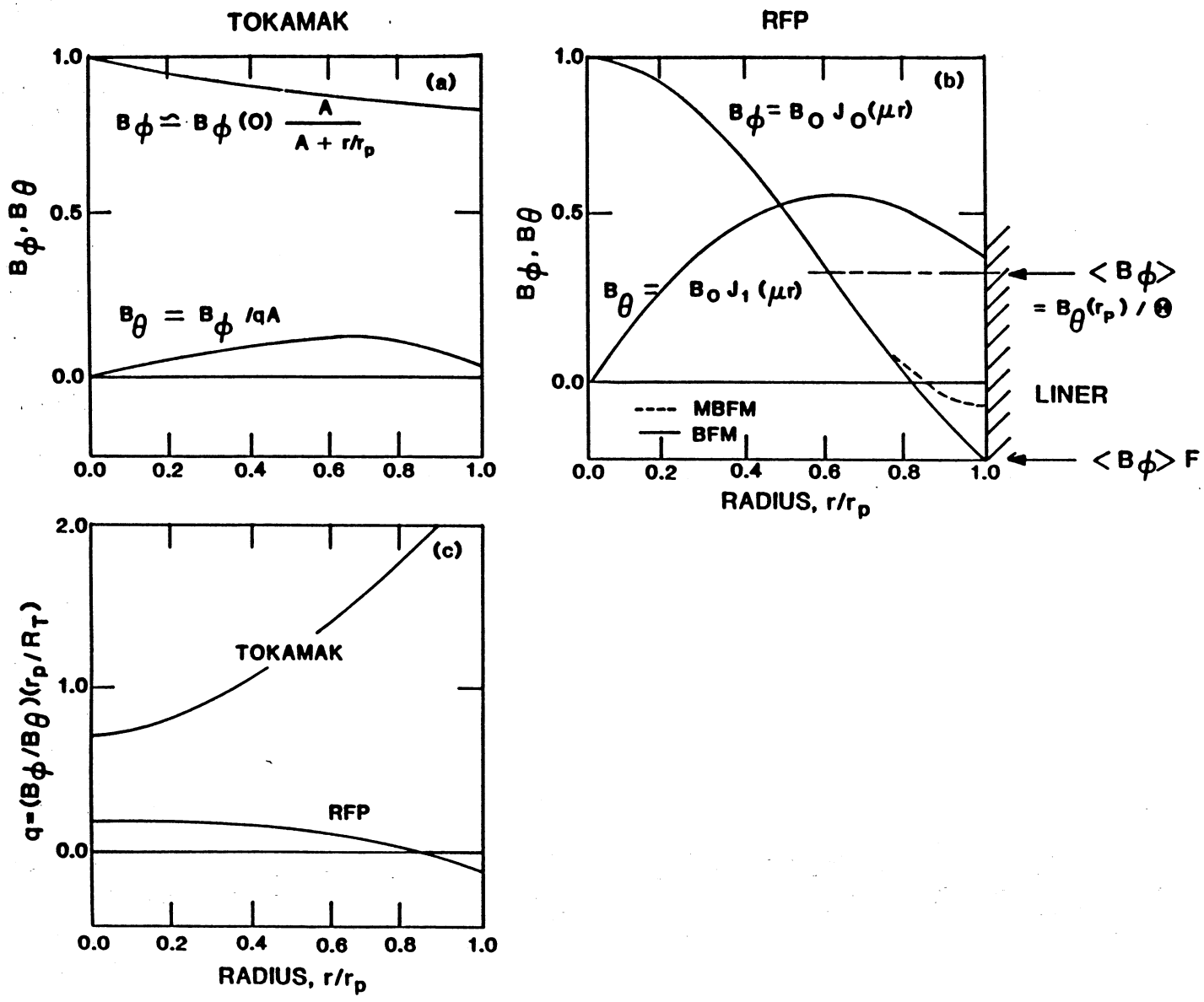


Fig. 4.2.-1. Magnetic field distribution for tokamak (a) and RFP (b) and the q profiles for tokamak and RFP (c).

strength at the external conductors, therefore, is small, resulting in a high engineering beta (defined as the ratio of the plasma pressure to the magnetic field pressure at the magnets). Low-current-density, less-massive, and resistive coils are possible. Also, the RFP can operate at high total beta. The experimentally measured beta values are in the range 10% to 20%, which is the range used in reactor studies. Further, the RFP relies on the magnetic shear to stabilize the plasma. Thus, it can operate with a large ratio of plasma current to toroidal field, and stability constraints on the aspect ratio, $R_T/r_p$, are removed. The choice of the aspect ratio can be made solely on the basis of engineering constraints. High-current-density operation and ohmic heating to ignition are possible.

The fundamental property of the RFP is that the field configuration and toroidal-field reversal is the result of the relaxation of the plasma to a minimum-energy state. Taylor's theory of relaxed states [2,3] postulates that all pinch configurations will relax to a state determined by minimizing the magnetic energy subject to some constraints on allowed motion or magnetic field variation. Taylor then considers the relaxation of a plasma with small but finite resistivity in a flux conserving cylinder, subject to the invariance of the magnetic helicity, $K \equiv \int \vec{A} \cdot \vec{B}\, dV$ where $\vec{B} \equiv \nabla \times \vec{A}$. The relaxed state was found to be force-free and described by $\nabla \times \vec{B} = \mu\vec{B}$, where $\mu$ is uniform across the plasma. The solution to this equation in cylindrical geometry gives the "Bessel-Function Model" (BFM), with $B_\phi \propto J_0(\mu r)$ and $B_\theta \propto J_1(\mu r)$ where $J_0$ and $J_1$ are the Bessel functions of the first kind. These relaxed states can be described by the dimensionless quantities, the pinch parameter, $\Theta$, and the reversal parameter, F:

$$\Theta \equiv \frac{B_\theta(r_p)}{\langle B_\phi \rangle} , \qquad (4.2.-1)$$

$$F \equiv \frac{B_\phi(r_p)}{\langle B_\phi \rangle} , \qquad (4.2.-2)$$

where $\langle B_\phi \rangle$ is the average toroidal field,

$$\langle B_\phi \rangle = \frac{2}{r_p^2} \int_0^{r_p} B_\phi(r)\, r\, dr. \qquad (4.2.-3)$$

The locus of relaxed states then form a curve in F-Θ space as shown in Fig. 4.2.-2 (labeled as BFM). In the same figure, the corresponding experimental data are also shown. These data lie to the right of the curve predicted by Taylor's BFM model. These experimental equilibria differ from Taylor's model, since plasma has finite pressure, μ is not uniform across the plasma, and a perfectly conducting wall is not used. Thus, they represent "near-minimum-energy" states. However, Taylor's concept of a preferred locus of relaxed states in F-Θ space remains valid.

The theory of relaxed states has several important consequences. First, the theory predicts that the relaxed states depend only on the pinch parameter, Θ, and these states are independent of initial conditions provided that time scale is sufficiently large for the relaxation process to take place. Second, if the current and toroidal flux are maintained constant in time (i.e., constant Θ) then, the relaxed state equilibrium will be sustained. Experimentally, RFPs are observed to exist for times much larger than the resistive decay time of the field profile. This process involves continuous generation of toroidal field within the plasma, often called the RFP "dynamo", to compensate for the resistive decay of the toroidal field and maintains the field profile.

Finally, the F-Θ relationship implies a strong coupling between the toroidal and poloidal fields; the toroidal field can be generated by driving toroidal current with external poloidal-field circuits. Indeed, such a relaxation-assisted plasma current ramp is used in experiments and is envisioned for RFP reactors. Furthermore, the strong coupling of the poloidal and toroidal fields also offers the possibility of a steady-state current drive system through the "helicity injection" technique. Current drive through "electrostatic" helicity injection has been experimentally demonstrated in spheromaks [4], which is also a relaxed-state system. Another helicity injection technique is the Oscillating-Field Current Drive (OFCD). In this scheme, oscillating voltages are applied to the toroidal and poloidal circuits in the appropriate phase to drive a DC toroidal current in the plasma with the plasma in effect behaving as a nonlinear rectifier. The experiments on OFCD are yet not conclusive but are encouraging [5,6]. Helicity injection techniques are discussed in more detail in Sec 4.6.

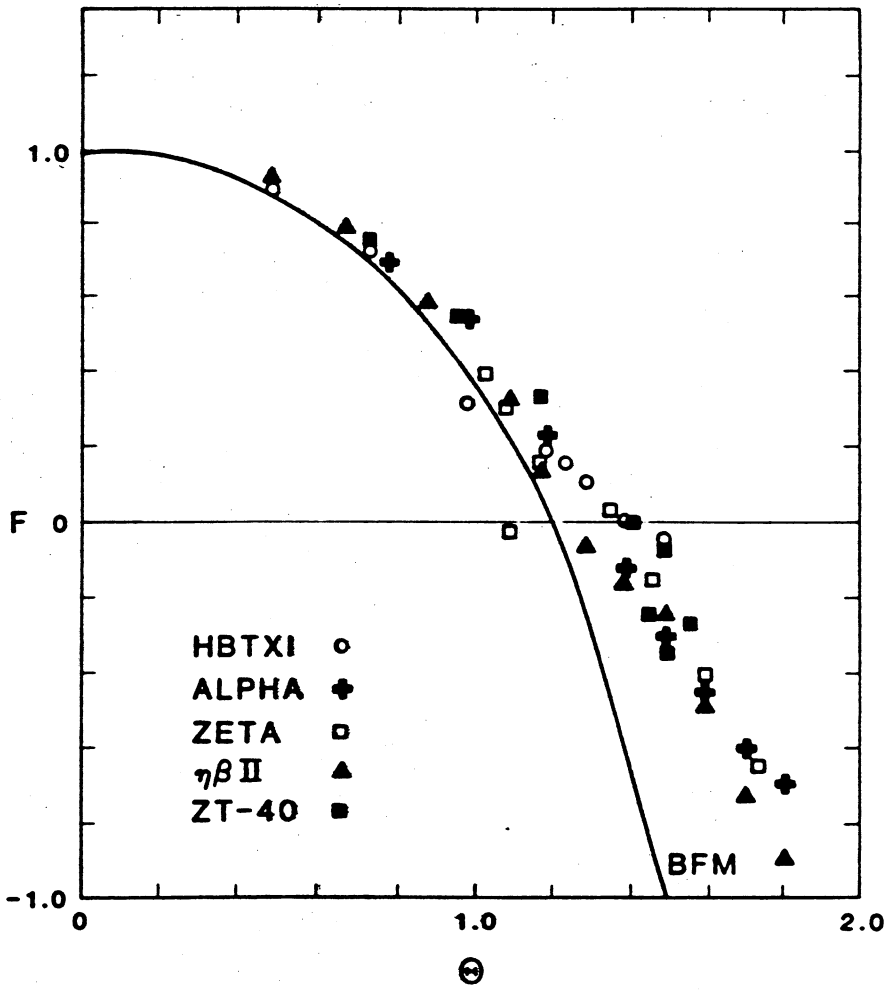


Fig. 4.2.-2. Locus of operating points on the F-Θ diagram. The solid line (BFM) is the curve predicted by Taylor's theory and the data points are from several RFP experiments.

4.2.1. Equilibrium

The analysis of equilibrium and stability in RFPs usually invoke the high-aspect-ratio (straight cylinder) approximation. Such a model encompasses z-pinches ($q = 0$), $\Theta$ pinches ($q \to \infty$), large-aspect-ratio tokamaks ($q > 1$) and RFPs ($q < 1$). The radial pressure balance in the screw pinch is described by

$$\frac{d}{dr}\left[ p + \frac{B_\Theta^2 + B_\phi^2}{2\mu_0} \right] + \frac{B_\Theta^2}{\mu_0 r} = 0 \ , \qquad (4.2.-4)$$

where p is the plasma pressure and $\mu_0$ is the permeability of free space. This equilibrium pressure balance is then subjected to stability analysis via the energy principle [7] or normal-mode technique.

In principle, some information on the current and pressure profiles is required to find the equilibrium magnetic field profiles. Because of the strong tendency for RFPs to relax, the field distributions obtained in modern experiments are near-minimum-energy states. The theory of relaxed states predicts the condition, $\nabla \times \vec{B} = \mu\vec{B}$ with $\mu \equiv \mu_0 j_{||}/B$ spatially uniform across the plasma, leading to BFM field profiles. However, a constant $\mu$ (or constant $j_{||}/B$) implies large parallel current density near the wall in a region of cold, resistive plasma. A $\mu$ profile that is nearly constant over the bulk of the plasma, and decreases in the outer region to match the practical $\mu(r_p) \simeq 0$ condition eliminates the unphysical features of the BFM. Examples are $\mu/\mu(0) = 1 - (r/r_p)^8$ or a $\mu$ profile which is constant for $r < r_r$ (the radius of reversal surface) and decreases uniformly to zero at $r_p$.

For a toroidal system, equilibrium also requires the compensation of the outward force from the plasma pressure and the plasma current (poloidal field pressure). Either a perfectly conducting wall, or a vertical field produced by the external circuits, or a combination of both, is necessary for equilibrium. The required value of this vertical field is given by Shafranov [8]

$$B_v = \frac{\mu_0 I_\phi}{4\pi R}\left[ \ln\left(\frac{8R_T}{r_p}\right) + \beta_\Theta + \frac{l_i}{2} - 1.5 \right], \qquad (4.2.-5)$$

where $l_i$ is the plasma internal inductance per unit length.

It follows from the static ideal MHD equations,

$$\nabla p = \vec{J} \times \vec{B} \ , \tag{4.2.-6}$$

$$\nabla \times \vec{B} = \mu_0 \vec{J} \ , \tag{4.2.-7}$$

$$\nabla \cdot \vec{B} = 0 \ , \tag{4.2.-8}$$

that the current and the magnetic field lines lie on constant plasma pressure surfaces. For axisymmetric, toroidal, current carrying plasma, the equilibrium consists of toroidal flux surfaces, nested about a magnetic axis. Each surface is generated by helical field lines. If the toroidal symmetry is violated, for example because of errors in magnet coils, the ideal nested toroidal surfaces break up and a more complicated structure emerges which includes helical magnetic islands. The existence and interaction of these islands are believed to have an important impact on plasma transport. Although both tokamaks and RFPs are susceptible to magnetic island formation, the number and location of the resonant flux surfaces is significantly different in the two concepts, making field errors a greater concern in RFPs.

### 4.2.2. Stability

The Suydam criterion [9] gives a necessary condition for stability against ideal MHD pressure-driven modes for a straight cylinder.

$$\frac{r}{4}\left(\frac{1}{q}\frac{dq}{dr}\right)^2 + \frac{2\mu_0}{B_\phi^2}\frac{dp}{dr} > 0 \ , \tag{4.2.-9}$$

where q(r) is a relative measure of field line pitch at position r. This criterion simply states that the negative pressure gradient associated with the confinement of a hot plasma has a destabilizing effect and can be compensated only by a sufficiently large radial variation in the field line pitch (i.e., large magnetic shear).

By including first-order toroidal effects, Eq. (4.2.-9) becomes the Mercier criterion [10].

$$\frac{r}{4}\left(\frac{1}{q}\frac{dq}{dr}\right)^2 + \frac{2\mu_0}{B_\phi^2}\frac{dp}{dr}(1 - q^2) > 0 \ , \qquad (4.2.-10)$$

which shows that if $q(r) > 1$ everywhere, the system is stable even without the magnetic shear. This is the primary approach to stability used in the tokamak. Physically, the $q > 1$ condition forces the wave length of potentially unstable $m = 1$ kink mode to exceed the major circumference of the torus ($2\pi R_T$). In RFPs, $q < 1$ and RFPs must operate with sufficient shear to satisfy the Mercier criterion. Moreover, a pitch minimum, $dq/dr = 0$, should be avoided within the plasma.

Necessary conditions for stability against ideal MHD current-driven modes have been derived by Robinson [11] on the basis of the energy principle [7]. The necessary condition is found to be $|P(r_w)| < 3P(0)$, where the pitch is $P(r) \equiv rB_\phi(r)/B_\theta(r) = Rq(r)$ and $r_w$ is the location of the conducting wall. This can be written approximately as

$$\left(\frac{r_w}{a}\right)^2 < 3 \left| \frac{B_\phi(0)}{B_\phi(r_w)} \right| \ , \qquad (4.2.-11a)$$

$$\Phi > 0 \ , \qquad (4.2.-11b)$$

where $\Phi$ is the total toroidal flux inside the conducting wall. These conditions require both the amplitude and the region of the field reversal not to be large: the conducting wall should be close to the plasma to stabilize current driven modes. Furthermore, stability against current-driven modes also requires that no pitch minimum occurs in the plasma.

The above conditions are usually well satisfied for experimental profiles and are also satisfied for the profiles calculated for TITAN design. The above necessary conditions (4.2.-11) are in practice close to being sufficient. Based on ideal MHD theory, therefore, RFP profiles are possible with plasma beta as high as 0.3. Note that Taylor's theory predicts that all states on the F-$\Theta$ diagram including those with $F > 0$ and no field reversal are near-minimum-energy states and, therefore, are stable. However, profiles with no reversal exhibit a pitch minimum within the plasma and are unstable to both ideal MHD pressure-driven and current-driven modes. This conclusion is confirmed

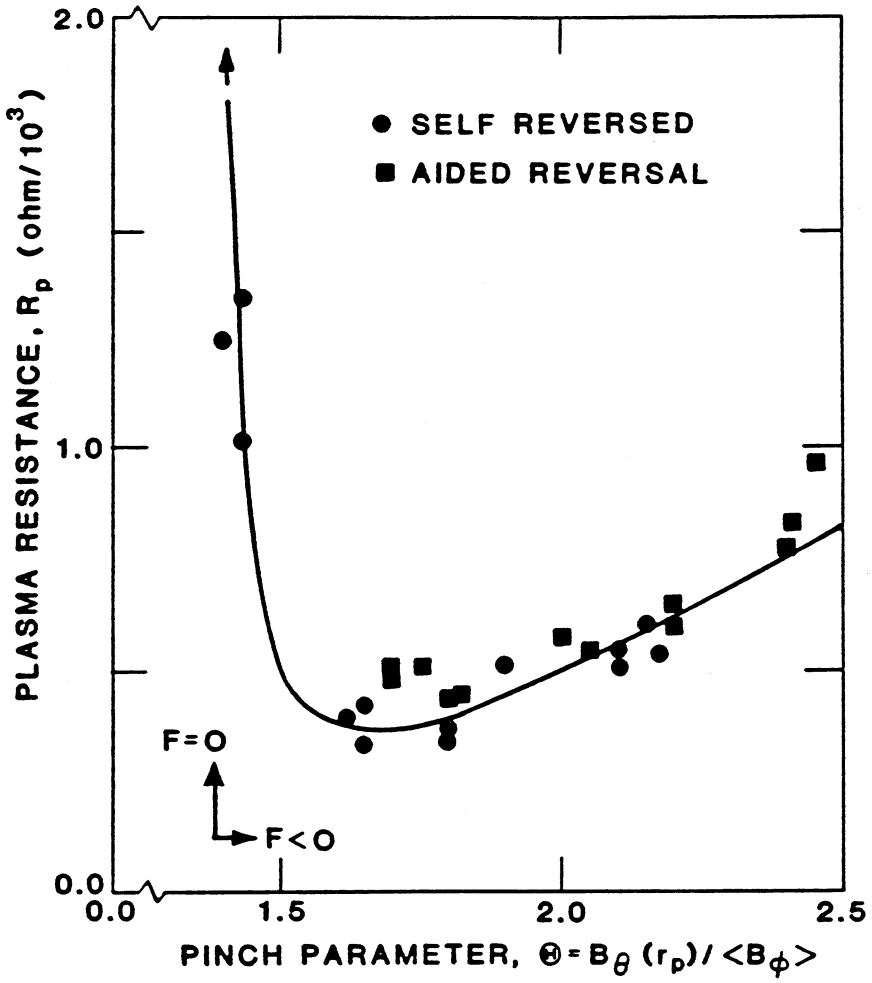


Fig. 4.2.-3. Plasma resistance as a function of the pinch parameter, Θ (HBTX1A).

experimentally and is shown in Fig. 4.2.-3, which shows the plasma resistance as a measure of the confinement as a function of the pinch parameter, $\Theta$. It is seen that as $\Theta$ increases, the resistance falls dramatically, particularly as $\Theta$ exceeds the value where the field reversal occurs [12].

In the ideal-MHD model, the plasma is assumed to have zero resistivity. This assumption constrains magnetic field lines to be "frozen" in the plasma and thus limits the class of potentially unstable modes. Resistive-MHD stability analysis has to be performed to provide a more realistic picture of the plasma behavior. In general, the criteria for resistive stability are more stringent, and a closer fitting conducting wall and a lower $\beta$ are required. Detailed analysis of current-driven resistive tearing modes has been made [13] and stable RFP configurations have been found with $\beta \simeq 0.2$. These configurations have been found, however, to be unstable to the so-called resistive g-modes. Moreover, analyses show that resistive g-modes can become unstable for pressure gradients substantially smaller than those that can drive ideal-MHD instabilities. These resistive g-modes are localized and may ultimately affect the confinement. In fact, some theoretical estimates of the energy confinement time have been proposed that are based on transport along stochastic field lines created by resistive g-mode turbulence [14] (see Sec. 4.2.4).

### 4.2.3. Relaxation and Sustainment

The theory of relaxed states has been extremely successful in predicting the behavior of RFPs and the characteristics of the F-$\Theta$ diagram. The details of the relaxation process to the near-minimum-energy states are neither invoked nor required in this theory. These details, however, are required to understand the relaxation, sustainment, stability, transport, and their relationship in RFPs.

Of particular interest is to account for RFP sustainment. Consider a cylindrically-symmetric, resistive plasma (even with anisotropic resistivity) with field-reversed profiles. According to the Ohm's law, there should be a poloidal electric field corresponding to the poloidal current at the reversal point. To sustain this resistive electric field, Faraday's law requires a resistive decay of the toroidal flux inside the reversal radius. Reversed-field pinch discharges, however, are maintained for times far longer than the resistive diffusion time. Some mechanism is necessary to drive the poloidal current at the plasma surface, canceling the resistive electric field there. This mechanism, the so-called "dynamo", generates the magnetic field that opposes the resistive field diffusion.

Several mechanisms for toroidal flux regeneration have been proposed, each offering a different explanation for the origin of the poloidal current at the reversal surface. For example, second-order effects of low-level MHD fluctuations resulting from nonlinear evolution of resistive MHD modes can drive a sufficient poloidal current at the reversal surface to sustain the field reversal [15]. Alternatively, a plasma model with stochastic field lines is proposed, wherein a global rather than a local Ohm's law applies and the poloidal current at the reversal surface can be driven by electromagnetic fields originating elsewhere in the plasma [16-18].

In summary, quasi-stationary RFP equilibria are sustained through continuous relaxation and field generation. These time-averaged equilibria are stable to ideal and resistive-tearing modes, because the relaxation process acts to maintain the stability. Relaxation and field-generation processes are driven continuously by a complex spectrum of resistive modes and their nonlinear interaction. These processes also involve field-line reconnection and profile modification which can impact the cross-field transport. Therefore, the plasma confinement and $\beta$ are also affected by the relaxation process. The details of the mechanisms that drive the relaxation and dynamo activities in RFPs, however, remain unresolved.

### 4.2.4. Transport and Confinement

Some theoretical models for the transport in RFPs have been proposed. However, a detailed transport model is not yet available for RFPs, and the precise behavior of the energy confinement is unknown. One can use an empirical approach to evaluate present experimental results and form a basis for the extrapolation of these results to reactor regimes. Here, the details of the transport physics is not considered but rather, experimental observations are used to guide the theory. Starting with simple pressure balance, $p \propto \beta_\theta I_\phi^2/r_p^2$, one has

$$T = \frac{\mu_0}{16\pi k_B}\left[\frac{I_\phi}{N}\right]\beta_\theta I_\phi \ , \qquad (4.2.-12)$$

where $N = n\pi r_p^2$ is the plasma line-averaged density, T is the average ion temperature, and $k_B$ is the Boltzmann constant. First, Eq. (4.2.-12) predicts that $T/I_\phi \propto I_\phi/N$, a behavior which is observed experimentally. Second, the

plasma pressure in some devices is found to scale as $I_\phi^2$ over a wide range of parameters, indicating a constant $\beta_\theta$ operation. In fact, there is some experimental evidence that RFPs operate near a beta limit; energy transport and loss mechanisms in RFPs are self-adjusted to lose just enough plasma energy to maintain $\beta_\theta$ constant (Sec. 4.3.6). Equation (4.2.-12) then suggests that the temperature varies linearly with the current for a fixed $I_\phi/N$, as reported for a number of experiments. Note that the constant-beta assumption still remains an open question, since a strict linear relation between T and $I_\phi$ is not observed in all RFP experiments.

Next, using the definition of the energy confinement from the energy balance for a steady-state ohmically-heated discharge, and substituting from Eq. (4.2.-12) for T, one gets

$$\tau_E \equiv \frac{3\ n\ k\ T}{\eta\ j_\phi^2} = \frac{3}{16}\ \mu_0\ \beta_\theta\ r_p^2\ \sigma\ , \qquad (4.2.-13)$$

where $j_\phi \equiv I_\phi/\pi r_p^2$ and $\sigma = 1/\eta$ is the plasma electrical conductivity. The plasma resistance is observed to have classical temperature dependence, $\sigma \propto T_e^{3/2}$, on a number of RFP experiments over a wide range of parameters. Then, using the constant-beta assumption and linear dependence of T and $I_\phi$, the energy confinement time is found to scale with the plasma current, $\tau_E \propto I_\phi^{3/2} r_p^2$.

It is important to point out that in calculating the plasma resistance, geometrical effects (i.e., field-line pitch), impurities, and the anomalous resistance associated with the RFP dynamo must be considered. The dynamo represents an added dissipation of the currents driven by the dynamo electric field and, therefore, appears as an actual resistivity anomaly. In fact, the resistivity in RFP experiments in many conditions is observed to be close to the classical value, taking into account the geometrical and impurity effects. The dissipation associated with the dynamo effect is generally small and the ohmic power delivered to the plasma is not expected to exceed the classical predictions by a significant amount. However, at low densities (or high $I_\phi/N$) the resistance anomaly factor is too high to be explained by geometrical or impurity effects.

Some theories have been proposed which estimate the energy confinement time associated with the electron parallel transport along stochastic magnetic field lines caused by resistive-fluid turbulence. In one theory [14], resistive

g-mode turbulence has been considered. The diffusion coefficient for this case is found to scale as:

$$D \propto \eta\ (M/m)^{1/2}\ \beta_\theta^2\ , \qquad (4.2.-14)$$

where M and m are the ion and electron masses, respectively. Using this diffusion coefficient for ohmically heated discharges, the value of beta is found to be $\beta_\theta \simeq (m/M)^{1/6}$ and is independent of machine parameters (the factor 1/6 is a result of assuming a $J_0$ radial temperature profile). This, together with the pressure balance, results in a linear temperature-current scaling, as reported in a number of experiments.

In another theory [19], resistive tearing mode turbulence has been considered which results in another scaling, namely,

$$\beta_\theta \propto (I_\phi/N)^{-1/3}\ I_\phi^{-1/3}\ r_p^{-1/6}\ , \qquad (4.2.-15a)$$

$$T \propto (I_\phi/N)^{2/3}\ I_\phi^{2/3}\ r_p^{-1/6}. \qquad (4.2.-15b)$$

In still another theory based on current-driven drift-wave turbulence [20], the following scaling relationships are found:

$$\beta_\theta \propto (I_\phi/N)^{-1}\ I_\phi^{-1/7}\ r_p^{-2/7}\ , \qquad (4.2.-16a)$$

$$T \propto I_\phi^{6/7}\ r_p^{-2/7}\ , \qquad (4.2.-16b)$$

$$\tau_E \propto (I_\phi/N)^{-1}\ I_\phi^{8/7}\ r_p^{9/7}\ . \qquad (4.2.-16c)$$

This last theory predicts a weak dependence of plasma beta on machine parameters and almost linear temperature-current dependence. A better resolution of these

various theoretical predictions must await experiments with a broader range of plasma and machine parameters (e.g., plasma current, dimensions).

## 4.3. RFP EXPERIMENTS

The earliest milestone (1965) for the RFPs was the discovery of a period of improved stability and reduced turbulence (called quiescence) on the ZETA device [21]. This quiescent period observed in ZETA was preceded by a turbulent phase with large energy losses and strong plasma-wall interaction. Furthermore, self-reversal of the external toroidal field relative to the on-axis field was observed, but the importance of these observations was not appreciated at the time.

To reduce RFP formation losses, experimental RFPs during 1970s used fast magnetic-field programing, with typical rise-times of a few microseconds, to force the reversal externally. These experiments required electrically insulating discharge tubes to accommodate the high voltages needed for fast programming and operated on time scales of up to tens of microseconds. Many important advances in RFP physics were made in these machines.

With experience from fast-programing machines and a general theory of relaxed states in hand, modern RFP experiments in late 1970s and 1980s have moved back toward a slow rising plasma current (0.1-1.0 ms) and the facility for slow $B_\phi$ control to assist and optimize the self-reversal process and to minimize RFP formation losses. These machines use a metallic liner, are equipped with better vacuum systems, and have more accurate magnetic-field geometry. The first of these modern machines to operate was ETA-BETA-II at Padova [22-24] at 1979. Today, high-temperature plasmas are routinely produced in many intermediate-size machines such as TPE-1R(M) at ETL, Sakura-Mura [25,26], ZT-40M at Los Alamos [27-29], HBTX1A at Culham [30,31], and OHTE/RFP at GA Technologies [32,33]. General parameters of these experiments are listed in Table 4.3.-I. The design parameters of the TITAN reactor are also listed in that table for comparison.

The plasma parameters obtained in these experiments have been improving steadily. Values of $\beta_\theta$ in the range 0.1 to 0.2 are routinely achieved, which are adequate for a reactor. Electron temperatures in the range 0.4-0.6 keV, densities up to about $10^{20}$ $m^{-3}$, and energy confinement times of a few tenths of millisecond are typical of these intermediate-size experiments. Data from a number of machines indicate a linear temperature-current scaling, which suggest

TABLE 4.3.-I

COMPARISON OF TITAN DESIGN POINT TO KEY RFP EXPERIMENTS IN PRESENT OPERATION[a]

| Parameter | TPE-1R(M) | ETA-BETA-II | ZT-40M | OHTE-RFP | HBTX | TITAN |
|---|---|---|---|---|---|---|
| Laboratory | ETL (Japan) | Padova (Italy) | Los Alamos (USA) | GA Tech. (USA) | Culham (UK) | UCLA et al. (USA) |
| Major Radius, R (m) | 0.5 | 0.65 | 1.14 | 1.24 | 0.8 | 3.9 |
| Minor Radius, $r_p$ (m) | 0.09 | 0.125 | 0.20 | 0.20 | 0.26 | 0.6 |
| Maximum Current, $I_\phi$ (MA) | 0.15 | 0.25 | 0.45 | 0.50 | 0.30 | 17.7 ($\lesssim$ 10)[c] |
| Maximum Current Density, $j_\phi$ (MA/m$^2$) | 5.9 | 5.1 | 3.6 | 4.0 | 1.4 | 15.7 ($\lesssim$ 5)[c] |
| Pulse Risetime (ms) | 0.45 | 0.1-0.5 | 0.25-2.0 | 0.2-0.5 | 0.3-4.0 | 10,000. |
| Pulse Length (ms) | 0.8 | 1.0-2.0 | 5.0-37. | 5.0-10.0 | 5.0-14.0 | $\infty$ |
| Average Density, n ($10^{20}$/m$^3$) | 0.1-1.0 | 0.2-4.0 | 0.1-1.0 | 0.1-5.0 | 0.1-1.0 | 4.3 (< 4.) |
| On-axis Electron Temperature, $T_e(0)$ (keV) | 0.5-0.6 | 0.1-0.2 | 0.3-0.5 | 0.5 | 0.3-0.4 | 24.0 ($\lesssim$ 6.)[c] |
| Maximum Ion Temperature, $T_i$ (keV) | 0.5-0.6 | 0.1-0.2[b] | > $T_e(0)$ | > $T_e(0)$ | 0.3-0.4[b] | 24.0 ($\lesssim$ 6.)[c] |
| Poloidal Beta, $\beta_\theta$ | ~ 0.1 | ~ 0.1 | 0.1-0.2 | 0.1-0.3 | 0.1-0.2 | 0.20 ($\lesssim$ 0.05)[c] |
| Energy Confinement Time, $\tau_E$ (ms) | ~ 0.1 | ~ 0.1 | 0.3-0.7 | ~ 0.4 | 0.1-0.3 | 252 ($\sim$ 400)[c] |

[a] Values given in this table do not form a self-consistent set measured for any one condition, but instead describe a range of typical conditions.

[b] At maximum (peak) current.

[c] Titan design parameters during burn (at ignition).

$\tau_E \propto T_e^{3/2}$. Furthermore, both experimental and theoretical evidence suggests a strong scaling of $n\tau_E$ with the plasma current ($\tau_E \propto I_\phi^{5/2}$).

4.3.1. Start-up and RFP Formation

The time history of a typical RFP experimental discharge can be divided into three phases: the formation phase; the sustainment phase; and the termination phase. A representative time history of a RFP discharge is shown in Fig. 4.3.-1 (upper trace). The formation phase denotes the time from the start to the peak of the toroidal plasma current. The sequence of events during the formation phase begins by establishing a toroidal magnetic field inside the discharge chamber using the toroidal field coils in the absence of the plasma. At the time of peak toroidal magnetic field, poloidal-field windings are activated to produce a toroidal voltage around the discharge chamber. This voltage typically ionizes the gas in a few microseconds, and the toroidal current is initiated. As time proceeds the toroidal current increases, and toroidal magnetic field on the axis increases, while the toroidal magnetic field at the wall decreases, keeping the average toroidal field in the chamber almost constant. Eventually the toroidal magnetic field at the wall passes through zero, becomes reversed, and is crowbarred.

The discharge is then extended by using a passive crowbar on the poloidal circuits, which gives a decaying waveform, or an active (power) crowbar, which produces a flat-top current waveform as seen in Fig. 4.3.-1 (upper trace). Reversed-field pinch discharges normally experience an abrupt end when the plasma current decreases rapidly to zero. Accompanying this fast current "termination" is a positive pulse in the toroidal voltage at the liner, in contrast to the negative toroidal voltage spike that accompanies the disruption of the current in a tokamak indicating a difference in the flow of magnetic energy to or from the plasma.

Three modes of operation are generally used for the RFP formation phase: "self reversal", where a conducting shell maintains and conserves the toroidal flux inside the chamber and is used on OHTE/RFP and often on HBTX1A; "matched mode", where external circuits are programmed to conserve the toroidal flux inside the chamber by maintaining $E_\theta \simeq 0$ at the liner, simulating the action of a conducting shell, as usually used on ZT-40M; and "aided reversal", where the external circuits supplement the plasma self-reversal effect, as typically used on ETA-BETA-II. Field control during the formation phase provides flexibility in varying the pinch parameter, $\Theta$, on which the configuration depends. The

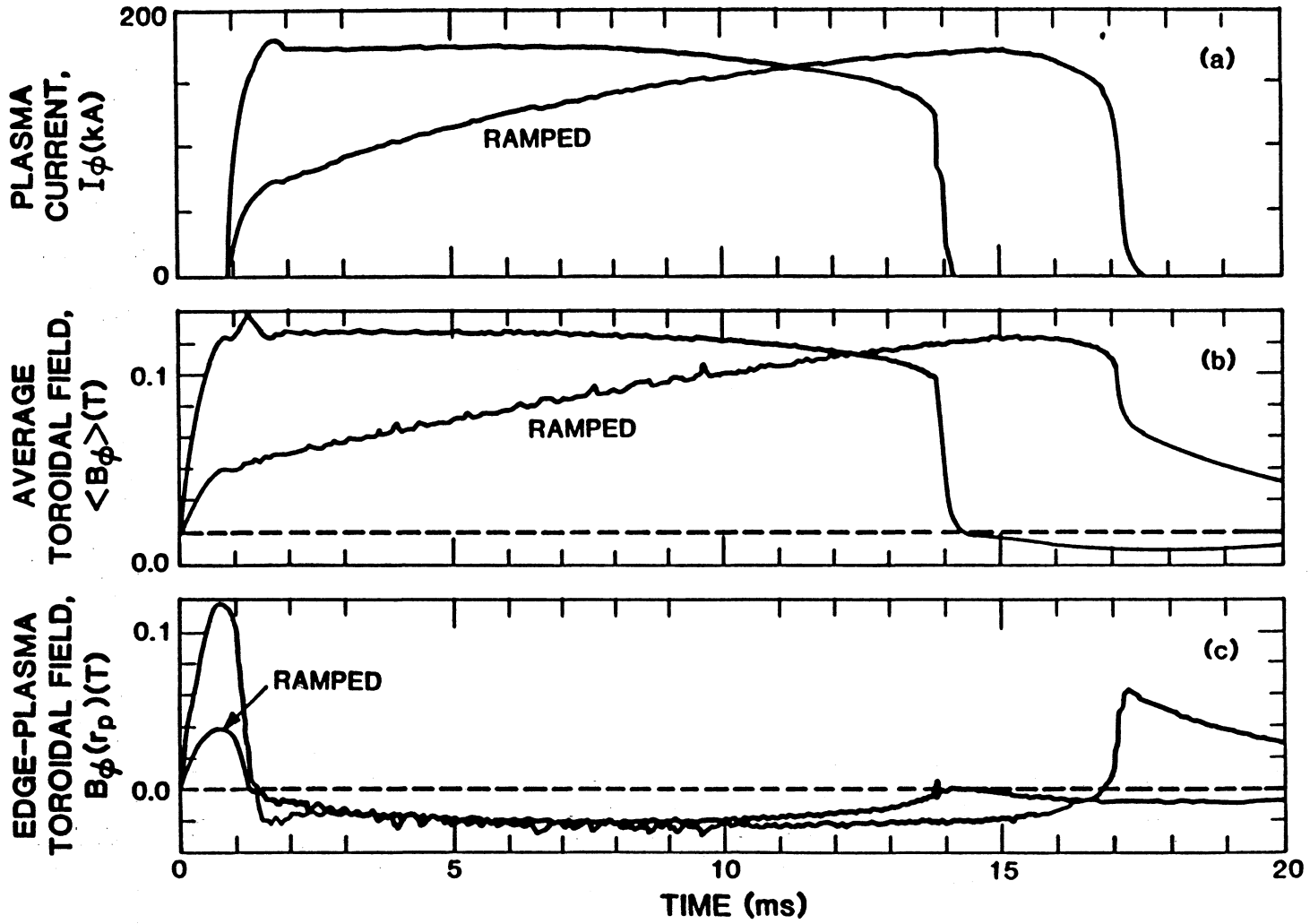


Fig. 4.3.-1. Typical waveforms for the toroidal current, $I_\phi$, average toroidal field $\langle B_\phi \rangle$, and toroidal field at the plasma edge, $B_\phi(r_p)$ (ZT-40M).

choice of the formation mode also affects the consumption of the poloidal flux. The final plasma parameters, however, are not particularly sensitive to the mode used for RFP formation.

Another mode of start-up of an RFP has been demonstrated on the ZT-40M experiment. This mode is called "ramped start-up" because the plasma current is slowly ramped to its final value after an initial low-current RFP is formed. The lower trace in Fig. 4.3.-1 shows such a ramped start-up sequence. In a conventional start-up sequence, the peak current is nearly reached at the time the field at the wall reverses (Fig. 4.3.-1, upper trace). This start-up mode is undesirable in a large experiment or a reactor because the RFP formation phase is a very lossy process until reversal is reached. In a ramped start-up, on the other hand, the RFP configuration is set up in a relatively short time at a low current and then the current is slowly raised to the desired value while maintaining the RFP profiles.

The ramped start-up scenario relies on the plasma relaxation process. During the current ramp, the toroidal flux must be increased proportionally to the current to maintain the RFP profiles (i.e., holding F and $\Theta$ constant). This requires generation of toroidal flux via the dynamo action since the toroidal field at the wall is negative while the average toroidal flux is positive. The plasma must generate an equal and opposite amount of negative and positive flux (to satisfy Faraday's law) and then expel the negative flux from the plasma to generate a net positive flux increase. Indeed, the ramped discharges show that toroidal flux continues to be generated on a multi-millisecond time scale, and negative flux is expelled from the plasma.

The TITAN design relies on ramped start-up scenario for RFP formation and plasma current ramp to its final value. Special attention is given to the RFP formation phase. Experimental data point to a RFP formation "window" in the parameter space constrained by many factors such as the volt-second requirement (i.e, poloidal-flux consumption), equilibrium and field error constraints, plasma density, and current density constraints. These experimental data are described in detail in Sec. 4.5.1 and then extrapolated to find a RFP formation window for the TITAN design.

### 4.3.2. Plasma Parameters

The time variation of the temperature from several machines is shown in Fig. 4.3.-2. For discharges with a flat-top current waveform (Fig. 4.3.-2.a and b) the electron temperature rises rapidly, reaching approximately 100-200 eV

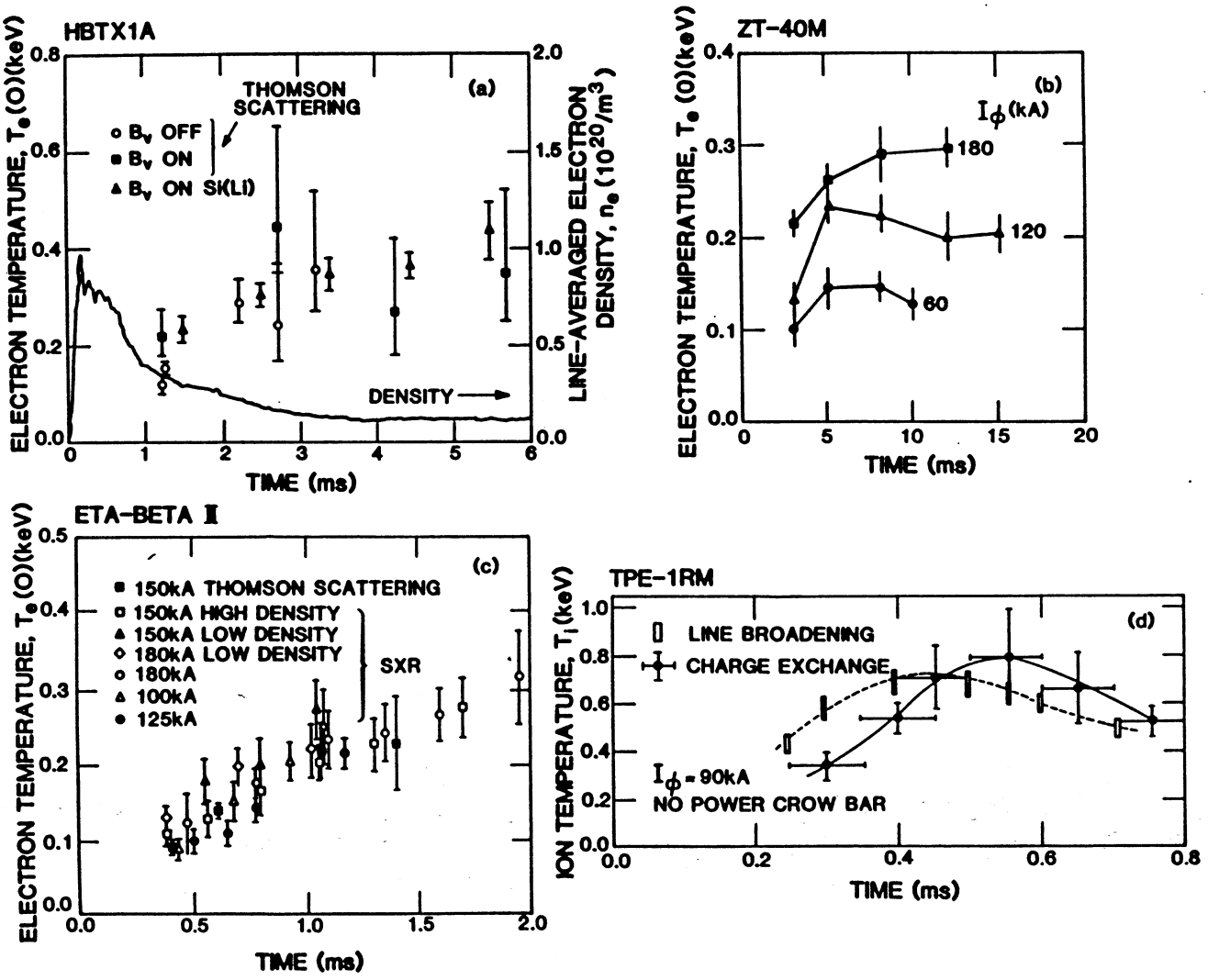


Fig. 4.3.-2. Time dependence of electron temperature for HBTX1A (a), ZT-40M (b), and ETA-BETA-II (c), and ion temperature for TPE-1R(M) (d).

near the time of peak current, and then more slowly as the density drops, reaching ultimately 300-500 eV. At later times the temperature remains approximately constant or decreases slightly. This later behavior is attributed to wall effects, possibly caused by field errors or inadequate equilibrium. Similar behavior of the electron temperature is seen on smaller devices, as is illustrated in Fig. 4.3.-2.c for ETA-BETA-II, where the time scale is much shorter and $T_e$ rises continuously during the pulse. It is shown in Fig. 4.3.-2.b that the temperature increases with plasma current. Similar behavior is generally observed in all RFP experiments.

The ion temperature is usually comparable to the electron temperature, with some examples showing $T_i > T_e$. Figure 4.3.-2.d shows the time variation of the ion temperature in TPE-1R(M). The electron-ion equilibration time, however, is so long that the ions cannot be heated by collisions with electrons and some anomalous ion heating mechanism is apparent.

Generally, RFP experiments operate without active refueling. The chamber is filled with gas prior to the discharge and density is maintained by recycling with the chamber wall. Modern RFP discharges are of sufficient duration where active refueling by pellet injection is being implemented [29]. The temporal variation of plasma density is shown in Fig. 4.3.-3. Typically, the electron density rises initially to a value corresponding to the filling density and then falls rapidly to 10-20% of the filling value during the formation phase (density "pump-out"). Thereafter, the density decays more slowly. In machines with long pulses, the density tends to reach a steady state value which shows little dependence on the initial filling density but depends on the plasma current and the wall conditioning.

The rate of intial pump-out depends strongly on the wall condition and is attributed to particles which leave the discharge and are not replaced fast enough by wall recycling. This process can be affected by pre-conditioning the wall, as seen in Figs. 4.3.-3.a and b for HBTX1B and ZT-40M, respectively. In these experiments, the walls were loaded with hydrogen or deuterium prior to the discharge initiation. The results show that the density decay can be much reduced and the density sustained approximately constant for up to 5 ms or longer without active refueling.

Gas-puffing through external fast-acting valves has been performed on both HBTX1A and ZT-40M. The valves inject a steady stream of gas for a pre-programmed portion of discharge. In these experiments, gas-puffing has increased the density by at least a factor of two while temperature measurements

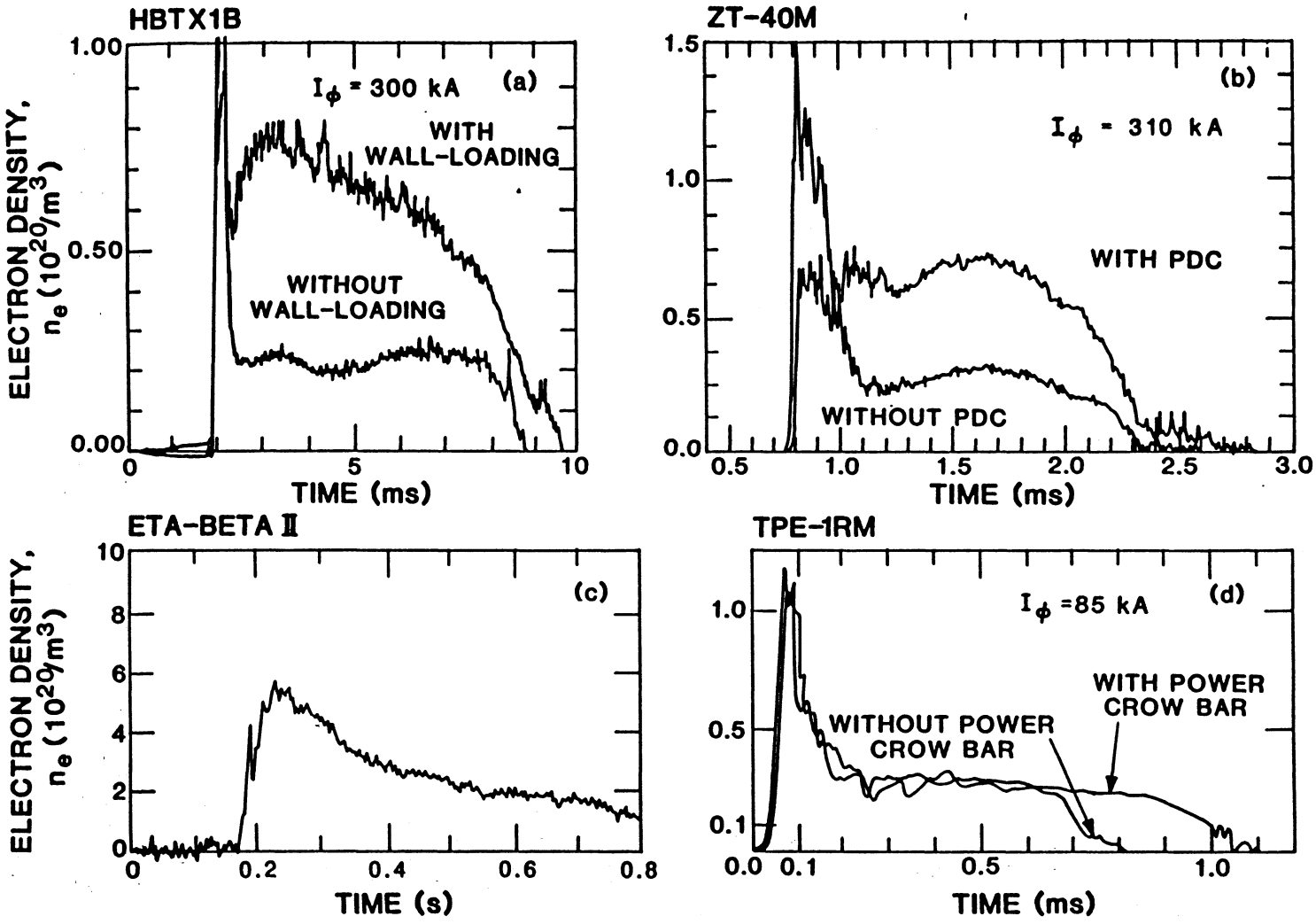


Fig. 4.3.-3. Time dependence of plasma density for HBTX1B (a), ZT-40M (b), and ETA-BETA-II (c), and TPE-1R(M) (d).

indicate that the electron temperature decreased when the density was increased. Also, increasing the plasma density by gas-puffing has increased the duration of the current pulse in both HBTX1A and ZT-40M. Additional gas-puffing experiments await better equilibrium control, since gas-puffing often changes the equilibrium at such a rate that it cannot be controlled by the present feedback systems on these experiments.

### 4.3.3. Fluctuations

Fluctuations of MHD origin are important for field generation and sustainment. Fluctuations can also enhance cross-field transport because of the break-up of the magnetic surfaces and resulting ergodic field-line behavior. Fluctuations have been studied on various RFP experiments [17,34-37]. In HBTX1A, for example, dominant global modes with m = 1 and a broad n spectrum centered around n = -8 (corresponding to the aspect ratio of the device) were found with the minus sign indicating that these modes are resonant inside the reversal surface. Fine-scale activity with a short transverse correlation length, containing comparable power to the global modes, was also found in the core of the discharge. Modes with m = 0 and small toroidal mode numbers were also observed. These dominant modes were observed at all times during the discharge, including the formation phase where the amplitude was a factor 5 to 10 times higher. These oscillations, therefore, appear to a play a fundamental role. In contrast to HBTX1A, coherent quasi-continuous m = 1 activity in the center of the plasma was observed to dominate in low-$\Theta$ ZT-40M discharges [38]. The m = 1 modes were consistent with the predictions of the resistive instability theory.

Estimates of the width and separation of magnetic islands resulting from the m = 1 modes indicate that the field lines are stochastic inside the reversal surface and probably throughout the plasma when the m = 0 modes are taken into account. Qualitative estimates of the energy confinement time based on stochastic field line diffusion from the m = 1 modes are similar in magnitude to those observed on HBTX1A.

The level of magnetic-field fluctuation is denoted by $\tilde{B}/|B|$ where $\tilde{B}$ is the rms value of the random fluctuation amplitude on the poloidal and toroidal fields and $|B|$ is the average value of $(B_\phi^2 + B_\Theta^2)^{1/2}$. The fluctuation levels in RFPs are about $10^{-2}$ and are ten or more times greater than typically observed in tokamaks. The magnetic-field fluctuation levels are observed to decrease with increasing plasma current or magnetic Reynolds number, $S \equiv \tau_\Omega/\tau_A$ where $\tau_\Omega$ and $\tau_A$

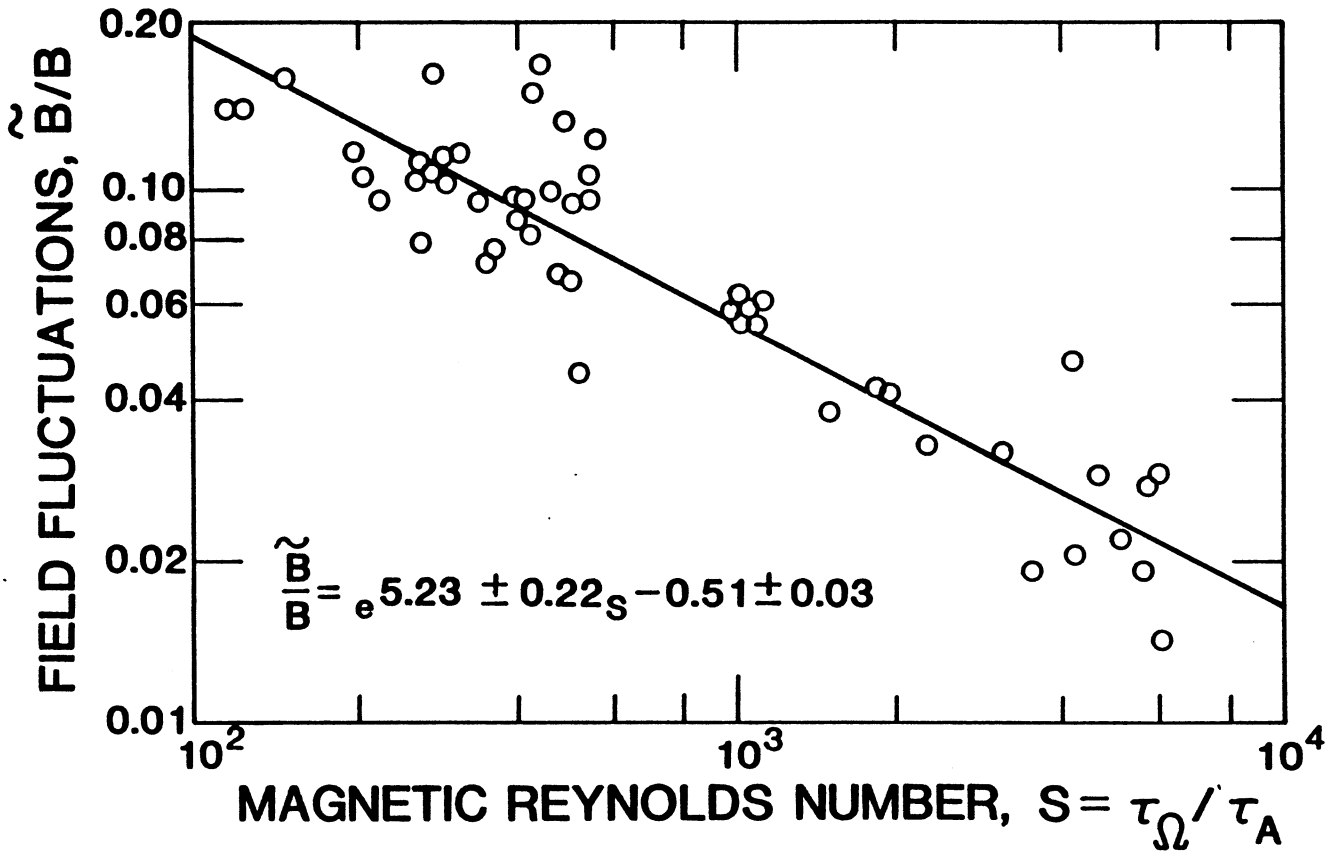


Fig. 4.3.-4. Magnetic fluctuation amplitude as a function of magnetic Reynolds number, S (OHTE).

are, respectively, the resistive and Alfvén times. This behavior is shown in Fig. 4.3.-4 for OHTE/RFP where fluctuation levels appear to decrease as $S^{-1/2}$. Similar behavior is also reported for ETA-BETA-II [39]. The cross-field transport caused by stochastic field-line diffusion, corresponding to such a correlation of fluctuations with S, can give a favorable temperature-current scaling which is consistent with the observed $T_e \propto I_\phi$ dependence.

### 4.3.4. Current termination

Operating RFP experiments usually end with a "current termination" phase where the plasma current is rapidly reduced to approximately zero. This termination occurs in a few tenths of microsecond in small devices and up to a few hundred microseconds in larger machines. Current termination is accompanied by a positive voltage spike and large density and magnetic-field fluctuations. A number of variables such as plasma radius and density, field reversal, magnetic field errors, and impurities are identified to affect the termination. However, a complete and satisfactory explanation of RFP current termination is not yet available.

Some evidence suggests that the onset of termination may be related to a loss of density and confinement, possibly leading to a streaming parameter, $\xi \propto (I_\phi/N)/T_e^{1/2}$, that exceeds a critical value for runaway electrons. A recent study [40] indicates that termination occurs when $I_\phi/N \sim 1\text{-}2\times10^{-13}$ A m, which is consistent with the occurrence of a critical drift threshold when $\xi$ approaches unity.

Rapid current termination can have severe consequences in large, high-current experiments or reactors because of the large voltage spikes and the localized heating of the walls. A method of controlled "rundown" has been tested experimentally on HBTX1B [41] in which the toroidal-field circuit is controlled so that the pinch parameter is maintained at a given value as the current is decreased. The field reversal in this case is maintained until the current reaches a relatively low level. Maintaining reversal in this way is found to delay termination and the current can be reduced to between 10% to 20% of the maximum value before the termination occurs.

### 4.3.5. Scaling

Extensive measurements of the dependence of the temperature to the current for a range of RFPs have been reported. These measurements indicate that the on-axis electron temperature increase with plasma current as $T_e(0) \propto I_\phi^{\nu'}$, where

$\nu'$ is in the range of 0.5-1.0. For several experiments, $\nu' \simeq 1$ up to plasma currents of 500 kA in agreement with the pressure balance Eq. (4.2.-12) for $\beta_\theta$ and $I_\phi/N$ constant. Temperature increases on the order of 1 eV/kA have been observed. Figure 4.3.-5 shows this behavior for OHTE/RFP. Data from ZT-40M for a range of conditions and short-pulse operation are given in Fig. 4.3.-6 which shows $\nu' \simeq 1.2$ while $nT_e \propto I_\phi^2$ (constant $\beta_\theta$). In other experiments on ZT-40M with flat-top operation and longer pulses, it was found that $T_e(0) \propto I_\phi^{0.7}$, but in these conditions, $n \propto I_\phi^{1.3}$, again resulting in $nT_e(0) \propto I_\phi^2$.

More recent results [42,43] suggest that the temperature-current scaling might be better described by postulating a constant beta, $nT_e(0) \propto I_\phi^2$, with a slope determined by $I_\phi/N$. Evidence from a number of experiments indicates that $\beta_\theta$ varies relatively little over a range of conditions and from one machine to another, the latter suggesting little dependence on the dimensions of the apparatus. Some variation of $\beta_\theta$ with $I_\phi/N$ has been reported, with $\beta_\theta$ increasing somewhat as $I_\phi/N$ is reduced and as $I_\phi$ is increased. It should also noted from present experimental results that the range over which favorable scaling is obtained appears to be extended by improved wall-conditioning methods and by reduction in field errors.

Estimates have been made of the energy confinement time, $\tau_E$, on various experiments, but only a limited amount of scaling information is available. Specifically, quantitative data on the variation of $\tau_E$ with machine radius is not available. The experimental value of $\tau_E$ is generally obtained from the ratio of plasma energy to the heating power, which for all RFP experiments to date is the ohmic dissipation of the plasma current.

Under the assumptions of $T_e \propto I_\phi^{\nu'}$, $\sigma \propto T_e^{3/2}$, and $\tau_E \propto r_p^2$, similar to Eqs. (4.2.-12) and (4.2.-13), the following "ohmic" scaling law can be deduced:

$$\tau_E \propto I_\phi^{5/2-\nu'} \; r_p^2 \; f(\beta_\theta, I_\phi/N) \; / \; Z_{eff} \; , \qquad (4.3.-1)$$

where the $\tau_E$ dependence on $\beta_\theta$ and $I_\phi/N$ have been incorporated into the function $f(\beta_\theta \; , \; I_\phi/N)$. In Fig. 4.3.-7, the inverse of plasma diffusivity, $1/\chi_E \propto \tau_E/r_p^2$, is plotted as a function of $I_\phi$ using the data from ZT-40M together with a few data points from ETA-BETA-II and TPE-1R(M). Two analytical curves that fit the data are also included. The design point for TITAN is also shown.

In the case where $\beta_\theta(I_\phi/N)$ is approximately constant, then $T_e \propto I_\phi$, and classical ohmic scaling Eq. (4.3.-1) yields $\tau_E \propto I_\phi^{3/2} \; r_p^2$, with the constant of

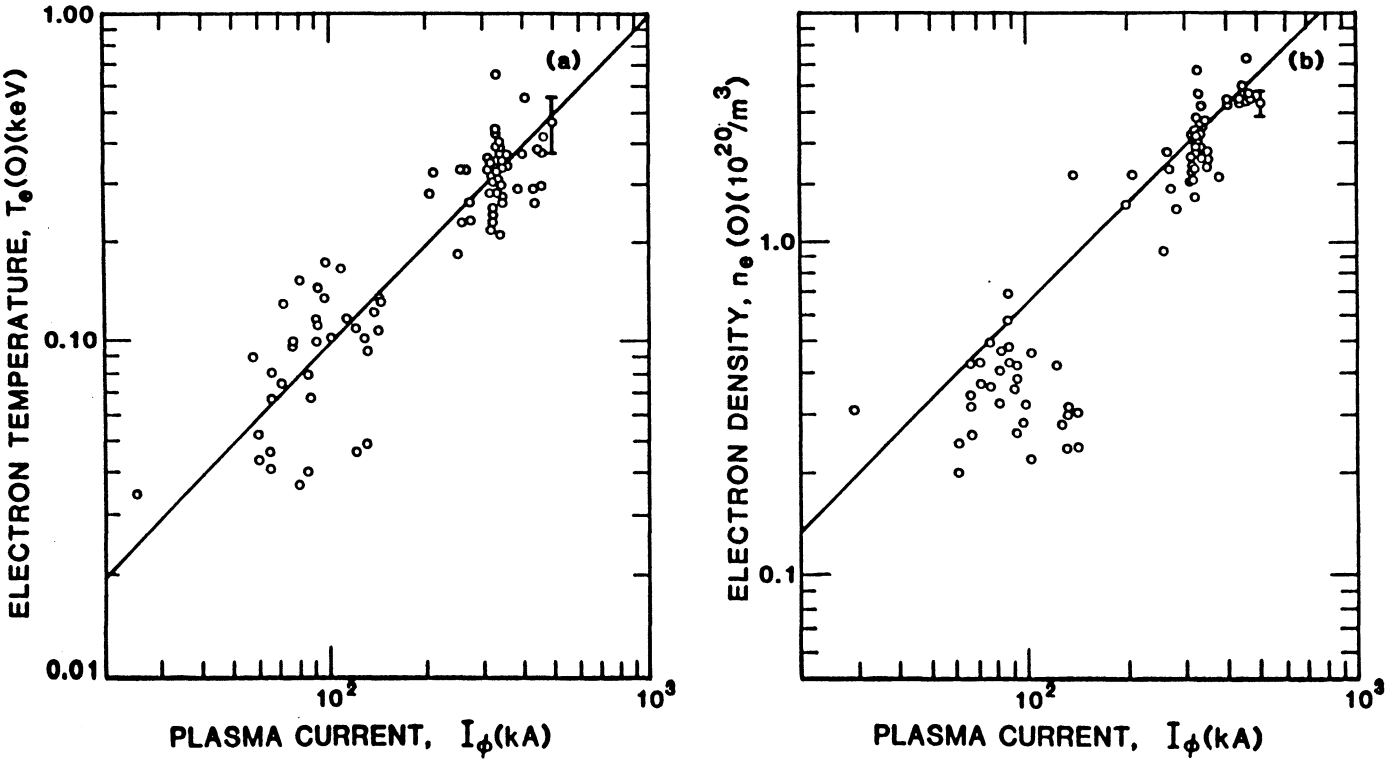


Fig. 4.3.-5. Variation of central electron temperature and central electron density with the plasma current (OHTE).

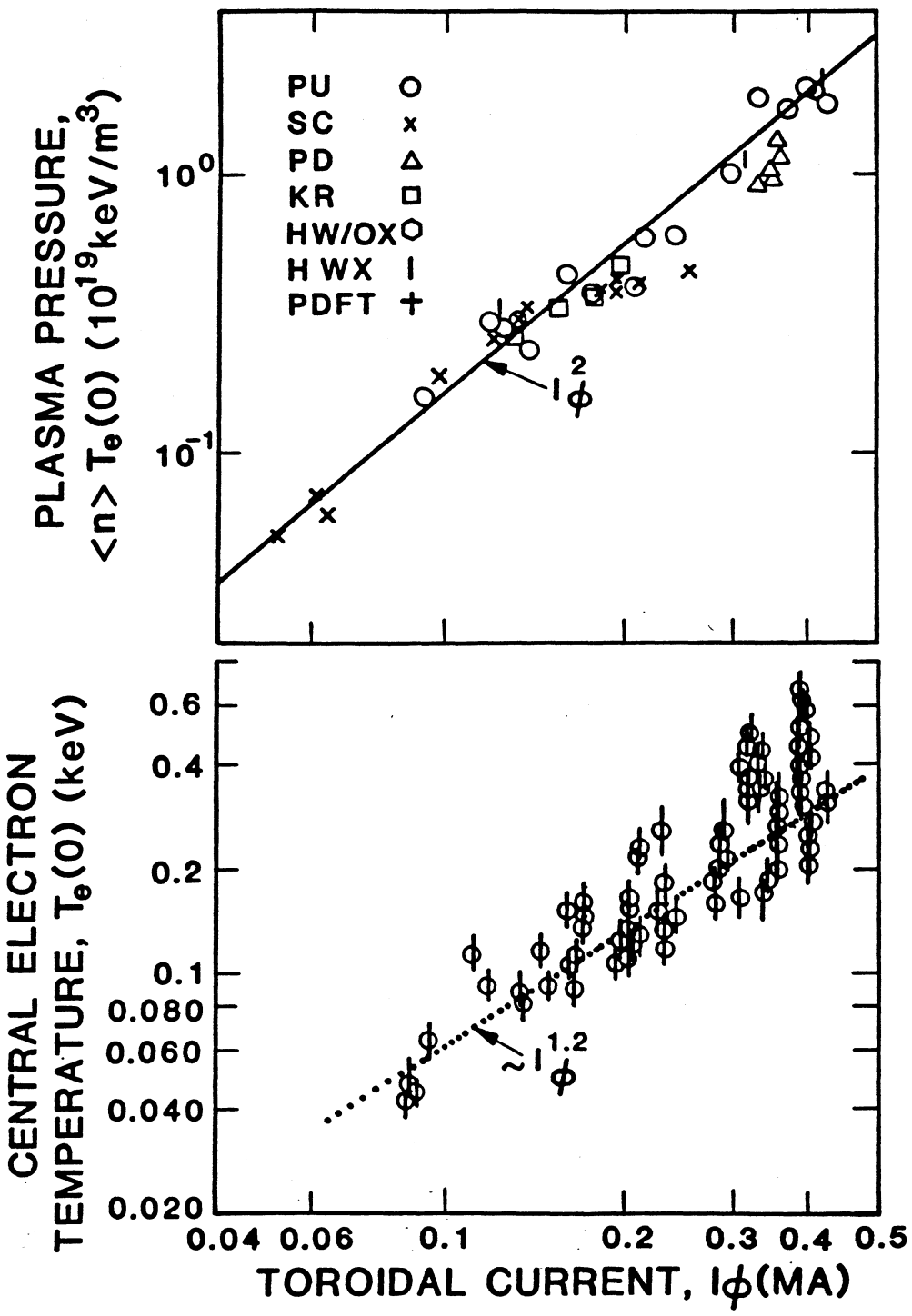


Fig. 4.3.-6. Variation of central electron temperature and the product of central electron temperature with the average electron density with the plasma current (ZT-40M).

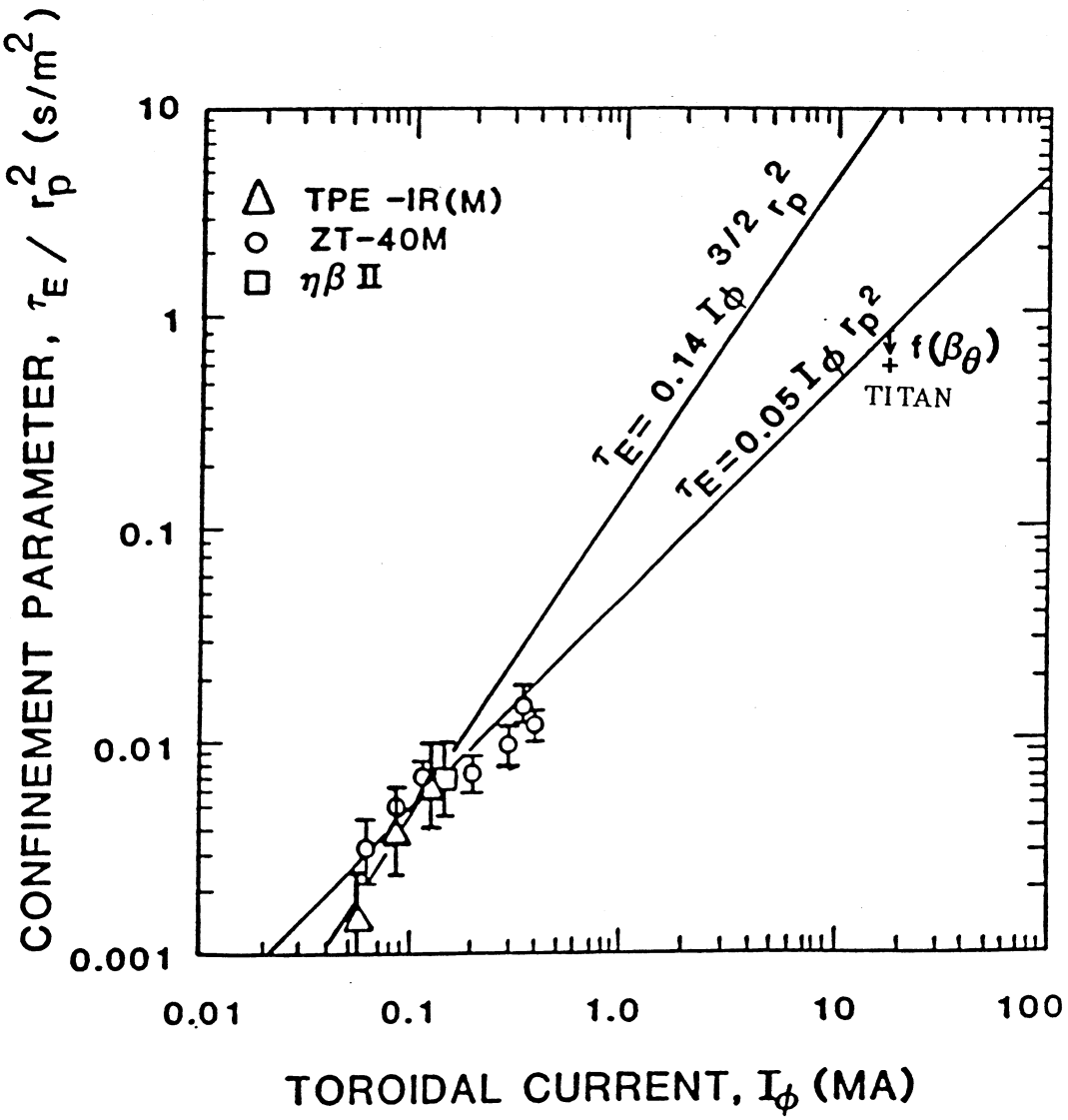


Fig. 4.3.-7. Variation of global energy confinement time, $\tau_E$, with plasma current with data from several experiments.

proportionality depending on $\beta_\theta^{5/2}(I_\phi/N)^{3/2}/Z_{eff}$. The ZT-40M data of Fig. 4.3.-7 is plotted in Fig. 4.3.-8 in the form of $n\tau_E$ as a function of plasma current, which depends only on the parameter $(I_\phi/N)^{1/2}/Z_{eff}$, and is in agreement with the classical scaling $n\tau_E \propto I_\phi^{5/2}$, provided that $Z_{eff}$ does not vary. A similar conclusion was also reached in OHTE/RFP, where a value of $n\tau_E \sim 10^{17}$ s/m$^3$ was recorded.

4.3.6. Evidence of a Beta-Limited Confinement

The observed scaling of plasma pressure with the toroidal current, $nT_e(0) \propto I_\phi^2$, is very suggestive that RFPs operate near a beta limit; the transport would adjust by MHD activity, radiation, or other mechanism to lose energy at a sufficient rate to maintain $\beta_\theta$ constant.

To test this hypothesis, a set of experiments was performed on ZT-40M by adding trace quantities of krypton as an impurity [44,45] to enhance the radiative losses of the plasma. The choice of krypton was made to maximize the ratio of radiated power to the ohmic heating input. It was found that as the impurity was injected, the radiation losses, $P_{rad}$, were increased, but at the same time, the input power, $P_{in}$, only slightly increased and most importantly the poloidal beta remained constant. It follows that as radiation losses increased, the non-radiative losses decreased to preserve the constant beta.

A simple zero-dimensional power balance equation for a plasma at steady state gives , $P_{in} = P_{loss} = P_{rad} + P_{nr}$, where $P_{nr}$ and $\tau_{nr}$ are, respectively, the non-radiative power loss and non-radiative energy confinement time. Using the definition of the global energy confinement time, $\tau_E$, one can write

$$\tau_{nr} = \tau_E \left(1 - \frac{P_{rad}}{P_{loss}}\right)^{-1} . \qquad (4.3.-2)$$

For the assumed constant beta scaling and self-similar profiles of density and electron temperature (i.e., before and after krypton injection), the values of the total energy loss, $P_{loss}$, and $\tau_E$ remains unchanged. Equation (4.3.-2) then indicates that as the radiative losses were increased, the non-radiative losses were decreased (or $\tau_{nr}$ was increased) to maintain the energy content of the plasma and keep $\beta_\theta$ constant. The data from the krypton impurity experiments are plotted in Fig. 4.3.-9 which agree closely with predictions of Eq. (4.3.-2).

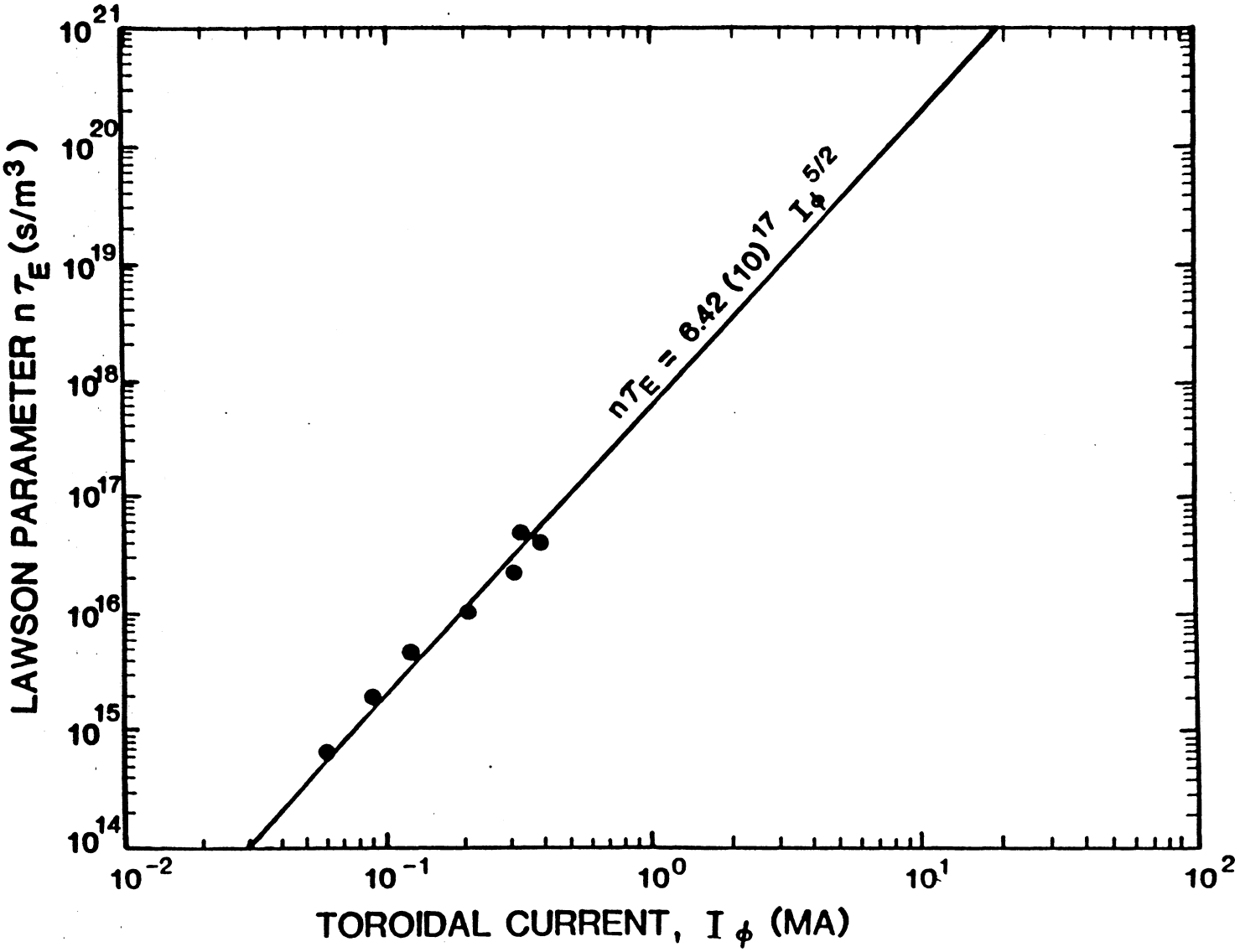


Fig. 4.3.-8. Variation of the Lawson parameter, $n\tau_E$, with the plasma current (ZT-40M).

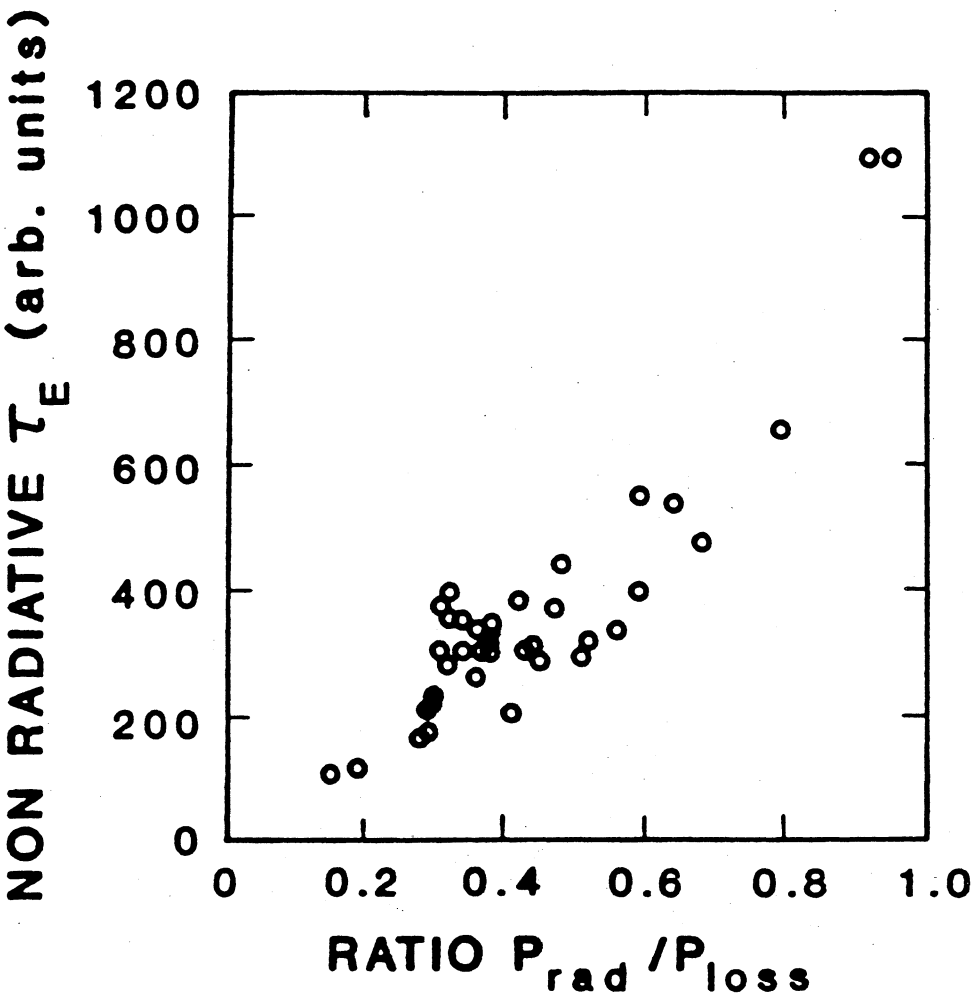


Fig. 4.3.-9. Scaling of the non-radiative energy confinement time with the fractional radiative power loss (ZT-40M).

A second experimental check was made on the beta limit hypothesis. The energy confinement scaling Eq. (4.3.-1) also predicts that the total energy confinement of the plasma scales as $Z_{eff}^{-1}$. By injecting krypton impurities, the plasma resistance was varied and the total confinement time was measured. These experimental data is shown in Fig. 4.3.-10, which indicate that $\tau_E$ scales as $Z_{eff}^{-1}$, as predicted by Eq. (4.3.-1).

It is important to point out that while these results are very suggestive of the beta limit hypothesis they are not conclusive. Furthermore, it appears that far more power is being supplied to the discharge than is needed to maintain the plasma at its beta limit [44,45] and, therefore, these experiments are not expected to show an underlying transport which is not affected by the beta limit hypothesis.

4.3.7. Summary

In this section, the principles of the RFP confinement concept were discussed and the experimental data base was briefly reviewed. This data base is less extensive than that of tokamaks and, therefore, requires a larger extrapolation to reactor relevant regimes. However, modern RFP experiments such as those of Table 4.3.-I have all demonstrated the robustness of the RFP dynamo and an emerging commonality of the basic physical processes operative in RFPs.

The key physics requirements and uncertainties for a RFP reactor include heating, transport, plasma-wall interaction, current-drive (now under experimental investigation) and impurity control/particle exhaust with pumped limiters or magnetic divertors. The largest uncertainties in the existing RFP data base remain in the confinement physics and, in particular, in the mechanism and magnitude of cross-field transport in the near-minimum-energy state RFP configuration. Experiments with higher currents (and possibly higher current densities) and variable plasma size are needed to distinguish between different possible scaling laws. The modern RFP experiments are physically small, but operate with reactor-like power density; therefore, they can be strongly influenced by plasma-wall interaction. The increased particle and heat load on the first wall and limiter systems, and the need to control plasma-wall interactions also represent major challenges for the next-step multi-mega-ampere experiments.

Data from large multi-mega-ampere experiments are expected in the early 1990s. These data are of the utmost importance in resolving some of the key physics requirements and uncertainties for a RFP reactor. Furthermore, these

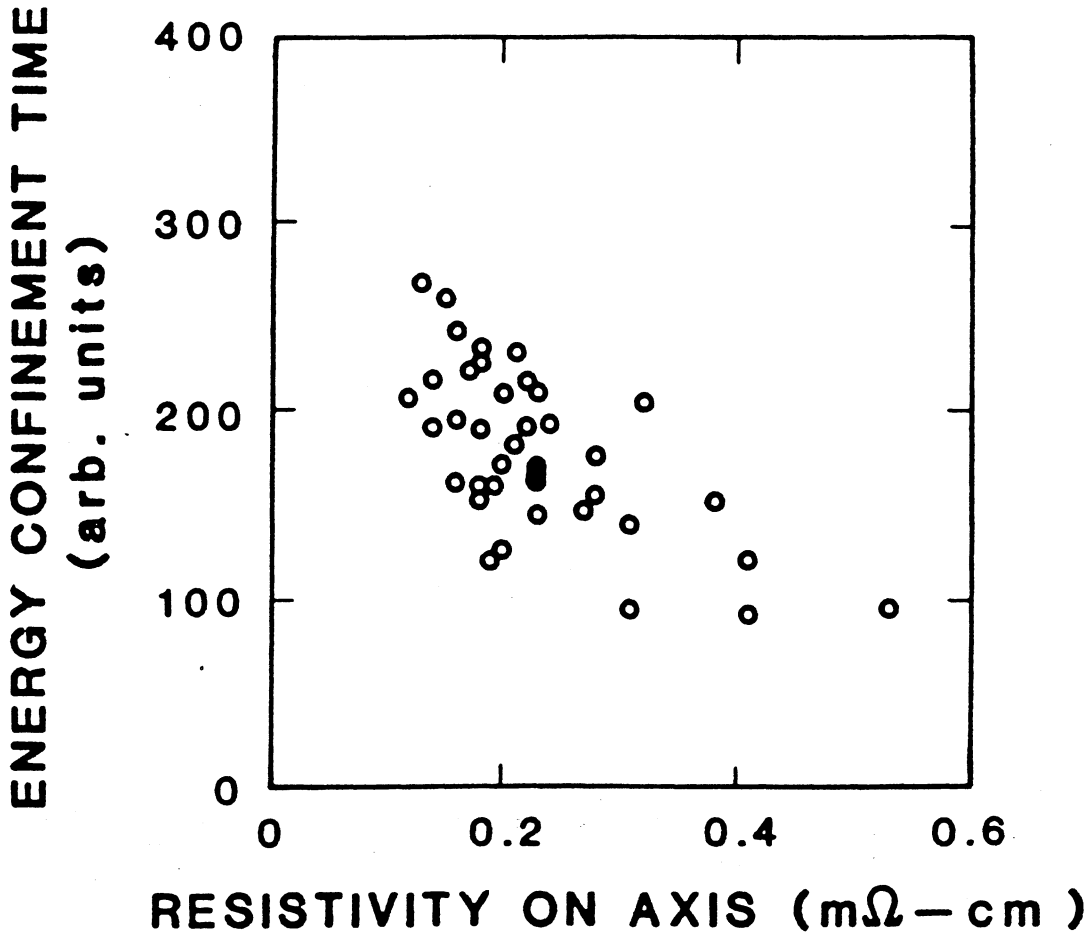


Fig. 4.3.-10. Dependence of $\tau_E$ with the effective plasma resistivity (ZT-40M).

next-step experiments can provide valuable technological insight for devising a development path towards RFP fusion reactors.

## 4.4. MAGNET CONFIGURATION

The magnet configuration consists of a poloidal-field-coil (PFC) set, a toroidal-field-coil (TFC) set, a divertor-coil set, and an Oscillating-Field Current-Drive (OFCD) coil set. The divertor and the OFCD analyses have not progressed sufficiently to yield specific coil designs. Similarly, a detailed TFC design has not been performed, but two options are under consideration. One option uses a discrete set of normal-conducting, copper coils positioned outside the blanket/shield, similar to the CRFPR design [46], and is discussed in Sec. 4.4.2. The second TFC option is to use the integrated blanket/coil (IBC) concept [47], which is discussed in Sec. 8.2.5. An analysis of the PFC issues leading to the reference FPC design is presented in Sec. 4.4.1.

### 4.4.1. Poloidal-Field Coil (PFC) System

The PFC set performs both an equilibrium and an ohmic-heating (start-up) function. The equilibrium function requires that a vertical field of a certain magnitude and index, $n = \partial(\ln B_v)/\partial(\ln R)$, corresponding to the plasma current and beta [8,48,49], be imposed over the plasma cross section in order to maintain the plasma against the outward expansive forces arising from plasma and poloidal-field pressure. The ohmic-heating function provides the poloidal-flux swing required to establish the steady-state plasma current, which is then subsequently sustained by OFCD (Sec. 4.6). Since the ohmic-heating function is required only during start-up and the equilibrium function is required continuously, the PFC set is naturally, but not necessarily, split into two coil sets: an equilibrium-field coil (EFC) set and an ohmic-heating coil (OHC) set; both are discussed separately in the following subsections.

#### 4.4.1.1. Equilibrium-Field Coils (EFCs)

Since the EFCs are continuously active, the recirculating power can be minimized by using superconducting EFCs. Superconducting EFCs, however, require $\geq$ 1.5 m of blanket and shielding between the coils and plasma compared to $\leq$ 0.8 m for normal-conducting EFCs; hence, more current is needed to produce the same field resulting in a more massive and expensive coil set. The trade-off between normal-conducting and superconducting EFCs was examined and found to

weigh somewhat in favor of superconducting EFCs (Sec. 5.3). Consequently, the use of superconducting EFCs is adopted for the scoping phase study. A more detailed analysis of the superconducting EFC performance during the plasma transients is underway. An additional constraint is imposed to use only a single pair of EFCs positioned not to interfere with vertical or horizontal movement of the first wall, blanket, shield, and TFC assembly during maintenance procedures.

The steady-state EFC currents are determined by equating on-axis EFC vacuum field to the vertical field required for toroidal equilibrium. The required vertical field, $B_v$, is given by [8,48]

$$B_v = \frac{\mu_o I_\phi}{4\pi R_T}\left[\ln\left(\frac{8R_T}{r_p}\right) + \frac{l_i}{2} + \beta_\theta - 1.5\right] , \qquad (4.4.-1)$$

where $R_T$ and $r_p$ are the plasma major and minor radii, respectively, $I_\phi$ is the steady-state plasma current, $\beta_\theta$ is the poloidal beta, and $l_i$ is the internal inductance per unit length of plasma. Typically, $l_i \simeq 1$ for RFP field and current profiles. The position of the EFCs is determined such that the value of the decay-index,

$$n \equiv -\frac{\partial(\ln B_v)}{\partial(\ln R)} \simeq \frac{R_T}{r_p}\frac{B_v(R_T - r_p) - B_v(R_T + r_p)}{B_v(R_T - r_p) + B_v(R_T + r_p)} , \qquad (4.4.-2)$$

remains in the range $0 < n < 1.5$ [49]. Having a circular plasma cross section further constrains the index [48] to $0 < n \leq 0.65$, which is the criterion used herein. The resulting EFC design is shown in Fig. 4.4.-1 and the associated parameters are given in Tables 4.4.-I to 4.4.-III.

4.4.1.2. Ohmic-Heating Coils (OHCs)

The most efficient coupling of OHCs to the plasma is obtained with the "close-fitting" OHC configuration shown in Fig. 4.4.-1. Such a configuration requires the removal of most of the OHCs in the upper-half plane to gain access to the reactor torus for (single-piece) maintenance purposes. In order to eliminate the need for coil movement for maintenance purposes, one can array the

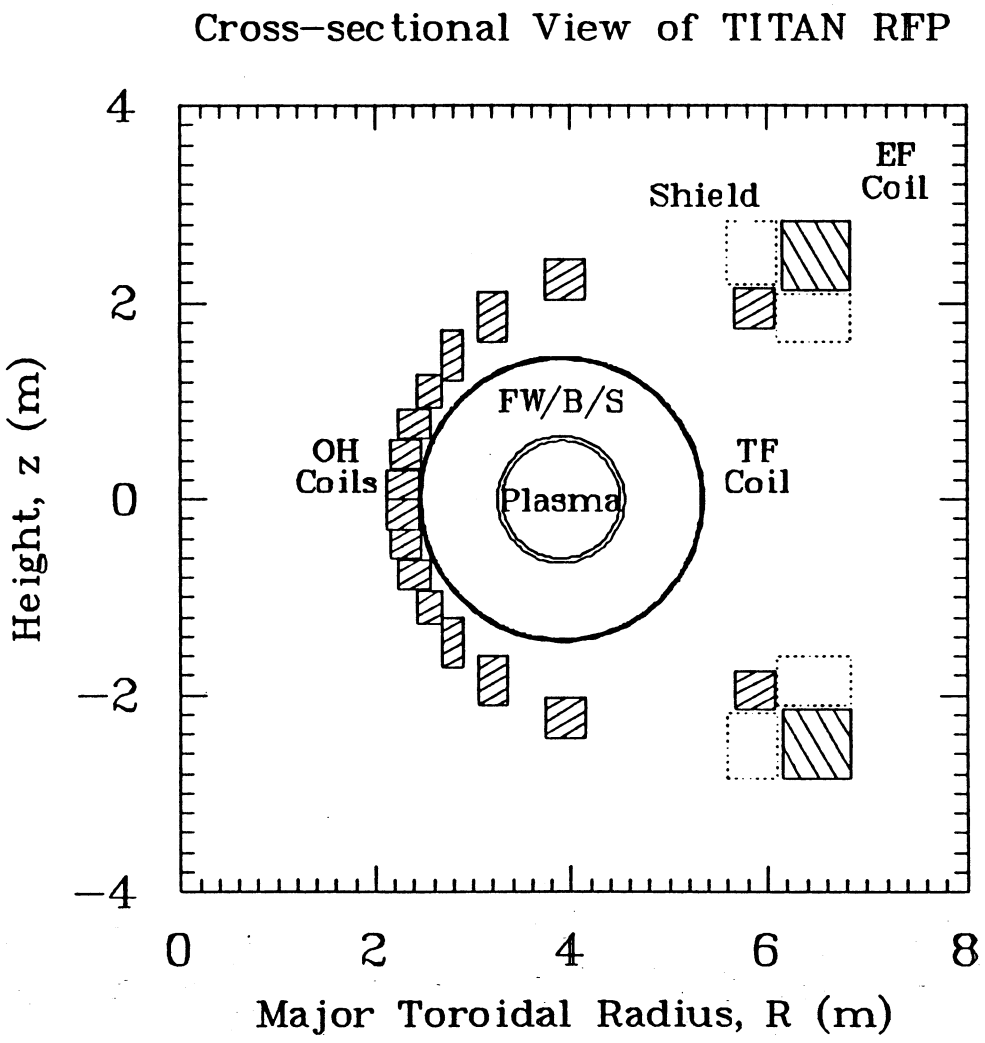


Fig. 4.4.-1. A cross-sectional view of the "close-fitting" poloidal-field coil set for the 18-MW/m$^2$ Strawman design. The locations of the toroidal-field (TF) coils (if IBC is not used), the first wall, blanket, and shield assembly (FW/B/S), and the plasma are shown in addition to the equilibrium-field (EF) coils and the ohmic-heating (OH) coils.

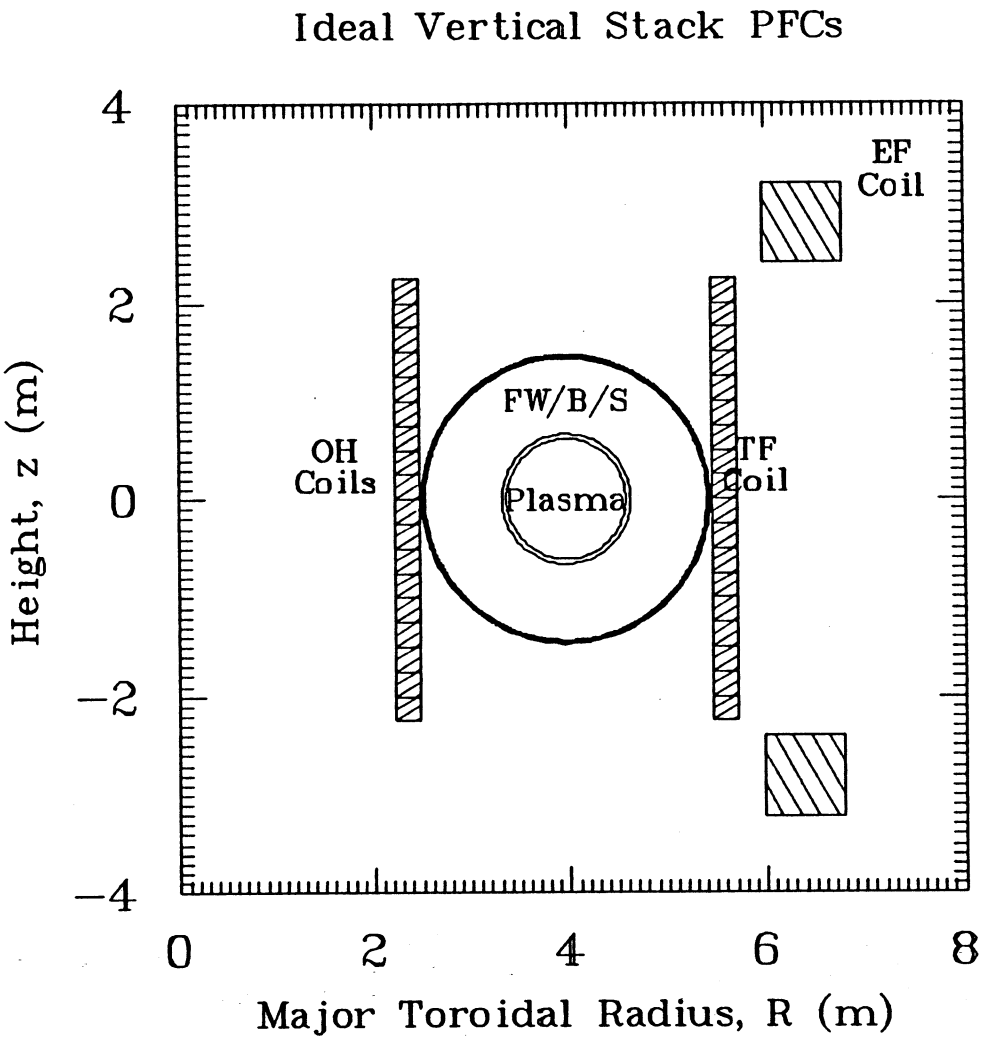


Fig. 4.4.-2. A cross-sectional view of the "vertical-stack" OHC configuration considered for the 18-MW/m$^2$ Strawman design. The locations of the toroidal-field (TF) coils (if IBC is not used), the first wall, blanket, and shield assembly (FW/B/S), and the plasma are shown in addition to the equilibrium-field (EF) coils and the ohmic-heating (OH) coils.

TABLE 4.4.-I

PFC Locations and Parameters for the 18-MW/m$^2$ Strawman Design

| Function | R (m) | ±z (m) | ΔR (m) | Δz (m) | A (m$^2$) | I$^{(a)}$ (MA) | j$^{(a)}$ (MA/m$^2$) | Mass$^{(b)}$ (tonne) |
|---|---|---|---|---|---|---|---|---|
| EF | 6.4959 | 2.4873 | 0.6973 | 0.6973 | 0.4862 | 8.882 | 18.27 | 146.1 |
| OH1 | 5.8699 | 1.9473 | 0.4000 | 0.4000 | 0.1600 | -2.057 | 12.86 | 43.4 |
| 2 | 3.9472 | 2.2299 | 0.4100 | 0.4100 | 0.1681 | -2.057 | 12.24 | 30.7 |
| 3 | 3.1958 | 1.8533 | 0.3000 | 0.5000 | 0.1500 | -2.057 | 13.71 | 22.2 |
| 4 | 2.7905 | 1.4625 | 0.2000 | 0.5000 | 0.1000 | -2.057 | 20.57 | 12.9 |
| 5 | 2.5503 | 1.1031 | 0.2500 | 0.3300 | 0.0825 | -2.057 | 24.94 | 9.7 |
| 6 | 2.4028 | 0.7705 | 0.3300 | 0.3000 | 0.0990 | -2.057 | 20.78 | 11.0 |
| 7 | 2.3163 | 0.4557 | 0.3200 | 0.3000 | 0.0960 | -2.057 | 21.43 | 10.3 |
| 8 | 2.2759 | 0.1508 | 0.3300 | 0.3000 | 0.0990 | -2.057 | 20.78 | 10.4 |

(a) Values are at steady state for the EFCs and at the back bias for the OHCs.
(b) A density of 7.36 tonne/m$^3$ is assumed.

OHCs into two vertical stacks with one stack positioned inboard of the torus and the other outboard (Fig. 4.4.-2). Both the "close-fitting" and the "vertical-stacks" configurations were analyzed in the scoping phase study using the code CCOIL [46,50].

The locations of the close-fitting OHCs are determined in CCOIL by first specifying an arc, which is defined as a segment of an ellipse that is symmetric about the equatorial plane, upon which the coils are to be arrayed. The Fourier coefficients for a series representation of the current distribution on the arc that excludes flux from the entire plasma cross section are then determined. Assuming equal-current coils to facilitate series electrical connection of the coils, the current distribution is integrated along the arc to yield the OHC current-center locations.

The locations of the vertical-stack OHCs are taken to be uniformly spaced within a stack and each stack is positioned adjacent to the TFCs in the equatorial plane to maximize vertical access to the torus (Fig. 4.4.-2). The coils within a stack are of equal current. The current distribution between stacks is determined by requiring the coil set exhibit an on-axis field null in order to facilitate RFP early breakdown/formation (Sec. 4.5.1).

The single-turn back-bias and forward-bias OHC currents, $I_{OH}^{-}$ and $I_{OH}^{+}$, are determined by imposing inductive flux conservation and ignoring the resistive losses, as given below:

TABLE 4.4.-II

PFC Parameters for the 18-MW/m$^2$ Strawman Design

| Parameter | Value |
|---|---|
| EFC current (MA)[a] | 17.8 |
| EFC volume (m$^3$) | 39.7 |
| EFC mass (tonne) | 292.1 |
| EFC joule losses (MW)[a] | (378.4 NC)(0.0 SC) |
| EFC peak field (T)[a] | 5.9 |
| EFC current density (MA/m$^2$)[a] | 18.3 |
| Vertical field index | 0.16 |
| OHC current (MA) | |
| ♦ back bias | -32.9 |
| ♦ forward bias | 15.1 |
| OHC volume | 40.9 |
| OHC mass (tonne) | 301.2 |
| OHC joule losses (MW) | (68.1[c])/321.6[b] |
| OHC von Mises stress (MPa)[b] | 215.6 |
| OHC peak field (T)[b] | 8.3 |
| OHC current density (MA/m$^2$)[b] | (12.2-24.9) |
| OHC stray vertical field (mT)[b] | 1.25 (<2.45[d]) |
| PFC transparency (%) | 67.2 |

(a) Steady-state values.
(b) Back-bias values.
(c) Forward-bias values.
(d) Stray vertical field constraint (see Sec. 4.5.1).

$$L_p I_\phi = M_{EF,p}\, I_{EF} + M_{OH,p}\, (I^+_{OH} - I^-_{OH}), \qquad (4.4.-3)$$

where $I_\phi$ and $I_{EF}$ are the steady-state plasma and EFC currents, respectively, $M_{i,j}$ is the mutual inductance between the $i^{th}$ and $j^{th}$ circuit elements, and $L_p$ is the plasma self-inductance. An additional constraint of a bipolar current swing, based on the startup scenario described in Sec. 4.5, is imposed to minimize the energy-storage and power-handling requirements:

TABLE 4.3.-III

PFC Circuit Parameters for the 18-MW/$m^2$ Strawman Design

| Parameter | Value |
|---|---|
| Self-Inductances (μH) | |
| • $L_p$ | 13.26 |
| • $L_{EF}$ | 14.80 |
| • $L_{OH}$ | 3.39 |
| Mutual Inductances (μH) | |
| • $M_{OH,p}$ | 3.47 |
| • $M_{OH,EF}$ | 3.08 |
| • $M_{EF,p}$ | 3.87 |
| Current Levels (MA) | |
| • $I_\phi$ | 17.75 |
| • $I_{EF}$ | 17.76 |
| • $\Delta I_{OH}$ | 48.07 |
| Magnetic Fluxes (Wb) | |
| • Plasma | 235. |
| • EFC | 68. |
| • OHC | 167. |

$$|I_{OH}^-| = I_{OH}^+ + I_{EF} \ . \qquad (4.4.-4)$$

The mutual inductances used in Eq. (4.4.-3) are estimated from the following formula for two coaxial hoops [51]:

$$M_{i,j} = \frac{2\mu_o(r_i r_j)^{1/2}}{k} [(1 - k^2/2)K(k) - E(k)] \ , \qquad (4.4.-5)$$

where

$$k = \frac{4r_i r_j}{(r_i + r_j)^2 + \Delta_z^2} \ . \qquad (4.4.-6)$$

The radii of the $i^{th}$ and $j^{th}$ hoops are $r_i$ and $r_j$, $\Delta_z$ is the distance between the

two parallel coil planes, and K(k) and E(k) are the complete elliptic integrals of the first and second kinds, respectively. Each coil in a coil set is simulated by 100 hoops to ensure that a high degree of accuracy is obtained, especially for coil self-inductances. The plasma, however, is simulated with a single-hoop current, which is positioned in the equatorial plane at a major radius, $R_T'$, that includes a Shafranov shift [8]:

$$R_T' = R_T + \frac{r_w^2}{2R_T}\left[(\beta_\theta + \frac{l_i}{2} - \frac{1}{2})(1 - x^2) - \ln x\right] , \qquad (4.4.-7)$$

where $R_T$ is the torus major radius, $r_w$ is the first-wall minor radius, and $x = r_p/r_w$ is the ratio of plasma and first-wall minor radii. When the calculation of the single-turn mutual inductance involves a coil set, a summation is performed over each hoop in each coil in the set; for example,

$$M_{OH,j} = \sum_{i=1}^{n_{OH}} M_{i,j} , \qquad (4.4.-8)$$

where $n_{OH} = 100\ N_{OH}$ is the number of hoops used to simulate the number of OHCs, $N_{OH}$. The single-turn self-inductances of the coil sets are determined by application of the formula for mutual inductance with both summations over the same coil set as follows:

$$L_k = \sum_{i}^{n_k} \sum_{j}^{n_k} M_{i,j} . \qquad (4.4.-9)$$

where all of the filaments are equi-spaced and carry equal currents. The singular element $M_{i,i}$ is replaced with the self-inductance of a wire of finite minor radius given by [51]

$$M_{i,i} = \mu_0 R_i \left[ \ln\left(\frac{8R_i}{\Delta}\right) - 1.75 \right], \qquad (4.4.-10)$$

where $R_i$ is the major radius of the hoop used to simulate a coil and $\Delta$ is the separation between the filaments and assumed to be 0.01 m. The plasma self-

inductance is expressed as a sum of an external inductance, $L_{p,ex}$, and an internal inductance, $L_{p,in}$, (i.e., $L_p = L_{p,in} + L_{p,ex}$). The external inductance is taken to be that for a wire with the same dimensions as the plasma [51]:

$$L_{p,ex} = \mu_0 R_T \left[ \ln \left( \frac{8R_T}{r_p} \right) - 2 \right] . \qquad (4.4.-11)$$

The internal inductance is derived from results of a one-dimensional equilibrium calculation [46] and is given by

$$L_{p,in} = \left[ 2\pi R_T (W_\theta + W_\phi) - \frac{\Phi^2}{2L_o} \right] (I_\phi)^{-2} , \qquad (4.4.-12)$$

where

$$W_i \equiv \frac{\pi}{\mu_o} \int_0^{r_p} B_i^2(r)\, r\, dr , \qquad (4.4.-13)$$

$$\Phi \equiv 2\pi \int_0^{r_p} B_\phi(r)\, r\, dr , \qquad (4.4.-14)$$

$$L_o \equiv \frac{\mu_o r_p^2}{2R_T} . \qquad (4.4.-15)$$

The above algorithms have been used to analyze the "close-fitting" and "vertical-stack" configurations. An additional constraint on the OHC design is the maximum level of the stray vertical field during breakdown, as described in Sec. 4.5.1. This constraint is in the form of a maximum value for the ratio of the stray vertical field to the initial toroidal field, $B_{\phi o}$, given by Eq. (4.5.-1). For a given $B_{\phi o}$, this constraint limits the stray vertical field produced by the OH coil set.

For the case of the vertical-stack configuration, the coil geometry is fixed by maintenance considerations. For the close-fitting configurations, however, the coil geometry is not placed under such a constraint and can be manipulated through the arc parameters to reduce the stray vertical field. The profiles of stray vertical field in the equatorial plane are shown in Figs. 4.4.-3 and 4.4.-4 in the back-bias condition for the close-fitting and vertical-stack configurations, respectively. Only the close-fitting configuration complies with the stray-vertical-field constraint by virtue of the freedom to move OHCs over the torus.

In principle, the initial toroidal field, $B_{\phi o}$, can be increased to ensure that the "vertical-stack" configuration complies with the stray-vertical-field constraint (4.5.-1). However, any increase in $B_{\phi o}$ would result in increases in the OHC volt-second consumption and in the formation energy and power. For example, with the vertical-stack configuration of Fig. 4.4.-2, $B_{\phi o}$ must be increased by one to two orders of magnitude. A single order of magnitude increase in the value of $B_{\phi o}$ would result in a volt-second consumption during formation $\geq$ 80 V-s, a formation energy $\geq$ 200 MJ, and a formation power $\geq$ 1 GW (Sec. 4.5.1). Consequently, a maximum value of 2.45 mT for the stray vertical field is adopted here.

A secondary constraint that the OHC set exhibit a field null within the plasma chamber, which is demonstrated in Fig. 4.4.-3 and Fig. 4.4.-4 for both configurations. Consequently, the close-fitting configuration of Fig. 4.4.-1 and Tables 4.4.-I to 4.4.-III has been adopted for the PFC design.

The circuit parameters of Table 4.4.-III, then, are used in the time-dependent simulation, which includes plasma-resistance effects and is discussed in Sec. 4.5.2, to yield more accurate determinations of the following back-bias OHC parameters: current, current density, joule losses, von Mises stress, peak field, and stray vertical field. Design iterations between the time-dependent simulation and CCOIL have not been performed.

### 4.4.2. Toroidal-Field Coil (TFC) System

Two options are being considered for the generation of the toroidal field. The first option is the use of normal-conducting, copper TFCs, positioned outside of the blanket and shield as is shown in Fig. 4.4.-1. In order to permit service access to the first wall, blanket, divertor, and plasma chamber, the TFCs must be discretized rather than forming a continuous toroidal shell. The discretization of the TFCs, however, introduces a toroidal-field ripple,

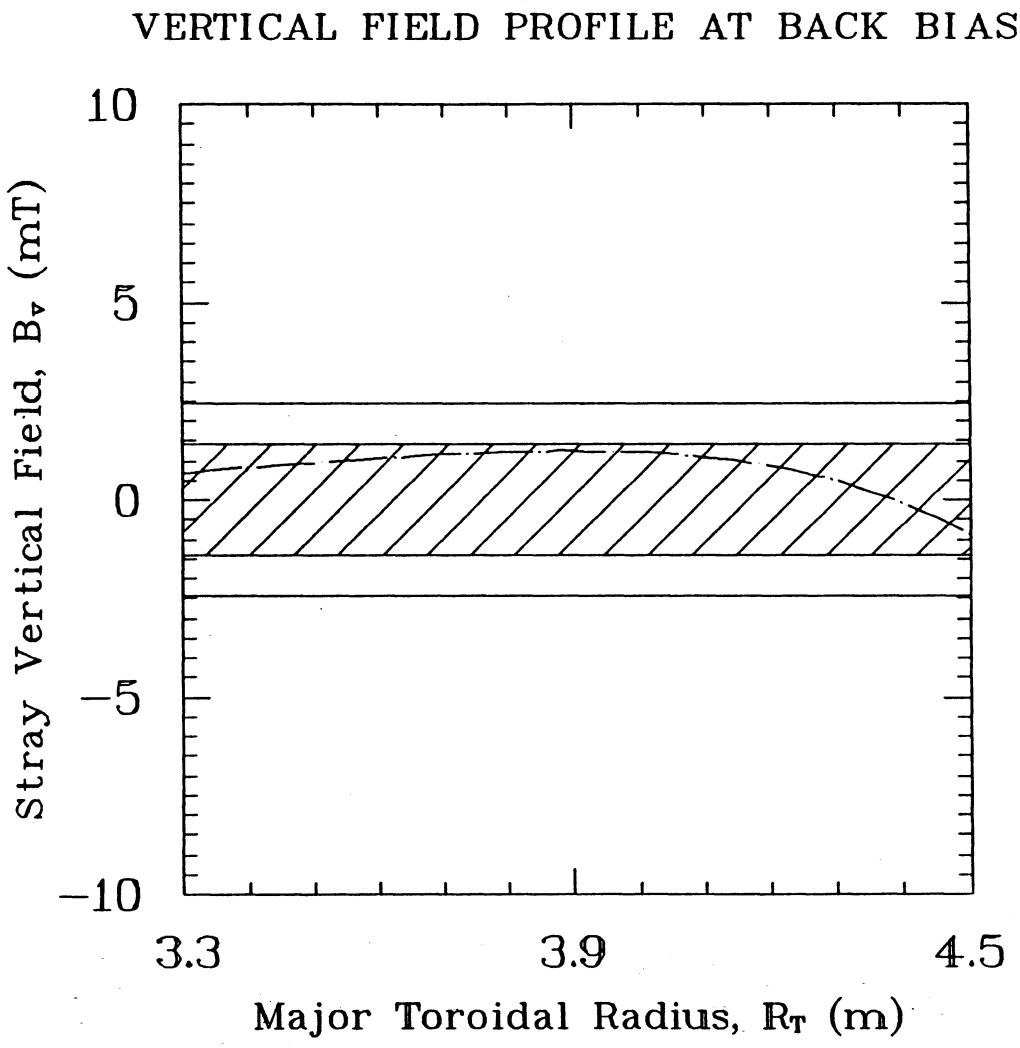


Fig. 4.4.-3. The stray-vertical-field profile in the equatorial plane for the close-fitting OHC configuration shown in Fig. 4.4.-1. Also shown are the bands for the allowed vertical field when the field null is on axis (clear) and when the field null is off-axis (shaded) as is the case for the close-fitting configuration.

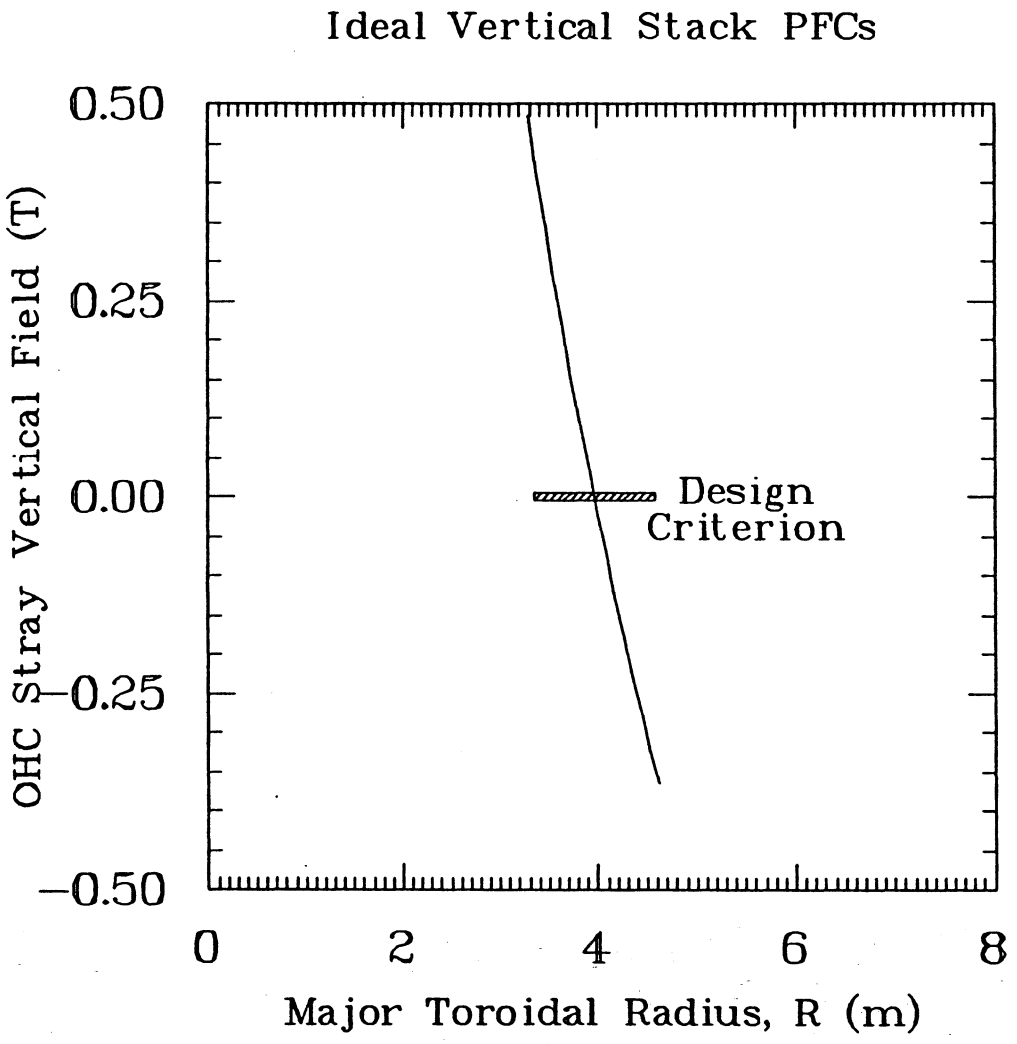


Fig. 4.4.-4. The stray-vertical-field profile in the equatorial plane for the vertical-stack configuration shown in Fig. 4.4.-2. Also shown is a 5 mT band to calibrate the extent of the violation of the stray vertical field constraint. Note the different scales than used in Fig. 4.4.-3.

which in turn causes magnetic islands within the edge-plasma region. Particles and energy flow freely within this island structure, density or temperature gradients cannot exist radially across the islands and, depending on island size, plasma confinement is degraded. To ensure that confinement is not adversely affected by the ripple, the radial extent of the islands is required to be small compared to the radial distance between the reversal surface and the plasma surface. This region is thought [1] to be the most responsible for confinement in an RFP. Consequently, the management of the ripple is a major factor in the design of the TFCs and is addressed in this section.

The design issues associated with the toroidal-field ripple has led, in part, to the consideration of a second TFC option, the integrated blanket/coil (IBC) concept [47] (Sec. 8.2.5). The IBC concept combines blanket and TFC functions by using a liquid metal which breeds tritium to fulfill the blanket function, flows so it can remove the energy deposited within it, and conducts electricity to fulfill the TFC function. The combination of functions eliminates the need for coolant penetrations through the conductor. With the major penetrations eliminated, the TFC current channel approaches a continuous toroidal shell which introduces no toroidal-field ripple. However, the IBC has a number of non-magnetic issues, as discussed in Sec. 8.2.5.

An estimate of the magnetic-island size produced by a discretized copper TFC set is given by the following formula for the radial thickness of an island [52]:

$$\Delta r = 4 \left[ \frac{r \, \Delta B_R}{n \, B_\theta \, (dq/dr)} \right]^{1/2} , \qquad (4.4.-16)$$

where r is the minor radius of the resonant surface, $\Delta B_R$ is the amplitude of the radial magnetic-field perturbation, n is the toroidal mode number of the resonant surface, $B_\theta$ is the poloidal field at the resonance, and the derivative of the safety factor, dq/dr, is evaluated at the resonant surface. The q-profile in the edge-plasma region can be taken to be linear:

$$\frac{dq}{dr} = \frac{q}{r_p - r_r} , \qquad (4.4.-17)$$

where $r_r$ and $r_p$ are the minor radii of the reversal and plasma surfaces. Assuming that the toroidal mode number of the resonance is equal to the number of TFCs, $N_{TF}$, the island-width criterion becomes

$$\frac{\Delta r}{r_p} \simeq 4 \left[ \frac{\Delta B_R (1 - r_r/r_p)}{N_{TF} B_\theta \, q} \right]^{1/2} < (1 - r_r/r_p) \; . \qquad (4.4.-18)$$

An estimate of the radial magnetic field arising from the ripple, $\Delta B_R$, can be obtained from two-dimensional field-line tracings at the plasma surface with only the TFCs simulated. Such simulations [46] have yet to be performed for the TITAN design and are also of limited application because $N_{TF}$ must exceed 100 before the primary resonance, $N_{TF}^{-1}$, appears within the plasma for the 18 MW/m$^2$ strawman design (Sec. 5.3.2) and Eq. (4.4.-16) becomes applicable. If the resonant surface is not in the plasma, there will be no islands in the plasma with a toroidal mode number of $N_{TF}$. However, islands resulting from higher order resonances may be present and are best uncovered by three-dimensional field-line tracings.

A more accurate assessment of island widths can be obtained from three-dimensional field-line tracings which simulate the toroidal, radial, and poloidal components of the magnetic field produced by the plasma, PFCs, and TFCs. Although such simulations remain to be done for this study, previous simulations [53] indicate that islands can be kept acceptably small if $\Delta B_R / B_\theta < 0.003$, which is the criterion used for the ZT-H design [54]. Scaling the number of TFCs from that design with aspect ratio, $A = R_T/r_p$, indicates that $N_{TF} \geq 28$ is required for the 18 MW/m$^2$ strawman design. Using the largest rectangular cross-sectional coils that will fit into the space allocated for the TFCs results in the preliminary TFC design shown in Fig. 4.4.-5 and described in Table 4.4.-IV. This design with $N_{TF} = 28$ will accommodate four or seven divertors that are equally spaced toroidally. If five or six divertors are needed to meet a divertor heat-load limit, then a minimum of $N_{TF} = 30$ is required to achieve equal spacing of the divertors. Note that the current density in the TFCs for this preliminary design is higher than predicted by the systems code in Sec. 5.3.2: 35.9 MA/m$^2$ compared to 17.4 MA/m$^2$. This increase in current density is the result of using coils with a rectangular cross section as opposed to specifying a radial build and assuming toroidal symmetry, as was down for the systems code (Sec. 5.2). The loss of conductor cross-sectional area

TABLE 4.4.-IV

PRELIMINARY TFC DESIGN PARAMETERS

| Parameter | Value | |
|---|---|---|
| Number of TFCs, $N_{TF}$ | 28 | |
| Major radius, $R_{TF}$ (m) | 3.892 | (3.892) |
| Minor radius, $r_{TF}$ (m) | 1.431 | (1.438) |
| Radial thickness (mm) | 12.8 | (26.0) |
| Toroidal thickness (mm) | 548.0 | (545.0) |
| Current per coil (kA) | 251.6 | |
| Current density ($MA/m^2$) | 35.9 | (17.8) |
| Total ohmic power (MW) | 65.0 | (32.3) |

Values in the parentheses are the results of increasing the radial space allocated for the TFCs from 0.028 m (Sec. 5.3) to 0.041 m.

results in a doubling of the ohmic power dissipated in the TFCs over that predicted by the systems code. The current density value of 17.4 $MA/m^2$, predicted by the systems code, can be recovered if the TFCs are made thicker in the radial direction by 0.013 m as indicated in Table 4.4.-IV. The effect of thicker the TFCs upon the PFC design should be negligible.

## 4.5. PLASMA/CIRCUIT SIMULATION

Early RFP reactor studies [46,53,55,56] have taken guidance from the results of (steady-state) parametric system models (Sec. 5) to provide initial conditions to a time-dependent, plasma/circuit simulation code that in turn models the start-up, approach to, achievement of, and maintenance of DT ignition. These early ignition/burn simulations generally assumed the existence of a low-current RFP "target" plasma ($I_\phi \simeq 0.1$ MA, $T \simeq 0.1$ keV, $n \leq 10^{20}$ $m^{-3}$, $F \simeq -0.1$, $\Theta \simeq 1.5$) onto which a bipolar OHC swing was imposed to ramp the plasma to an ohmic ignition.

Figure 4.5.-1 illustrates the general start-up scenario assumed [46], with the bulk of the start-up energy being provided from the electrical grid; power and voltage requirements were appropriately constrained, as were OHC back-bias stresses needed to provide all poloidal flux (inductive and resistive) requirements. Hence, the TF and OH coil and power supply designs are coupled through the formation process by the breakdown constraint ($B_V/B_{\phi o}$), reversal time, $\tau_R$, poloidal-flux consumption during formation ($\tau_R$, $B_{\phi o}$, geometry), and

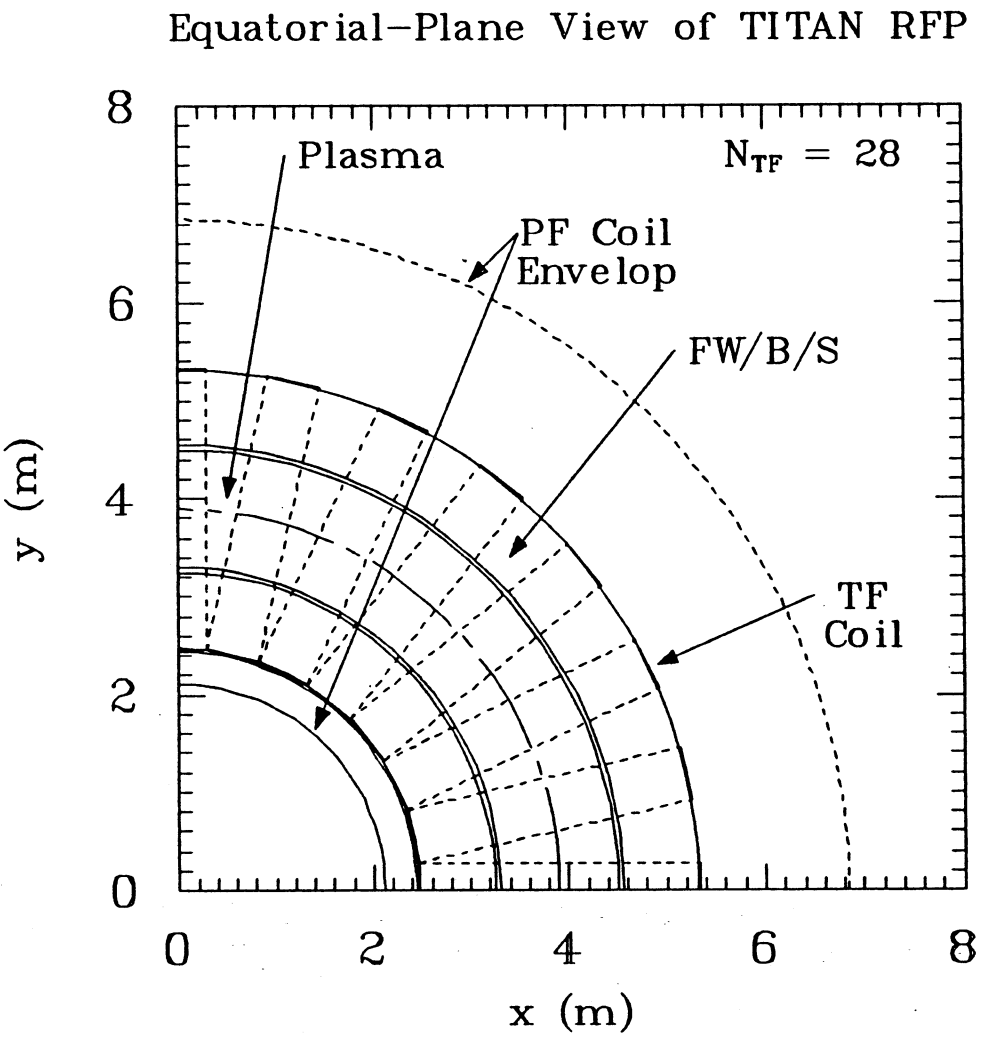


Fig. 4.4.-5. An equatorial-plane view of a quadrant of the preliminary TFC design. Also shown are the first wall, blanket, and shield assembly (FW/B/S), the plasma, and the poloidal-field (PF) coil envelope.

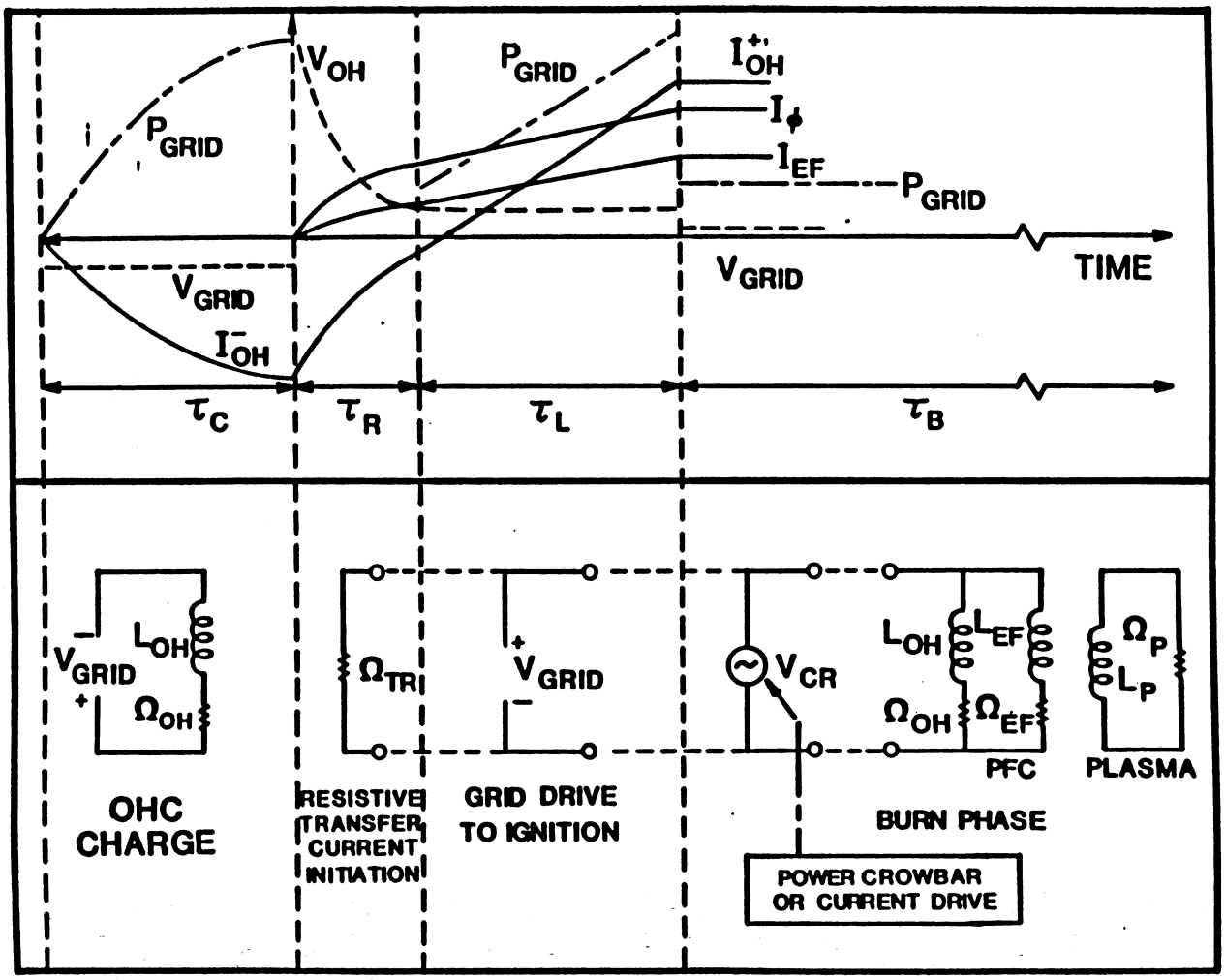


Fig. 4.5.-1. Schematic diagram of a simplified RFP start-up scenario showing the following start-up stages: OHC charge, resistive flux transfer and current transfer to the plasma, grid drive to ignition, and burn, followed by OFCD to sustained power generation.

the degree of subsequent toroidal-flux generation possible by the RFP dynamo. Existing experimental evidence has been summarized, primarily from ZT-40M [57], and used to establish RFP breakdown/formation "windows" to estimate coil and circuit parameters and to provide initial conditions for the current ramp to ohmic ignition and burn. Fig. 4.5.-2 schematically depicts a more detailed view of the RFP start-up, with Sec. 4.5.1 dealing primarily with this formation phase.

It became evident towards the end of the early RFP reactor studies [46,53] and during the earliest phase of the TITAN study that both the TFC and PFC (OHC + EFC) design limits would be determined more by the plasma breakdown, formation, and ramp-up transients than by the steady-state operational phase. The desire to use the RFP dynamo to generate internal toroidal flux, rather than injecting all the toroidal flux by the TFCs, and the bias stress and power strongly influence the TFC and OHC designs. Furthermore, the PFC configuration determines the coupling of OHC with the plasma, the magnitude of the stray vertical field, and the degree of multipolarity of field nulls in the plasma chamber. These in turn influence the breakdown and RFP formation conditions through the amount of initial (vacuum) toroidal field, $B_{\phi o}$, and ultimately affect the TFC design.

Section 4.5.1 describes and applies the existing RFP experimental data base for RFP breakdown and formation. Using the initial RFP conditions generated in Sec. 4.5.1, the plasma start-up (ramp-up → ignition → burn) is simulated by means of a zero-dimensional plasma/circuit model in Sec. 4.5.2. Recent developments to model eddy-current effects in the engineering structure that surrounds the RFP are given in Sec. 4.5.3.

### 4.5.1. Breakdown and RFP Formation

A body of experimental data is beginning to accumulate, which better defines the formation "window" and associated PFC/TFC circuit requirements for the TITAN reactor, as well as for other RFP devices [58,59]. Although, much of this information is not theoretically understood fully and extrapolation from ZT-40M-class experiments to a reactor is uncertain, this information and experience nevertheless is assimilated for the first time and used as part of the TITAN study. The formation phase is shown schematically on Fig. 4.5.-3, which gives more detail than shown in Fig. 4.5.-2 as well as introducing key notation. Generally, matched-mode RFP formation is assumed, wherein the RFP is externally driven to match exactly the reversed toroidal field generated by the

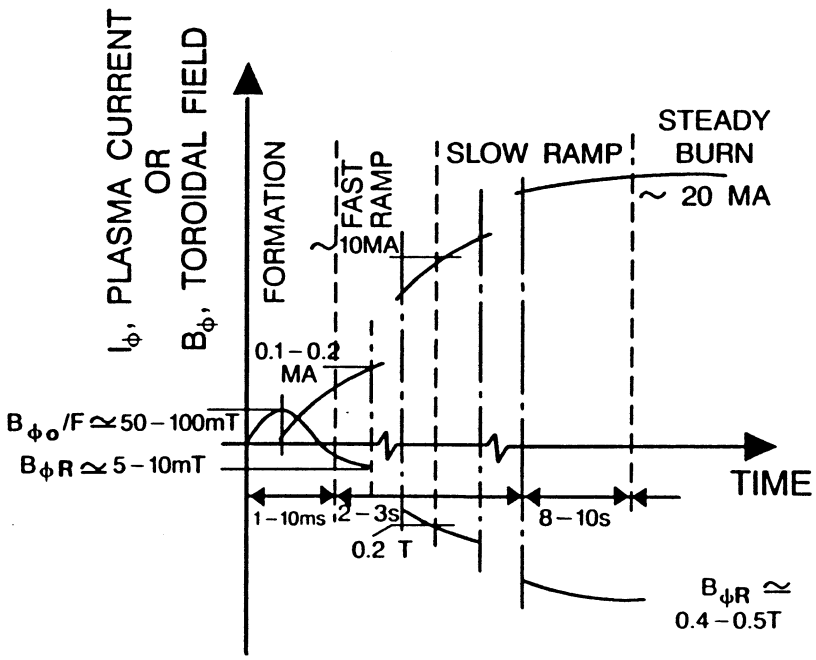


Fig. 4.5.-2. Schematic diagram of RFP start-up phases.

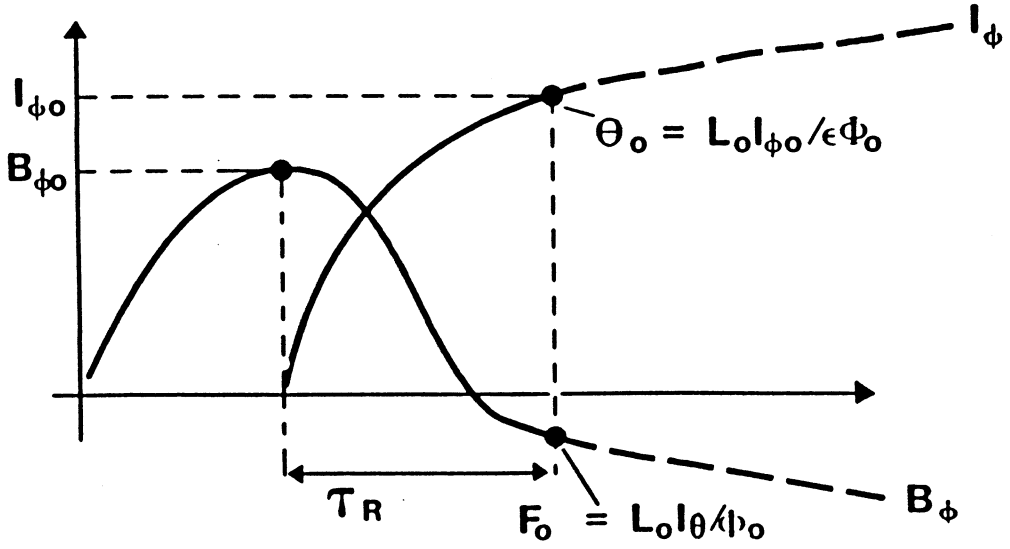


Fig. 4.5.-3. Matched-mode RFP formation leading to the initial conditions, $\Theta_o$, $F_o$, and $I_{\phi o}$ used as initial conditions for start-up, ignition, and burn simulations.

plasma (no toroidal flux change across TFCs). The formation phase of the RFP is characterized by the following experimentally observed behaviors:

- upper and lower density limits define a region outside of which poor or no RFP formation occurs.
- minimum plasma current (or possibly current density, in that size variations are limited in present-day experiments) below which robust RFPs cannot be formed.
- minimum limit on the toroidal electric field, $E_\phi$, or ratio of $E_\phi$ to initial filling pressure, $E_\phi/P_o$, to ensure breakdown.
- upper limit on the formation time, $\tau_R$.
- limits imposed on initial (vacuum) toroidal bias magnetic field, $B_{\phi o}$.

In addition to setting windows for RFP formation, relationships between these variables and the poloidal flux and energy consumption during formation have been derived [57]. These constraints are briefly summarized in the following subsections and formulated into a simplified breakdown and formation model (Sec. 4.5.1.12) that in turn is evaluated to provide initial conditions for the simulation of plasma start-up, ignition and burn (Sec. 4.5.2).

4.5.1.1. Plasma Breakdown

Plasma discharge and subsequent RFP formation generally occurs for values of the ratio of toroidal electric field to initial filling pressure, $E_\phi/P_o$, that are similar to tokamak values and generally are close to electron runaway condition. For example, JET reports [60] $E_\phi/P_o \geq 0.66\times10^4$ V/m torr compared to $1\text{-}2\times10^4$ V/m torr, for ZT-40M [57], which is very close to electron runaway condition. Fig. 4.5.-4 gives typical breakdown/formation characteristics for a range of tokamaks [61] and for ZT-40M. Generally, breakdown and discharge formation is not a problem for RFPs, but the degree of pre-ionization can greatly influence the discharge quality and poloidal-flux consumption [62]. Since stable RFP formation to date appears to require a high initial filling density for the levels of density pump-out experienced in present-day RFPs the generally common $E_\phi/P_o$ values for both RFPs and tokamaks give significantly higher values of $E_\phi$ required to initiate a robust RFP.

4.5.1.2. Stray-Vertical-Field Constraint

As shown in Fig. 4.5.-5, a toroidal field line of strength $B_{\phi o}$ in the presence of a vertical field $B_V$ will intersect the first wall and prevent the

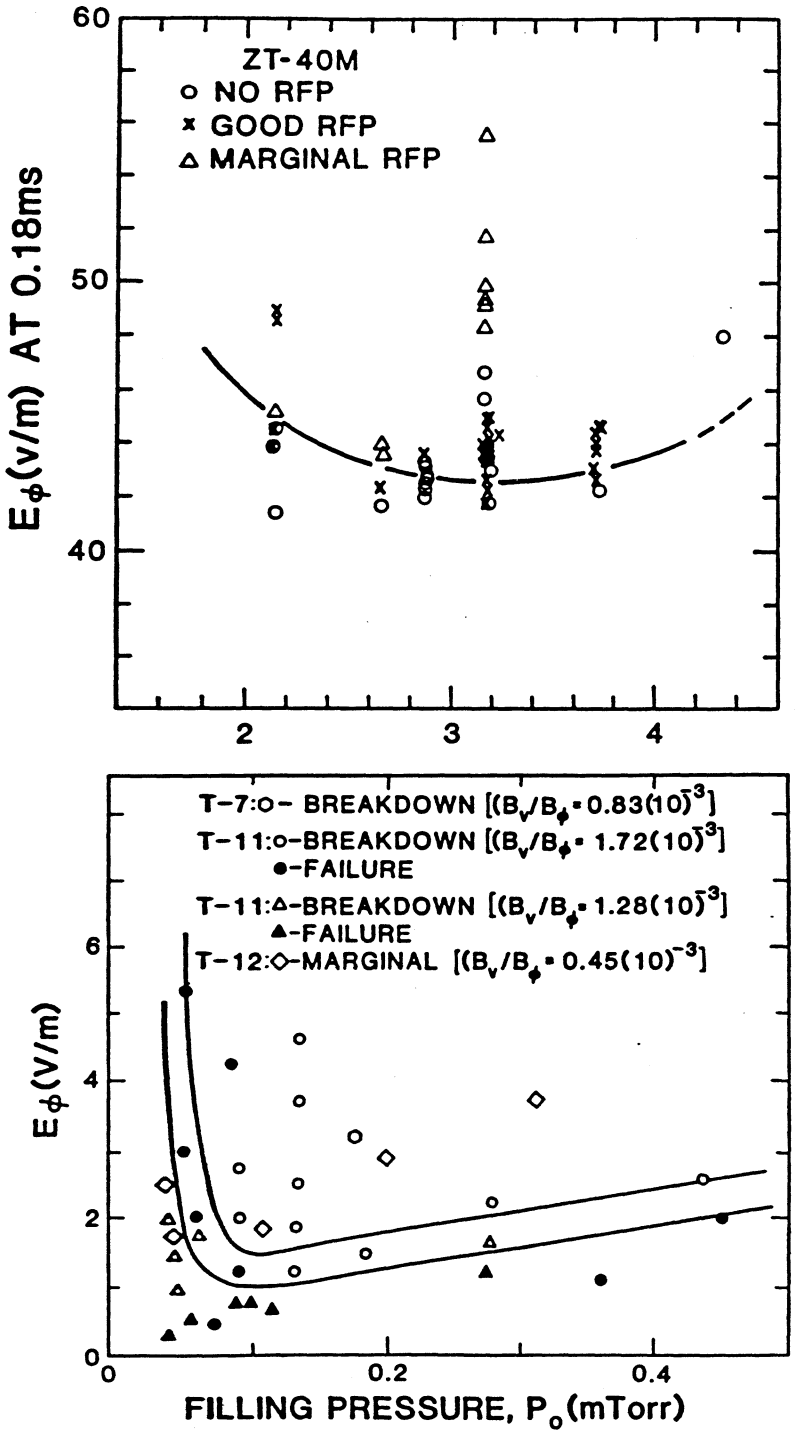


Fig. 4.5.-4. Typical breakdown curves for a) tokamak [61] and b) RFP [57] formation.

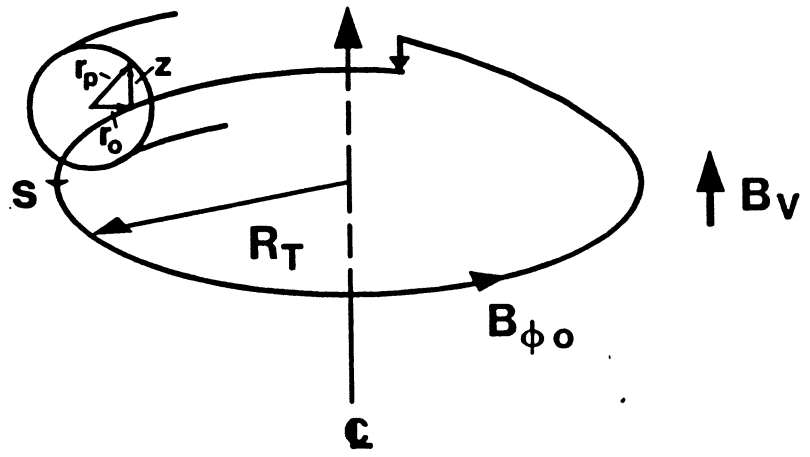


Fig. 4.5.-5. Schematic illustration of a field line in the presence of a vertical field.

formation of a continuous discharge if the ratio $B_V/B_{\phi o}$ is too large. The condition for the confinement of a single toroidal trajectory with a field null at a minor radial position $r_o$ is given by

$$\frac{B_V}{B_{\phi o}} \leq \frac{\varepsilon}{2\pi}\left[1 - (\frac{r_o}{r_p})^2\right]^{1/2} , \qquad (4.5.-1)$$

where $\varepsilon = r_p/R_T$ is the inverse aspect ratio. In addition, a drift constraint has been suggested for JET [60]:

$$E_\phi/(B_V/B_{\phi o}) \geq 10^3 \text{ V/m} . \qquad (4.5.-2)$$

The value of $B_V$ and the field-null(s) locations are determined from a vacuum-field calculation using the CCOIL model described in Sec. 4.4.2.

4.5.1.3. Initial Toroidal Flux Constraint

Once the $B_V/B_{\phi o}$ constraint is established, the relationships between $B_{\phi o}$ and the average toroidal flux within the initial RFP, $\langle B_\phi \rangle$, and hence, $F_o$, must be determined (Fig. 4.5.-3). Generally, for matched-mode RFP formation $\langle B_\phi \rangle \simeq B_{\phi o}$. Figure 4.5.-6 shows the relationship between $B_{\phi o}$ and $\langle B_\phi \rangle$ for a range of ZT-40 discharges [57,63] illustrating the experimental basis for this assumption. Given that $\langle B_\phi \rangle$ can be determined and the initial pinch parameter, $\Theta_o$, is specified, the initial (minimum) RFP current or current density (given $r_p$) is determined from the following:

$$I_{\phi o} = 5 r_p \Theta_o \langle B_\phi \rangle \ . \qquad (4.5.-3)$$

4.5.1.4. Initial Current-Density Constraint

Although Eq. (4.5.-3) gives a means to determine a current density that is consistent with the vertical-field constraint previously described, other, more dominant constraints may exist. For example, the ZT-40M experiment exhibits a minimum-current density limit, which translates to $j_{\phi o} \geq 0.4$ MA/m$^2$, below which RFP formation is difficult. Although not well understood, the application of such a constraint to the TITAN represents a conservative connection to experiment. Secondly, a number of RFP experiments [1] have shown an impurity burn-through constraint, typical of which is shown in Fig. 4.5.-7 for ZT-40M. For these conditions, burn-through requires

$$\frac{j_\phi}{n} \geq 6 \times 10^{19} \text{ MA-m} \ . \qquad (4.5.-4)$$

4.5.1.5. Minimum-Density Constraints

Generally if for a given initial filling pressure the pump-out of density is too great prior to toroidal field reversal, unreliable RFP formation occurs [57], as is shown in Fig. 4.5.-8a. Similarly, for a given initial filling pressure, $P_o$, a maximum initial bias field $B_{\phi o}$ is found above which RFP formation does not occur [57], as is shown in Fig. 4.5.-8b. Although RFPs form at lower values of $B_{\phi o}$, these RFPs require excessive poloidal-flux consumption,

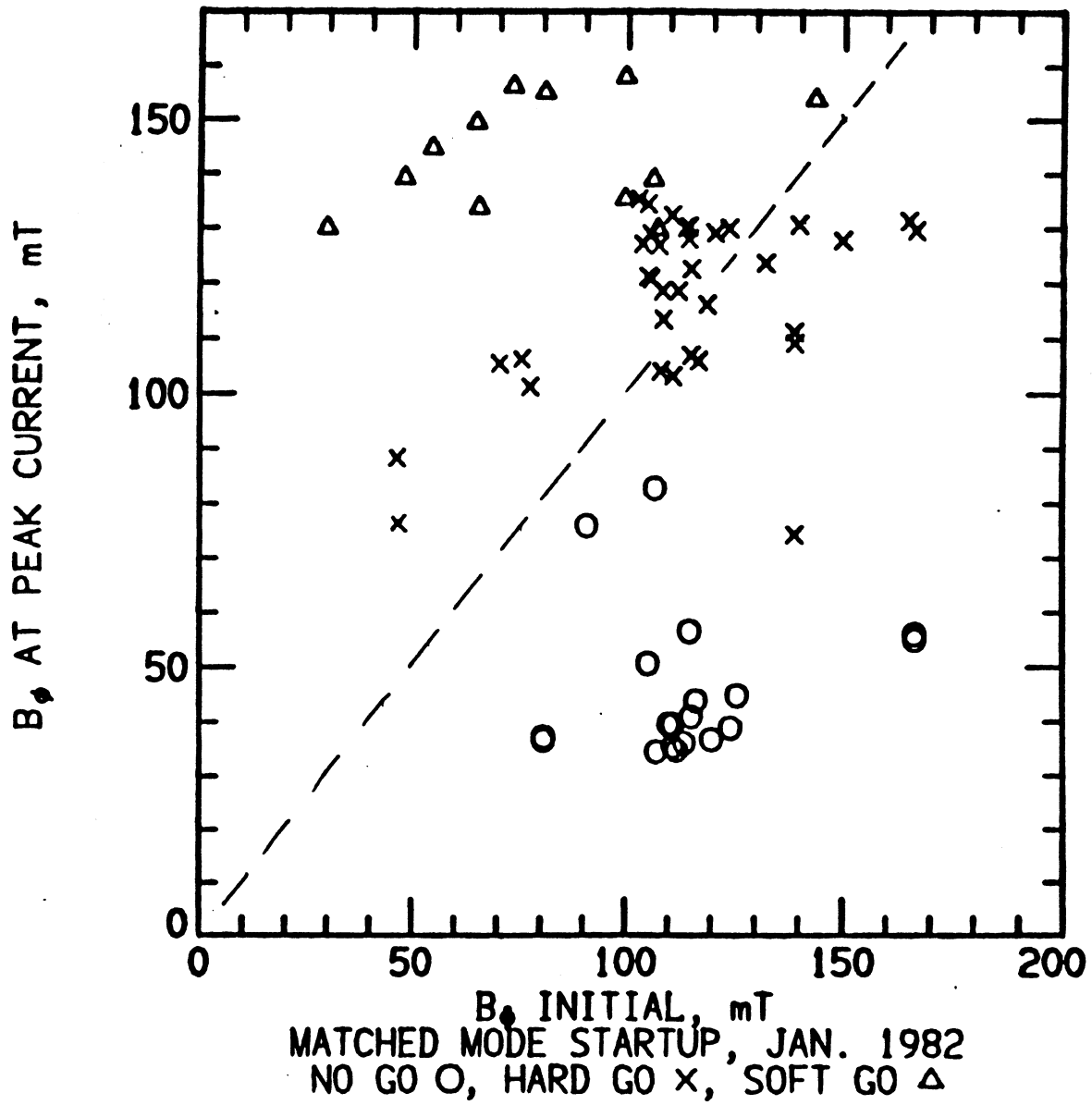


Fig. 4.5.-6. Relationship between $B_{\phi o}$ and $\langle B_\phi \rangle$ for a range of ZT-40M discharges [57,63] where robust RFP formation occurred, as well as no RFP formation as very shallow, spheromak-like, RFP were formed.

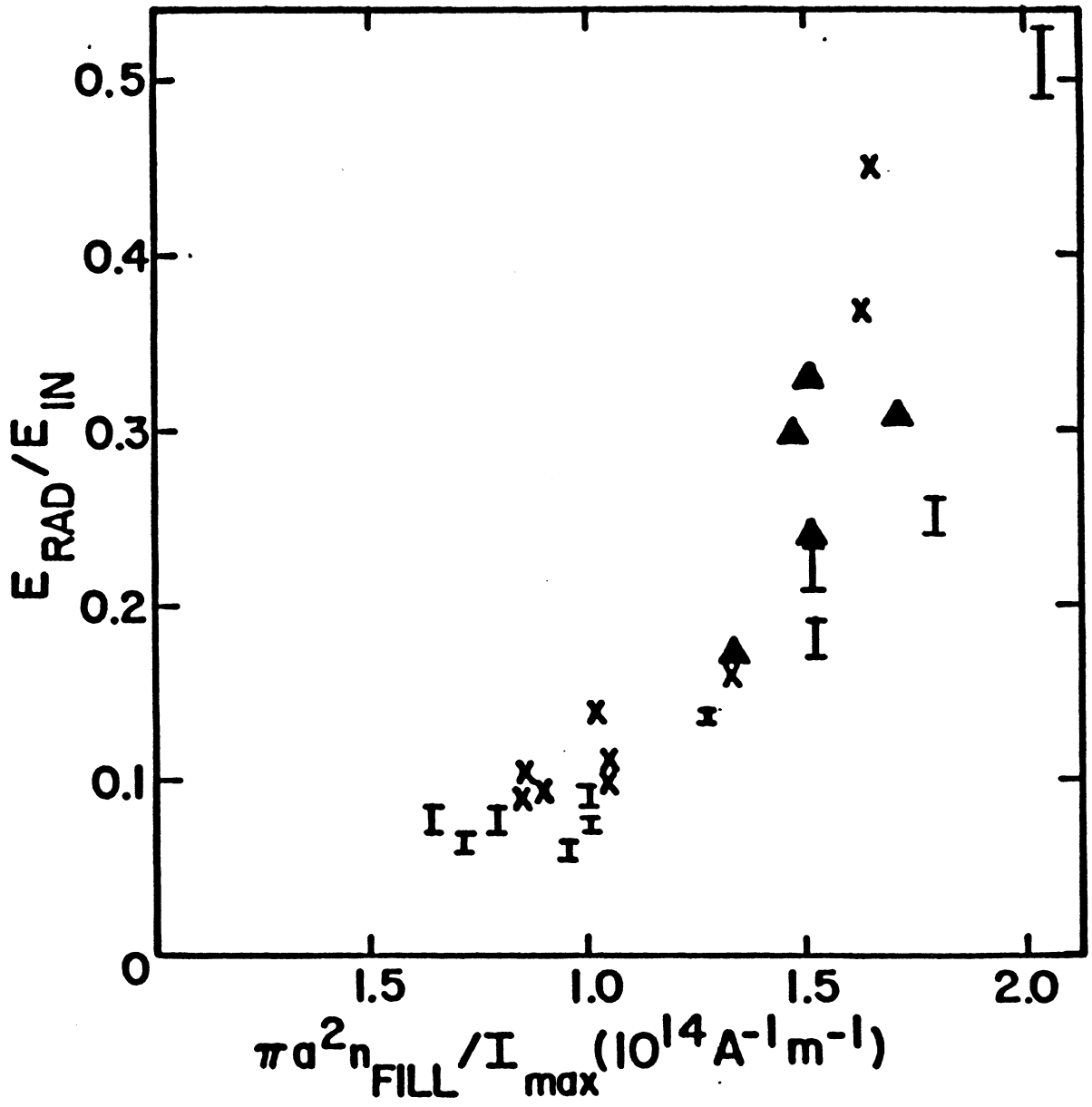


Fig. 4.5.-7. Impurity-burn-through constraint for ZT-40M [57].

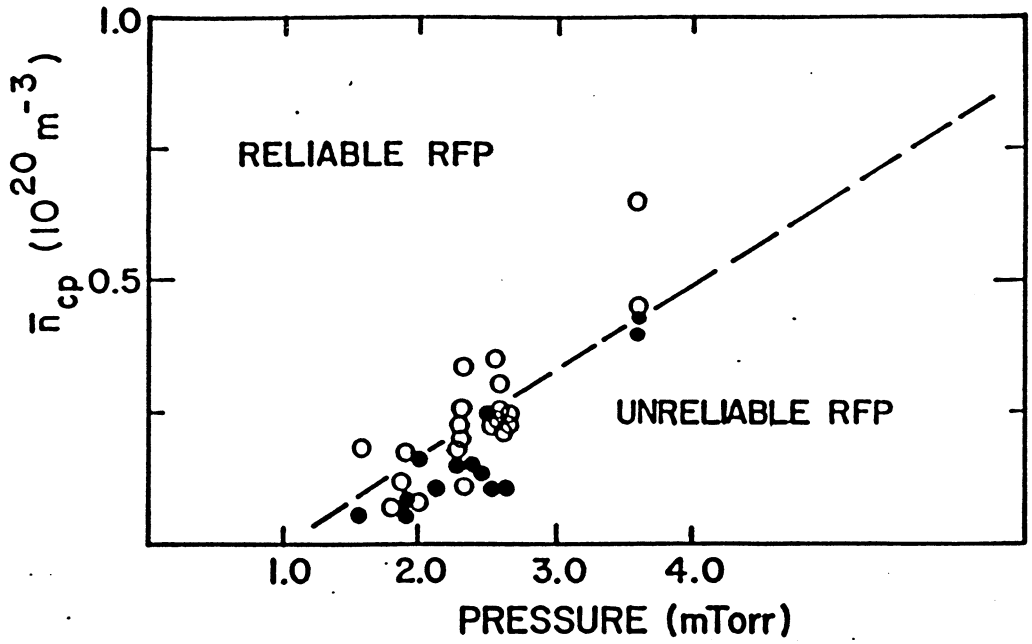


Fig. 4.5.-8a. Relationship between filling pressure and degree of pump-out, below which poor RFP formation is observed [57].

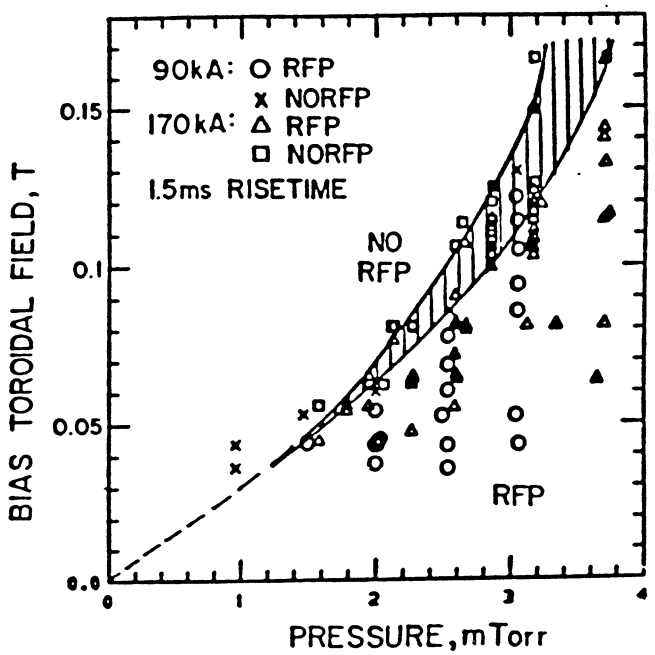


Fig. 4.5.-8b. Initial toroidal bias fields above which no RFP formation is found for a given filling pressure in ZT-40M [57].

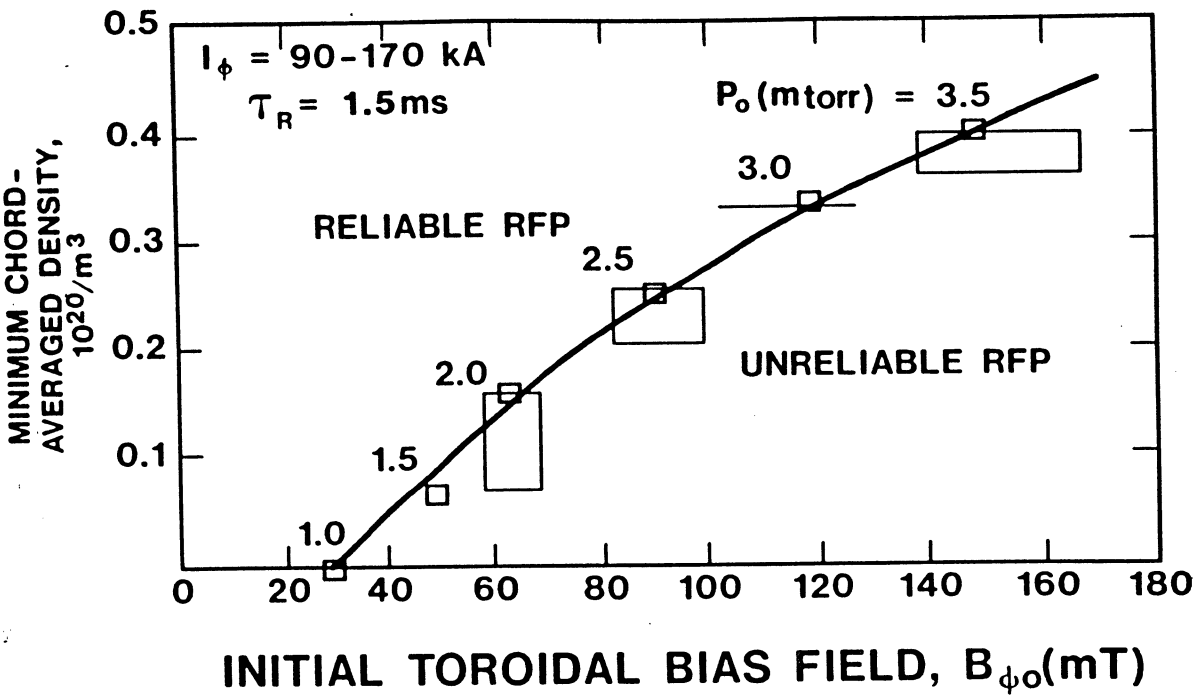


Fig. 4.5.-8c. Cross-correlation plot of Figs. 4.5.-8a and 4.5.-8b.

with Fig. 4.5.-8b showing a "horn of plenty" for the ZT-40M conditions examined. It should be noted that a variable and poorly controlled wall condition creates hystereses and related unknown effects in many of these data correlations. Figures 4.5.-8a and 4.5.-8b have been combined in Fig. 4.5.-8c in an attempt to eliminate the filling-pressure variable and perhaps to reduce the impact of these unresolved wall effects on the data. The result is a relationship between average plasma density and initial bias field that is forced to assure robust RFP formation. The cross-correlation plot given in Fig. 4.5.-8c is fitted with the following functions to give the critical density, $n_c$ versus $B_{\phi o}$ relationship.

$$n_c\ (10^{20}\ m^{-3}) = 0.10 \qquad \text{for } B_{\phi o} < 36\ mT$$

$$n_c\ (10^{20}\ m^{-3}) = 2.78\times10^{-3}\ B_{\phi o} \qquad \text{for } B_{\phi o} > 36\ mT \qquad (4.5.-5)$$

4.5.1.6. Reversal Parameter

Generally, $\Theta_o$ and the initial poloidal beta, $\beta_{\theta o}$, are specified as independent goals or targets, and, along with the assumption of a $\mu$ profile (e.g., modified Bessel function model), the appropriate F-$\Theta$ or Taylor diagram is determined. This derived F-$\Theta$ diagram for the assumed initial $\beta_{\theta o}$ and $\mu(r)$ values, then determines $F_o$.

4.5.1.7. Density Pump-out

The degree of density reduction between the initial filling pressure and the final RFP formation is poorly understood and strongly dependent on wall preconditioning. Hence, the pump-out is treated parametrically in terms of the ratio of initial filling density, $n_o$, to the final RFP plasma density $n > n_c$. The assumption is made that pump-out and $P_o$ can be minimized, thereby minimizing $E_\phi$ at start-up.

4.5.1.8. Toroidal Electric Field

The toroidal electric-field constraint, $E_\phi/P_o$, was discussed earlier in Sec. 4.5.1.1 in terms of breakdown and discharge formation. In characterizing the TITAN initial conditions, the following four possible constraints were considered:

$$E_\phi/P_o \text{ (V/m torr)} = 0.66\times10^3 \qquad \text{(JET breakdown)}$$

$$E_\phi/(B_V/B_{\phi o}) \text{ (V/m)} = 10^3 \qquad \text{(JET drift)}$$

$$E_\phi/P_o \text{ (V/m torr)} \leq 10^4 \qquad \text{(electron runaway)}$$

$$E_\phi/P_o \text{ (V/m torr)} \simeq 2\times10^4 \qquad \text{(ZT-40M)} \qquad (4.5.-6)$$

Hence, four sets of results are presented according to the above four possibilities.

4.5.1.9. Initial Current Risetime

Neglecting compressional and resistive voltages during the initial phase ($I_{\phi o} \simeq 0$) of the RFP formation, the current risetime is approximated by the sinusoidal, inductive wave form to give the following expression for $\tau_R$:

$$\frac{I_{\phi o}}{\tau_R} \simeq \frac{2}{\pi} \frac{V_{\phi o}}{L_p} \ , \qquad (4.5.-7)$$

where $V_{\phi o} \simeq E_\phi 2\pi R_T$,

$$L_p = \mu_o R_T \left[ \ln \left( \frac{8R_T}{r_p} \right) - 2 + l_i \right] \ , \qquad (4.5.-8)$$

and the plasma internal inductance per unit length, $l_i = 1 - (2F + 1)(1 - F)/2\Theta^2$ for the Bessel-function model, or $l_i \simeq 1$ for the modified Bessel-function model. For the ZT-40M experiment, $I_{\phi o}/\tau_R \simeq$ 30-40 MA/s. The risetime $\tau_R$ should then be compared to an effective shell/liner time-constant, $\tau_L = \mu_o r_w \delta_L / 2\eta_L$, where $r_w$ is the first-wall radius of thickness $\delta_L$ and electrical resistivity $\eta_L$.

4.5.1.10. Poloidal-Flux and Energy Consumption During RFP Formation

Figures 4.5.-9a and 4.5.-9b give the dependence of poloidal-flux and energy consumption as a function of initial current risetime for ZT-40M [57]. Separating the resistive and inductive components of the flux consumption and correcting for geometry while using the following expression for plasma resistivity at formation [57]:

$$\eta_{AV} \ (\Omega m) = 1.4 \frac{r_p^2}{R_T \ I_{\phi o}^{0.64}} \ , \qquad (4.5.-9)$$

the flux consumption during formation becomes

$$\int_o^{\tau_R} V_\phi dt = L_p I_{\phi o} + 9.04 \times 10^3 \ R_T \ I_{\phi o}^{0.36} \frac{\tau_R}{r_p^{0.72}} \ , \qquad (4.5.-10)$$

where $L_p$ is again given by Eq. (4.5.-8) using the modified Bessel function model. The associated energy consumption is given by

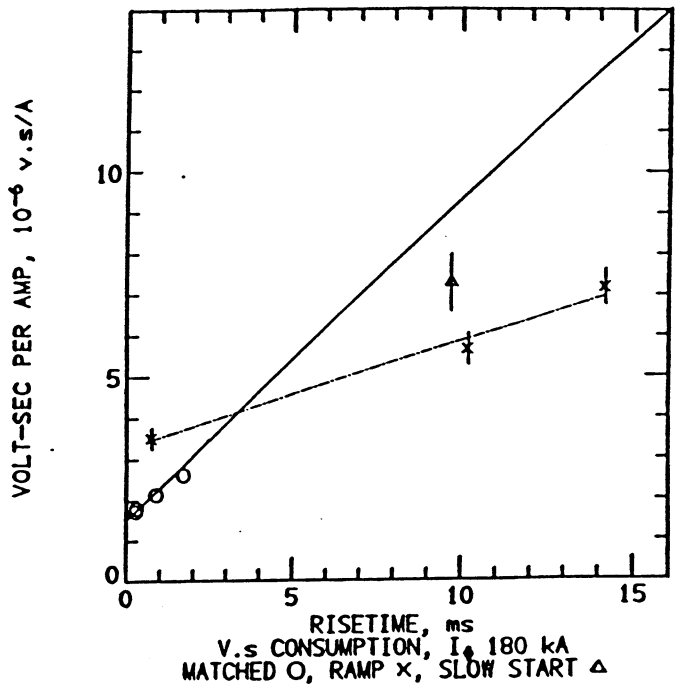


Fig. 4.5.-9a. Flux consumption during formation as a function of risetime for ZT-40M.

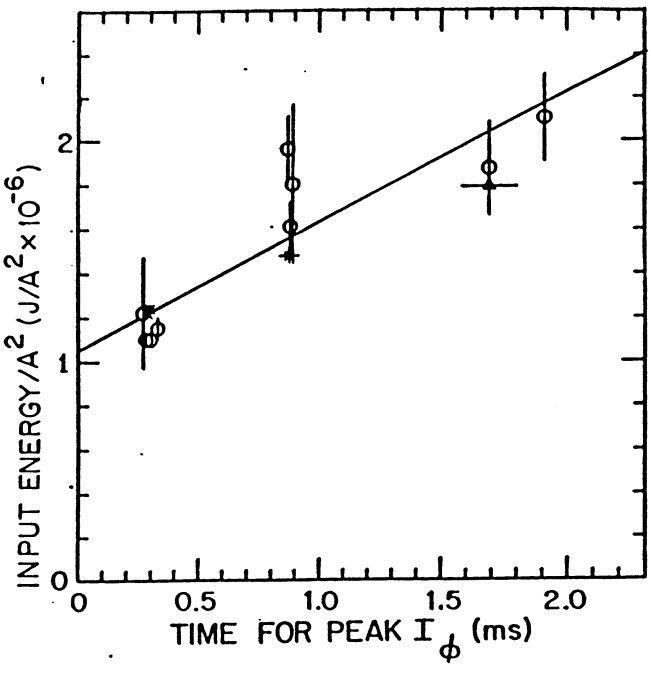


Fig. 4.5.-9b. Energy consumption during formation as a function of risetime for ZT-40M.

$$W_{B\phi} = \frac{1}{2} I_{\phi o} \int_{o}^{\tau_R} V_{\phi} dt \ . \qquad (4.5.-11)$$

4.5.1.11. Toroidal-Field Coil During Formation

Given the current-radius of the TFC, $r_{TF}$, and the parameters self-consistently determined from the previous subsections, the toroidal flux, $\Phi$, and associated single-turn TFC voltage, $V_\theta \simeq d\Phi/dt$, can be estimated from the following expression

$$V_\theta(V/m) = \frac{\pi r_p}{5\Theta_o} \left\{ \frac{B_{\phi o}}{\langle B_\phi \rangle} - 1 + \left( \left[ \frac{r_{TF}}{r_p} \right]^2 - 1 \right) \left( \frac{B_{\phi o}}{\langle B_\phi \rangle} - F_o \right) \right\} \frac{I_{\phi o}}{\tau_R} \ . \qquad (4.5.-12)$$

From this expression, the stored energy and required TFC circuit power can be readily obtained.

4.5.1.12. Calculational Algorithm and Preliminary Result

The set of constraints and/or options suggested in the previous eleven subsections has been combined into a calculation format and algorithm shown on Fig. 4.5.-10. The overall procedure begins with cost-optimized estimates provided by the parametric systems analysis (PSA) model (Sec. 5). This first geometry estimate is fed to the CCOIL code (Sec. 4.4), which estimates all aspects of the PFC configuration based on poloidal-flux balance and bipolar start-up. In addition to back- and forward-biased currents, inductances, and coil positions, CCOIL provides the multipolarity and vertical-field characteristics of a given (optimized) OHC set that is then used in the aforementioned formation model. The time-dependent plasma/circuit simulation code, which uses CCOIL output, then is used to gain a more accurate estimate of PFC flux consumption and associated back-biased stress and power consumption. As shown at the top of Fig. 4.5.-10, a closely coupled interaction between the PSA, CCOIL and BURN codes provides a well converged estimate of the TITAN design prior to examination and optimization of the formation phase described in this section. The sequence shown in Fig. 4.5.-10 is then followed, leading to a

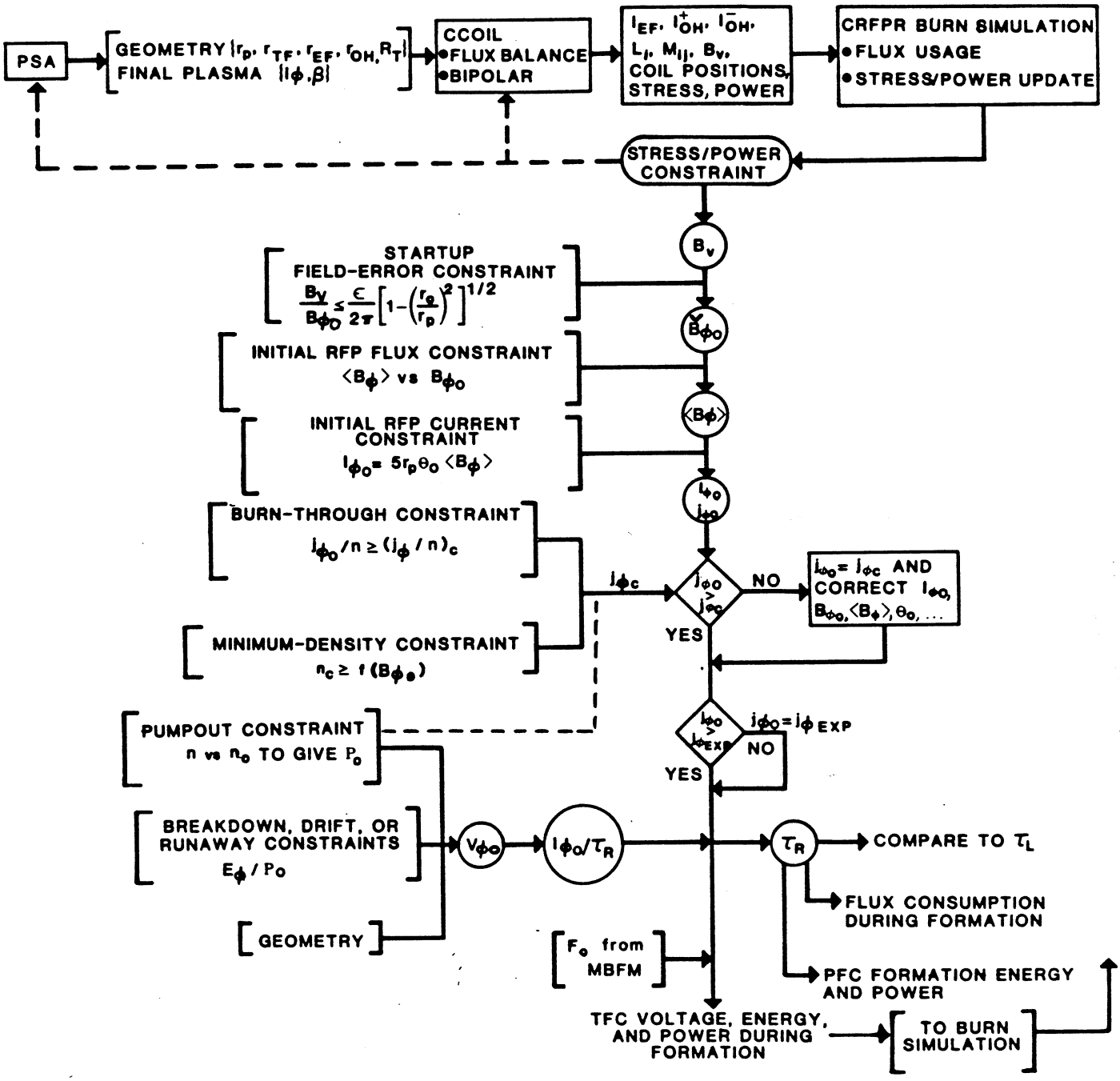


Fig. 4.5.-10. Calculational algorithm for the self-consistent determination of TITAN RFP formation conditions.

design for the TFC and OHC as dictated by RFP formation, that may or may not require further optimization through the PSA → CCOIL → BURN sequence.

Generally, the constraints imposed by the RFP formation physics, when combined, give the following global constraints on $\tau_R$, $n/n_o$, and $V_\theta/V_\phi$:

$$\tau_R \geq \frac{708\pi}{4} r_p^2 \frac{L_p}{R_T} \frac{(10^{20}\, j_\phi/n_o)_c}{E_\phi/P_o} , \qquad (4.5.-13a)$$

$$\frac{n}{n_o} \geq \frac{2.78}{5\Theta_o} r_p (10^{20}\, j_\phi/n_o)_c , \qquad (4.5.-13b)$$

$$\frac{V_\theta}{V_\phi} = \frac{2r_p}{L_p\Theta_o} \left[\frac{B_{\phi o}}{\langle B_\phi \rangle} - 1 + \left(\left(\frac{r_{TF}}{r_p}\right)^2 - 1\right)\left(\frac{B_{\phi p}}{\langle B_\phi \rangle} - 1\right)\right] . \qquad (4.5.-13c)$$

For the four possible means to determine $E_\phi/P_o$ listed in Eq. 4.5.-6, Table 4.5.-I gives the physics and device parameters and the associated start-up conditions. The (JET) "drift" or the "runaway" conditions listed in Table 4.5.-I are considered most typical of present-day experiments and are used as initial conditions for the start-up, ignition, and burn simulation of the TITAN design objective given in the following section.

A main objective of the foregoing analysis is to estimate the impact of stray vertical field on the RFP formation requirements. Using the fourth column in Table 4.5.-I as a baseline, the computational algorithm summarized in Fig. 4.5.-10 was exercised while varying $B_V$. The impact of increasing $B_V$ on the flux, energy, and power consumption is shown in Fig. 4.5.-11, with the design value being $B_V \simeq 2.5$ mT. Since the resistive poloidal-flux consumption during the full ramp-up to ignition and burn is ~ 25 Wb (~ 10% to total), an additional flux consumption during formation much above this value becomes a concern from the viewpoint of back-bias stress in the OHCs. Hence, $B_V$ much above a few milli-tesla should be avoided.

## 4.5.2. Plasma Start-up to Ignition and Burn

### 4.5.2.1. Model and Initial Conditions

The preliminary results given in Table 4.5.-I for the RFP formation phase have been used to estimate initial conditions for the simulation of the current

TABLE 4.5.-I

RFP FORMATION PARAMETERS FOR TITAN

| BASIC PHYSICS DATA | Breakdown | Drift | Runaway | $j_\phi$(exp) (0.4 MA/m$^2$) |
|---|---|---|---|---|
| $E_\phi/P_o$ (kV/m/torr) | 6.66 | 4.01 | 1.00 | 1.00 |
| $\eta_{Cu}$ ($\mu\Omega$m) | 0.0388 | 0.0388 | 0.0388 | 0.0388 |
| $\eta_{SS}$ ($\mu\Omega$m) | 0.358 | 0.358 | 0.358 | 0.358 |
| $\langle B_\phi \rangle / B_{\phi o}$ | 1.00 | 1.00 | 1.00 | 1.00 |
| $n_c$ ($10^{20}$ m$^{-3}$) | 0.25 | 0.25 | 0.25 | 0.28 |
| $n/n_c$ | 1.00 | 1.00 | 1.00 | 1.00 |
| $n$ ($10^{20}$ m$^{-3}$) | 0.25 | 0.25 | 0.25 | 0.28 |
| $n_o/n$ | 1.00 | 1.00 | 1.00 | 1.00 |
| $n_o$ ($10^{20}$ m$^{-3}$) | 0.25 | 0.25 | 0.25 | 0.28 |
| $P_o$ (mtorr) | 0.35 | 0.35 | 0.35 | 0.39 |
| $j_\phi/n$ ($10^{-20}$ MAm) | 1.00 | 1.00 | 1.00 | 1.43 |
| **MACHINE PARAMETERS** | | | | |
| $R_T$ (m) | 3.90 | 3.90 | 3.90 | 3.90 |
| $r_p$ (m) | 0.60 | 0.60 | 0.60 | 0.60 |
| $r_o$ (m) | 0.4892 | 0.4892 | 0.4892 | 0.4892 |
| $F_o$ | -0.10 | -0.10 | -0.10 | -0.10 |
| $\beta_{\Theta o}$ | 0.10 | 0.10 | 0.10 | 0.10 |
| $\Theta_o$ | 1.523 | 1.50 | 1.50 | 1.50 |
| $\delta_{SLD}$ (m) | 0.050 | 0.050 | 0.050 | 0.050 |
| $\delta_{BLK}$ (m) | 0.775 | 0.775 | 0.775 | 0.775 |
| $\delta_{TFC}$ (m) | 0.028 | 0.028 | 0.028 | 0.028 |
| $B_v$ (mT) | 1.2484 | 1.2484 | 1.2484 | 1.2484 |
| $\Delta I_{OH}$ (MA) | 47.96 | 47.96 | 47.96 | 47.96 |
| $R_{OH}$ ($\mu\Omega$) | 0.297 | 0.297 | 0.297 | 0.297 |

TABLE 4.5.-I (Continued)

| START-UP CONDITIONS | Breakdown | Drift | Runaway | $j_\phi$(exp) (0.4 MA/m$^2$) |
|---|---|---|---|---|
| $B_v/B_{\phi o}$ constraint | 0.014 | 0.014 | 0.014 | 0.013 |
| $B_v/B_{\phi o}$ (update) | 0.014 | 0.014 | 0.014 | 0.013 |
| $B_{\phi o}$ (mT) | 88.1 | 88.1 | 88.1 | 100.0 |
| $B_\phi$ (mT) | 88.1 | 88.1 | 88.1 | 100.0 |
| $B_{\theta o}$ (mT) | 132.1 | 132.1 | 132.1 | 150.0 |
| $B_{\phi R}$ (mT) | 8.8 | 8.8 | 8.8 | -10.0 |
| $I_{\phi o}$ (MA) | 0.40 | 0.40 | 0.40 | 0.45 |
| $E_\phi$ (V/m) | 2.30 | 14.18 | 3.46 | 3.93 |
| $V_\phi$ (V) | 56.4 | 347.4 | 84.7 | 96.2 |
| $L_p$ (μH) | 13.9 | 13.9 | 13.9 | 13.9 |
| $dI_\phi/dt$ (MA/s) | 2.6 | 15.9 | 3.9 | 4.4 |
| Max. circuit dI/dt (MA/s) | 10.2 | 10.2 | 10.2 | 10.2 |
| $\tau_R$ (ms) | 153.4 | 24.9 | 102.2 | 1,454.40 |
| RESULTS | | | | |
| Constant resistivity | | | | |
| • flux consumption (Wb) | 13.95 | 6.88 | 11.13 | 12.14 |
| • formation energy (MJ) | 4.44 | 1.64 | 3.32 | 4.06 |
| • formation power (MW) | 28.93 | 65.62 | 32.49 | 39.70 |
| • $j_{\phi o}$ (MA/m$^2$) | 0.35 | 0.35 | 0.35 | 0.40 |
| • $j_{\phi c}$ (MA/m$^2$) | 0.25 | 0.25 | 0.25 | 0.40 |
| Constant resistivity and $j_\phi$ | | | | |
| • flux consumption (Wb) | 39.94 | 11.11 | 28.44 | 30.26 |
| • formation energy (MJ) | 14.73 | 33.09 | 10.18 | 12.21 |
| • formation power (MW) | 96.09 | 13.28 | 99.66 | 11.95 |
| $\delta_L^{Cu}$ (mm) | 14.6 | 2.4 | 9.7 | 9.7 |
| $\delta_L^{SS}$ (mm) | 134.4 | 21.8 | 89.5 | 89.5 |
| $E_\phi B_{\phi o}/B_V > 1000$ (V/m) | 162.49 | 1000.00 | 243.95 | 314.527 |
| $j_{\phi o}/n_o$ ($10^{-20}$ MAm) | 1.43 | 1.43 | 1.43 | 1.43 |
| $v_D/v_{TH} < 0.01$ | 0.0076 | 0.0076 | 0.0076 | 0.0071 |
| $V_\theta$ (V/turn) | 3.44 | 20.89 | 5.10 | 5.79 |
| $W_\theta$ (kJ) | 85.5 | 85.5 | 85.5 | 110.3 |
| $P_\theta$ (MW) | 0.56 | 3.43 | 0.83 | 1.1 |

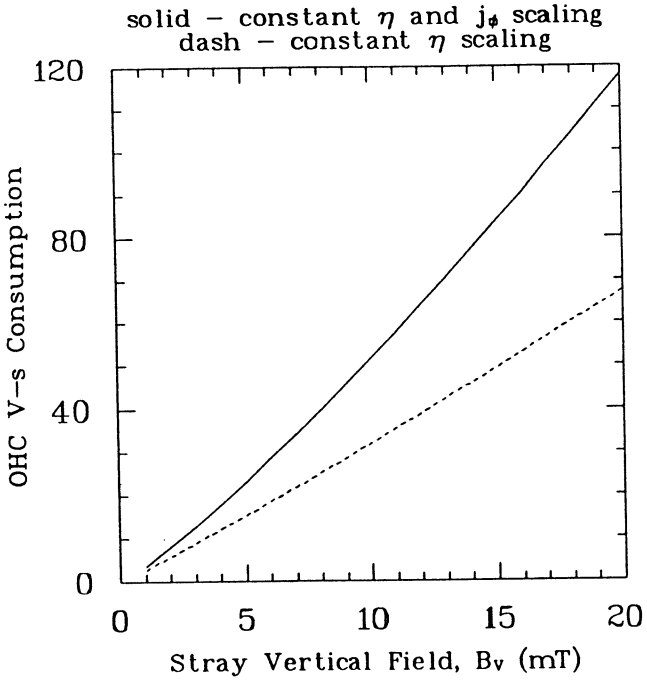


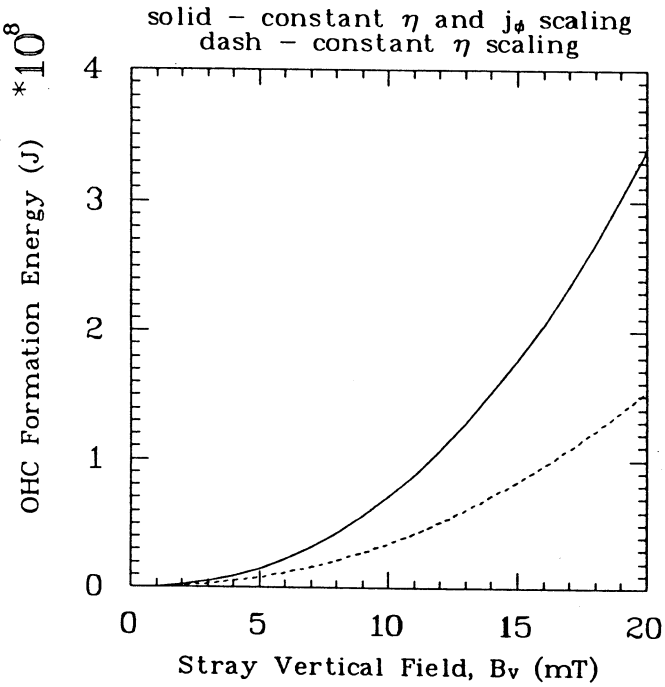


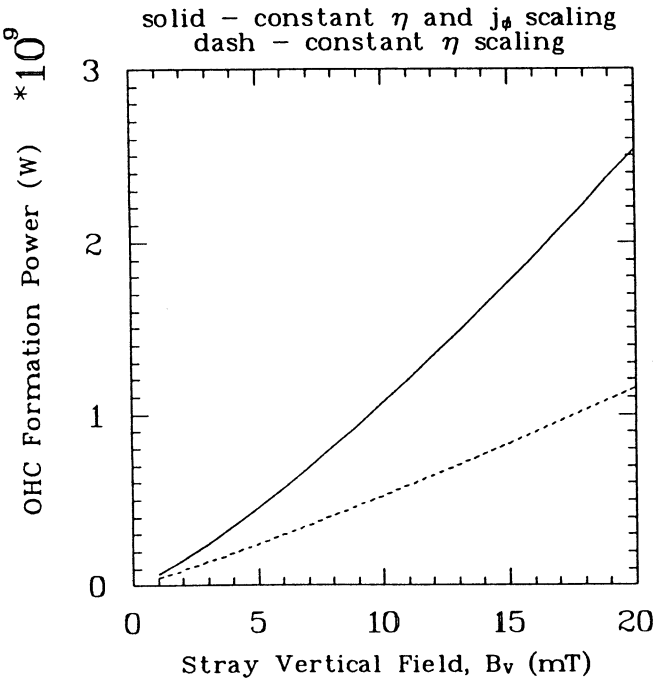


Fig. 4.5.-11. Dependence of formation flux, energy and power consumption on stray vertical field.

ramp-up to ohmic ignition and burn. Table 4.5.-II summarizes these initial conditions. The time-dependent plasma/circuit simulation code models the post-formation fast current ramp-up (few seconds to $I_\phi \simeq 10$ MA) followed by a slower ramp, driven from the grid, to plasma ignition and burn at $I_\phi = 18$-20 MA (Fig. 4.5.-2). The BURN code has been described in detail elsewhere [46,53]; a summary is given in Table 4.5.-III. The results of this zero-dimensional plasma simulation are compared with the one-dimensional MHD simulation in Sec. 4.7.1.

4.5.2.2. Results

The basic results from the zero-dimensional plasma/circuit simulation code are given in Figs. 4.5.-12. The start-up trajectory is shown on the F-$\Theta$ diagram in Fig. 4.5.-12a, which targets a design value of $\Theta$ and subsequent $\beta_\Theta$ variations cause F to decrease. More recent simulations target on the F value and that allows $\Theta$ to drift upward somewhat as beta increases in order to minimize and/or control the impact of formation and start-up on the TFC requirements.

The time-dependent plasma simulation requires that both electron and ion confinement times be specified. As discussed in Sec. 5.2.1, a scaling of the form,

$$\tau_{ce} = C_\nu I_\phi^\nu f(\beta_\Theta/\beta_{\Theta c}) \qquad (4.5.\text{-}13a)$$

$$\tau_{pi} \simeq 4\tau_{ce} , \qquad (4.5.\text{-}13b)$$

is used, wherein, $f(\beta_\Theta/\beta_{\Theta c})$ simulates the experimentally observed RFP beta limited confinement. For the simulation, it is assumed that $f(\beta_\Theta/\beta_{\Theta c}) \simeq (\beta_\Theta/\beta_{\Theta c})^m$ with $\beta_{\Theta c} = 0.19$ and $m = 8$. This assumption results in a strong pinning of the plasma beta upon ohmic ignition, but the electrons and ions decouple somewhat in temperature, as is shown in Fig. 4.5.-12b. The various confinement times and powers, as well as $n\tau_E$, are shown as a function of time in Fig. 4.5.-12c. The fueling rate is controlled throughout the start-up to assure that either a) the streaming parameter, $\xi = v_D/v_{TH}$, remains below a specific value safe from electron thermal runaway, or b) that the fueling rate never exceeds three times the loss rate. The crucial fields and stress levels in the OHC are also shown on Fig. 4.5.-12d. The results shown in Fig. 4.5.-12, while indicating no serious problem with ohmic ignition and burn for the scaling used ($\nu = 1.0$), are not unique and will be subject to modification and re-

TABLE 4.5.-II

PLASMA STARTING CONDITIONS FOR BURN SIMULATIONS

| | |
|---|---|
| Ion, electron temperature, $T_{i,e}$ (keV) | 0.05 |
| Plasma/wall radius ratio, $x = r_p/r_w$ | 0.923 |
| Plasma current, $I_{\phi o}$ (MA) | 0.45 |
| Plasma current density, $j_{\phi o}$ ($MA/m^2$) | 0.40 |
| Plasma density, $n_{io}$ ($10^{20}$ $m^{-3}$) | 0.71 |
| Filling pressure, $P_o$ (mtorr) | 1.0 |
| Plasma kinetic energy, $W_{po}$ (kJ) | 43.1 |

TABLE 4.5.-III

SUMMARY OF RFP PLASMA/CIRCUIT SIMULATION AND DESIGN CODE

- Profile-averaged, zero-dimensional, time-dependent.
- Follows concentration and energies of species from consistent reactions (H, $^3$He, $^4$He, T), using Fokker-Planck slowing-down model and including Bremsstrahlung, cyclotron, and line radiation.
- Magnetic-field and current-density profiles computed consistent with assumed p(r) [i.e., n(r), T(r)] and $\mu(r)$ profiles.
- Pellet-refueling model (constant $I_\phi/N = j_\phi/n$).
- Complete analysis of PFC circuit, including plasma as a non-linear circuit element, with PFC circuit driving the simulation.
- One-dimensional thermal and stress analysis performed as a function of time for a composite first wall.
- Outputs:
  - Time-history of currents, voltages, powers, and energies in PFC and TFC circuits.
  - Self-consistent, 1-D equilibrium for given p(r) [i.e., n(r), T(r)], and $\mu(r)$, and associated profile factors for given T(r).
  - Time-history of all plasma parameters, including energetic ion species.
  - Complete reactor energy balance.
  - Time-dependent first-wall response.
  - Reactor parameter file for use in standardized reactor costing.

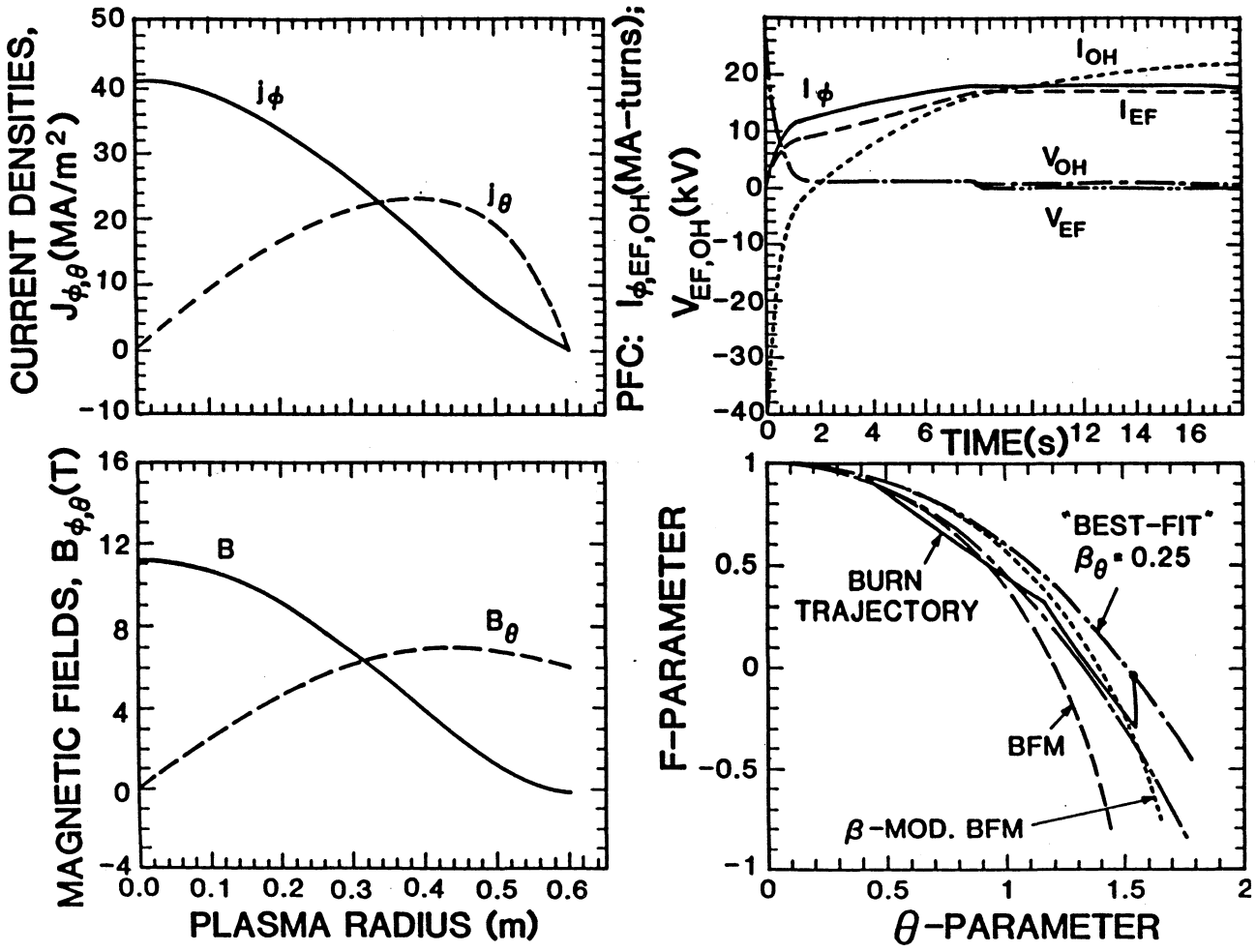


Fig. 4.5.-12a. Time-dependent results from zero-dimensional plasma/circuit simulation code for TITAN $I_w \simeq 18$ MW/m$^2$ "Strawman" design using the initial conditions given in Table 4.5.-III and the coil geometry shown in Fig. 4.4.-1.

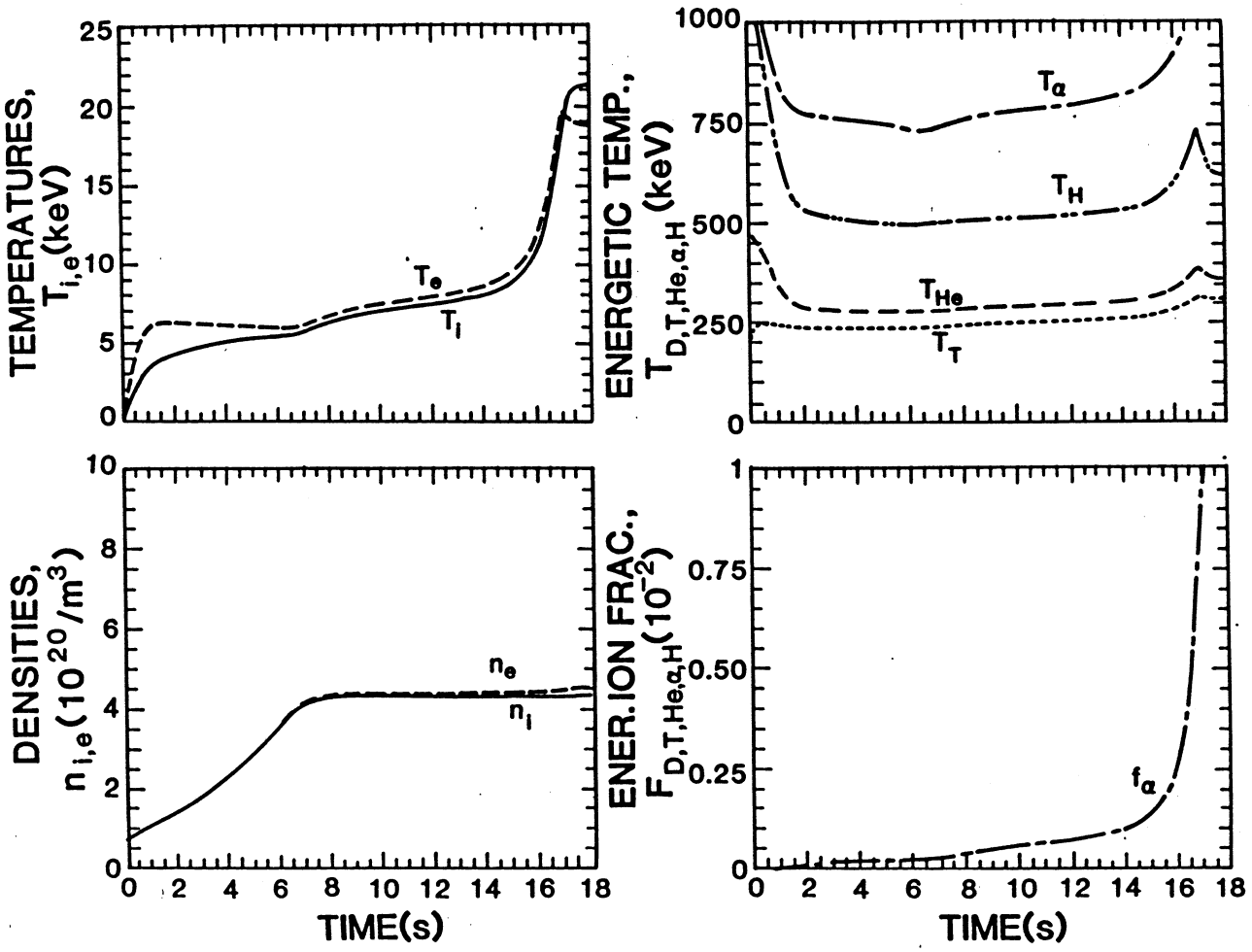


Fig. 4.5.-12b. Time-dependent results from zero-dimensional plasma/circuit simulation code for TITAN $I_W \simeq 18$ MW/m$^2$ "Strawman" design using the initial conditions given in Table 4.5.-III and the coil geometry shown in Fig. 4.4.-1.

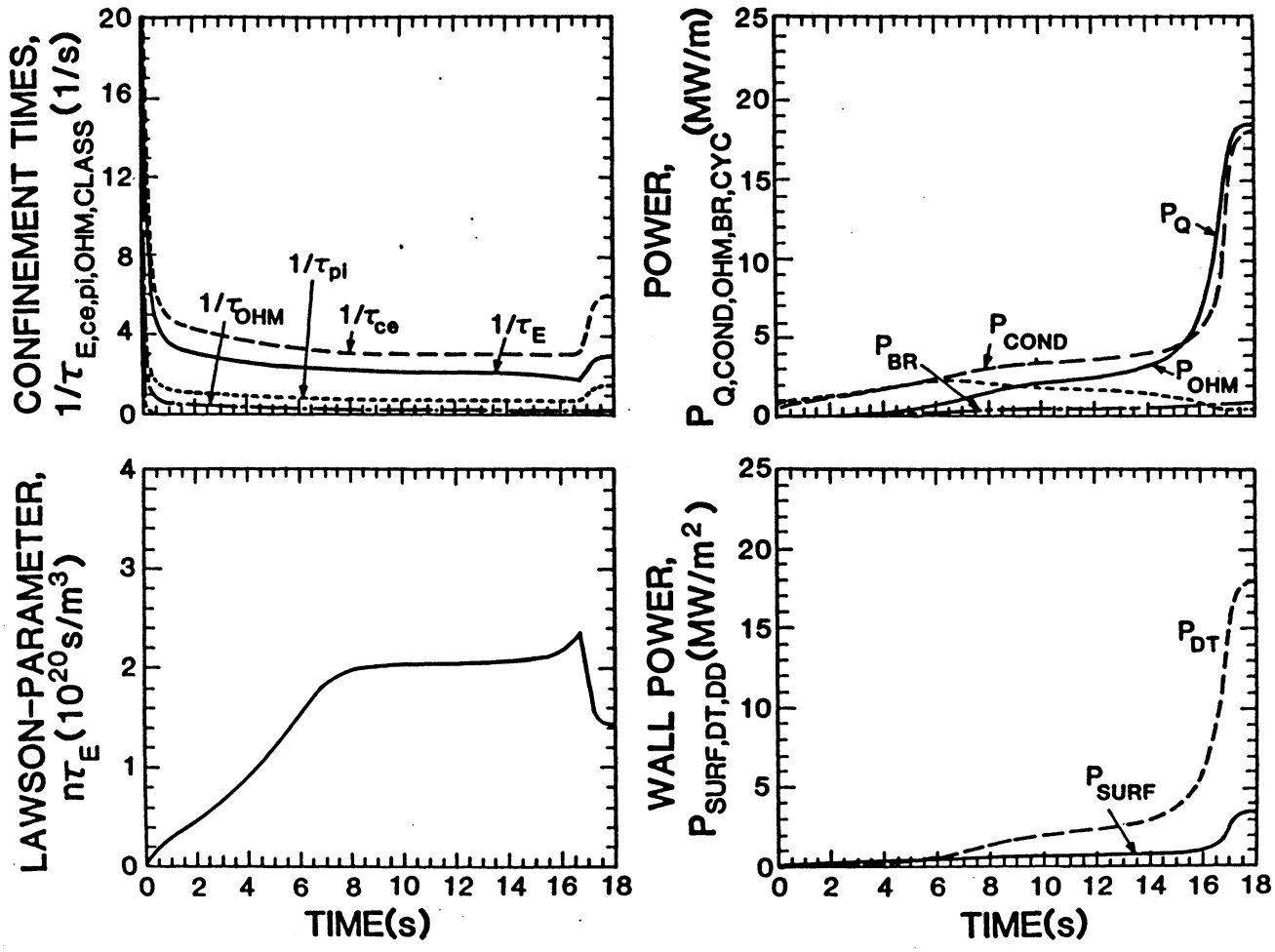


Fig. 4.5.-12c. Time-dependent results from zero-dimensional plasma/circuit simulation code for TITAN $I_W \simeq 18$ MW/m$^2$ "Strawman" design using the initial conditions given in Table 4.5.-III and the coil geometry shown in Fig. 4.4.-1.

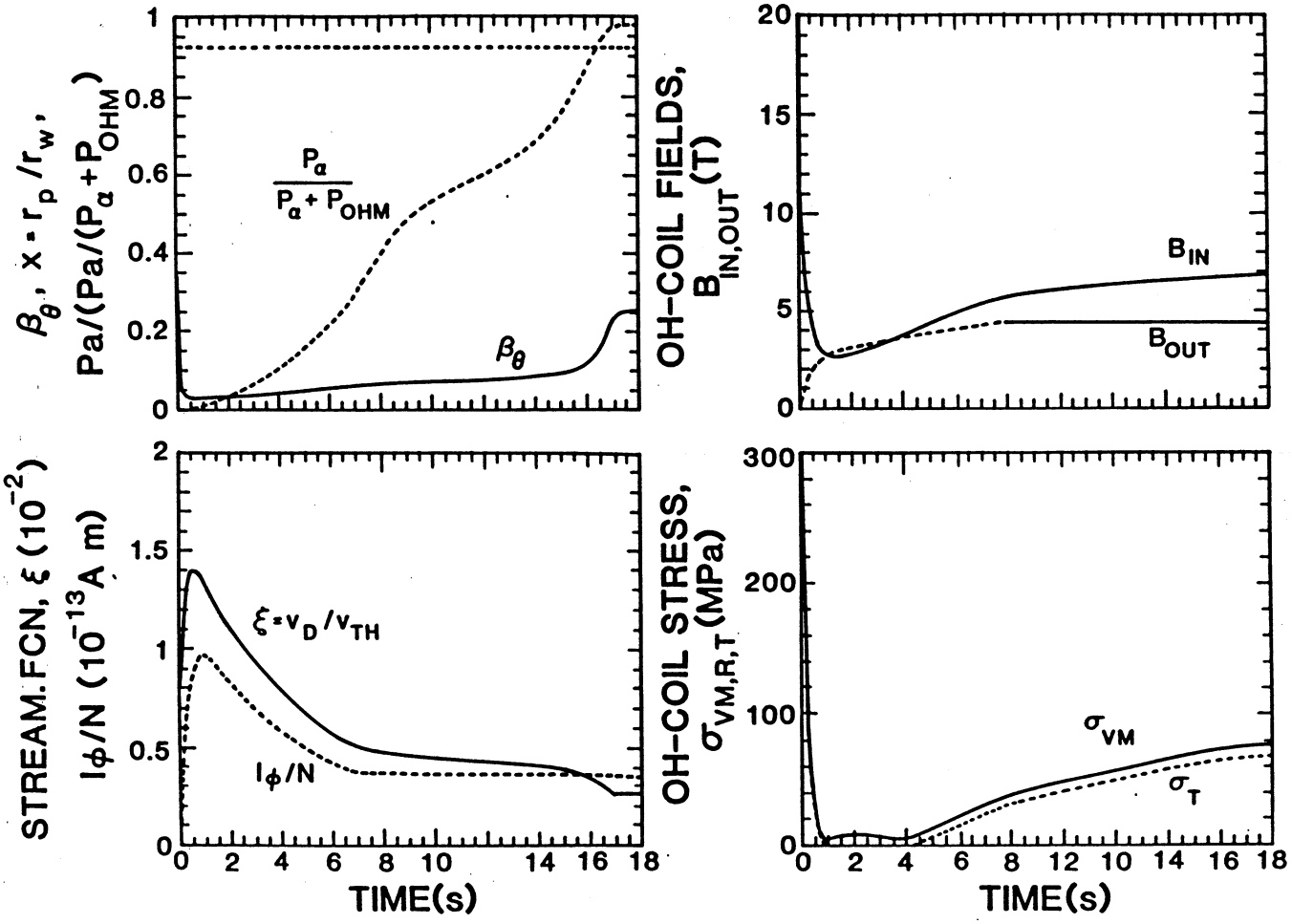


Fig. 4.5.-12d. Time-dependent results from zero-dimensional plasma/circuit simulation code for TITAN $I_W \simeq 18$ MW/m$^2$ "Strawman" design using the initial conditions given in Table 4.5.-III and the coil geometry shown in Fig. 4.4.-1.

optimization as new insight and understanding is developed in a range of crucial areas such as listed below:

- RFP formation
- current drive
- density (pellet) control
- impurity control (transients)

4.5.3. Eddy-Current Circuit Modeling

Analysis of plasma circuit interactions determines the plasma response to the externally applied fields. Such analyses are required so that appropriate switching sequences and voltages can be applied to the external circuitry (e.g., PF and TF coils) for various transient plasma operations, such as start-up and shut-down, fractional power operation, and OFCD.

The time-varying electromagnetic fields incurred during the plasma transients induce eddy currents in all conducting material surrounding the FPC, such as, the first wall, liner/conducting shell, vacuum vessel, blanket, shield, and structures. These eddy currents retard and modify the plasma response to externally applied magnetic fields. Furthermore, these eddy currents give rise to magnetic fields affecting the plasma equilibrium, to electromagnetic forces on all conducting materials which carry the eddy currents, and to an additional energy drain from the external circuits to compensate for Joule losses by eddy currents.

Eddy-current modeling is, therefore, a critical and usually the most difficult component of plasma-circuit interaction analyses. The approach to this problem, adopted for the TITAN study, is to divide the conducting material into small strips which simulate the actual eddy-current path and distribution. Each strip is modeled as an element of a complex circuit which also includes the external circuitry and the plasma as an equivalent circuit element. The interaction of these elements with each other is taken into account through the circuit-inductance matrix, $\vec{\vec{L}}$, containing self and mutual inductances for all elements. The matrix circuit equation describing the evolution of currents in circuit elements, including the plasma itself, can then be written as follows:

$$\frac{d}{dt}\left(\vec{\vec{L}}\,\vec{I}\right) + \vec{\vec{R}}\,\vec{I} = \vec{V}\,, \qquad (4.5.-14)$$

where $\vec{I}$ and $\vec{V}$ are the column vectors representing the currents and voltages, respectively, and $\vec{\vec{R}}$ is the diagonal matrix of resistances. For a given time history of voltages and switching sequences, the above matrix equation can be solved to obtain the currents, and then, magnetic fields and power flow through the circuits. In principle, the accuracy of such a procedure should be improved by increasing the number of the equivalent eddy current circuit elements, which, in turn, increases the complexity of the overall circuit analysis as well as the computation time.

The starting point of this procedure is the division of the conducting material into equivalent eddy-current circuit elements. Such a division, however, requires a priori knowledge of eddy-current paths and distributions. As an example, consider a conducting material that contains resistive breaks. These resistive breaks are usually introduced to suppress the magnitude of the eddy currents and associated effects. One can model these resistive breaks as high resistance conductors, as insulators, or a combination thereof. In the "conductor" model, the eddy currents flow through the breaks. The only effect of the resistive break is to increase the resistance of the eddy-current circuit element substantially. In the other extreme of the "insulator" model, the eddy currents do not flow through the breaks but instead turn around and form a "saddle" loop. The most reasonable model of course, is to combine both current paths: a part of the eddy-current flow through and the rest turns around the resistive break. These three models are schematically shown in Fig. 4.5.-13.

A comparison study of these models has been made by Brown, et al. [64], in which the effects of the eddy currents induced in the vacuum vessel of TFTR on the poloidal-field penetration were studied. Four different models for eddy-current circuit elements were used. In each case, the external PF circuits were oscillated in the absence of the plasma, and the resultant vertical field inside the vacuum vessel was calculated and compared to experimental measurements. As expected, the best simulation result was found for the most sophisticated model that properly included both the inductive and resistive contributions of the saddle current and break-paths. Also, satisfactory agreement was obtained with the simplest model, namely, the "conductor" model for the resistive breaks, without taking into account saddle currents. However, the other two simulations with simplified saddle current models did not produce satisfactory results. This work underscores the importance of the insight and a priori knowledge of eddy-current paths and distribution for the analysis.

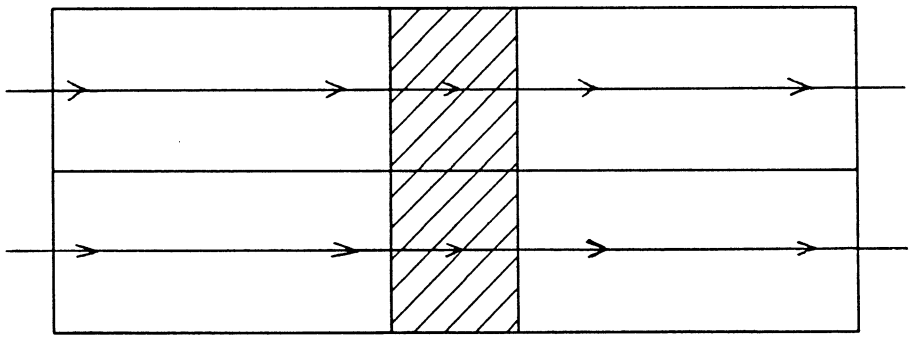

(a) TOROIDALLY CONTINUOUS PATH

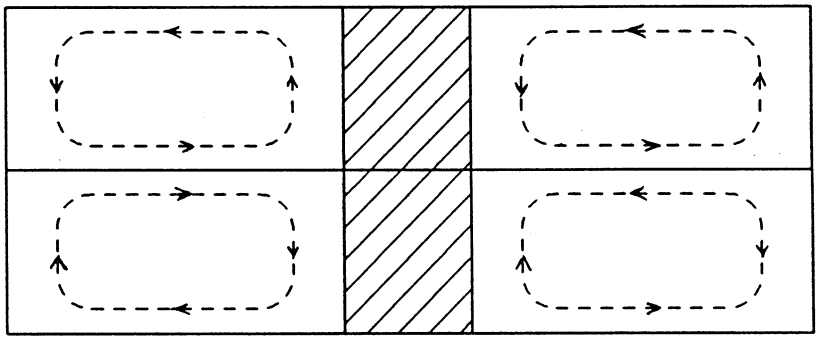

(b) SADDLE CURRENT

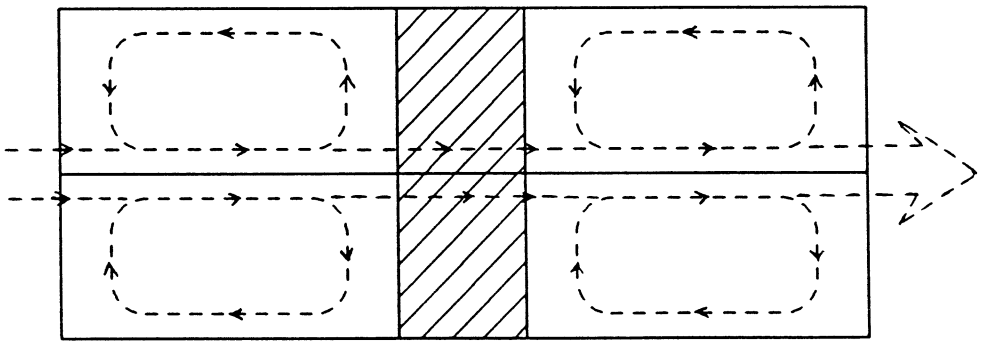

(c) COMBINED

Fig. 4.5.-13. Three models of a resistive break, conductor model (a), the resistive model (b), and combination (c). The resistive breaks are the shaded regions and arrows indicate the eddy-current paths.

To study the impact of eddy currents on the plasma response of the TITAN reactor, a circuit-analysis code has been developed. Given a specified FPC geometry and external coil sets, this code divides the FPC into small sectors and models each as an eddy-current circuit element. The self and mutual inductances of the various circuit elements are then calculated, and the overall inductance matrix is constructed. For a given voltage time history or start-up sequence (e.g., given in Fig. 4.5.-1), the circuit solver computes the time-varying currents in each circuit element. Special attention is given to the equilibrium-field-coil (EFC) circuits. At all times, the current in the EF coils should provide the necessary vertical field to maintain the plasma equilibrium. The required vertical field at the magnetic axis is given by the Shafranov formula [8],

$$B_V = \frac{\mu_0 I_\phi}{4\pi R_T}\left[\ln\left(\frac{8R_T}{r_p}\right) + \beta_\theta + \frac{l_i}{2} - 1.5\right] . \qquad (4.5.-15)$$

It has been shown [65] that the Shafranov formula is an accurate measure of the required vertical field for an RFP over a wide range of plasma conditions. In the presence of conducting material, the vertical field produced by the EFC set together with contributions from other external coils and eddy-currents should be equal to the vertical field given by Shafranov formula (4.5.-15). The code computes these contributions to find the current in the EF coil set self-consistently, and then calculates the necessary voltage, power, and switching sequence that has to be applied to the EFC set.

At present, the circuit analysis code uses the "conductor" model for resistive breaks. An upgrade that takes the saddle currents into account is under development. Furthermore, the plasma relaxation via the RFP dynamo couples the poloidal and toroidal-field circuits. Inclusion of this coupling and simulation of OFCD circuitry are also under study. Application of this code to the TITAN reactor start-up and transients is guiding the coil design, FPC engineering analyses, and FPC design integration effort.

## 4.6. CURRENT DRIVE

At full plasma current the nominal 18 $MW/m^2$ baseline TITAN design supports $W_M \simeq 2$ GJ of stored magnetic energy and requires $L_p I_\phi \simeq 250$ Wb. Given that

these burn conditions can be achieved by the start-up procedures described in Sec. 4.5, an inductively pulsed burn would be sustained for only $L_p/R_p \simeq 200$-$400$ s. Considerations of total power balance, thermal cyclic fatigue in a high-power-density environment, as well as the costs of on-site energy storage (frequent grid start-up seems unlikely) and thermal storage force serious consideration of steady-state current drive. An inductively driven RFP reactor, although a possibility [55], would be re-optimized to minimize the plasma resistance, thereby resulting in larger plasmas, lower power density and possibly the use of superconducting coils.

Section 4.6.1 reviews a number of current-drive options for the RFP. The TITAN study has focused on the Oscillating-Field Current Drive (OFCD) system which is described from an MHD viewpoint in Sec. 4.6.1.1. An analogue circuit model for OFCD is used in Sec. 4.6.2 to investigate parametrically the characteristics of the OFCD system for the TITAN reactor, and a design point is suggested for further engineering analyses.

## 4.6.1. Options

### 4.6.1.1. Oscillating-Field Current Drive (OFCD)

Unlike the tokamak, the toroidal and poloidal currents in the RFP are closely coupled since the RFP plasma is in a minimum-energy state. This near-minimum-energy state is defined [2,3,67] primarily by holding the toroidal flux, $\Phi$, and the magnetic helicity, $K = \int \vec{A}\cdot\vec{B}\, dV$, invariant within a conducting wall surrounding the plasma, where $\vec{A}$ is the magnetic vector potential ($\vec{B} = \vec{\nabla}\times\vec{A}$) and the integration is performed over the volume enclosed by the conducting wall. The locus of these near-minimum-energy states form a curve in F-$\Theta$ space, shown in Fig. 4.6.-1. If an external circuit parameter (e.g., voltage applied to TFC, $V_\Theta$) is varied to change the toroidal flux external to the plasma, intrinsic plasma processes related to turbulence and/or resistive instabilities generate voltages and currents within the plasma and increase or reduce poloidal flux in order to maintain the helicity constant and the plasma in a near-minimum-energy state. This nonlinear coupling between plasma and magnetic fields through the F-$\Theta$ diagram, like that shown on Fig. 4.6.-1, can be used to "rectify" current oscillations created at external coils into a net steady-state current within the plasma [5,46,66]. This "F-$\Theta$ pumping" is envisaged to transform toroidal magnetic flux (poloidal currents) into toroidal currents (poloidal magnetic flux) through the plasma relaxation which maintains the near-minimum-energy

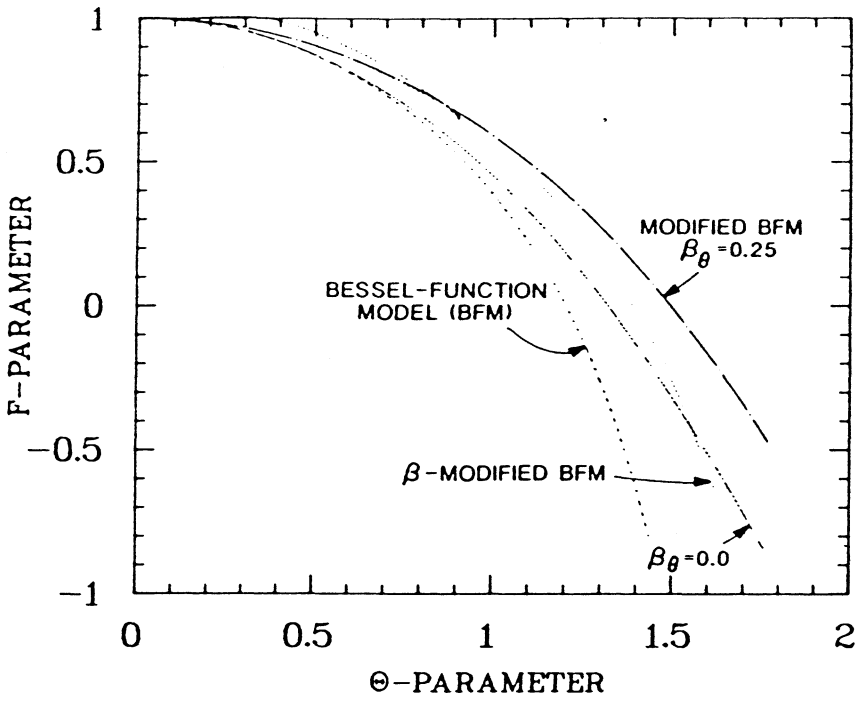


Fig. 4.6.-1. Taylor diagram showing locus of near-minimum-energy RFP states for a range of μ profiles and poloidal beta values.

configuration. The result is an efficient inductive but oscillatory (i.e., with no loss of electromagnetic flux) mean of steady-state current drive for RFPs [5,53,66].

Most of the analysis and design for the OFCD system is based on circuit-analogue models [5,46,66]. Such a model is described in Sec. 4.6.2 and is used to analyze the TITAN reactor current-drive system. One can also explain OFCD in RFPs on the basis of MHD theory. Consider the evolution of the q-profile for one OFCD cycle, as is shown in Fig. 4.6.-2. Initially the near-minimum-energy RFP state is characterized by a q-value that is less than unity on axis, with q falling to zero near the plasma edge and reversing sign at the plasma surface. In order to implement OFCD in the RFP, the external toroidal and poloidal field circuits are oscillated about steady-state values, with the most efficient pumping (i.e., maximum current for minimum reactive power) occurring when the toroidal and poloidal voltages are ninety degrees out of phase (Sec. 4.6.-2). A decrease in the external poloidal flux, Ψ, and an increase in the amplitude of

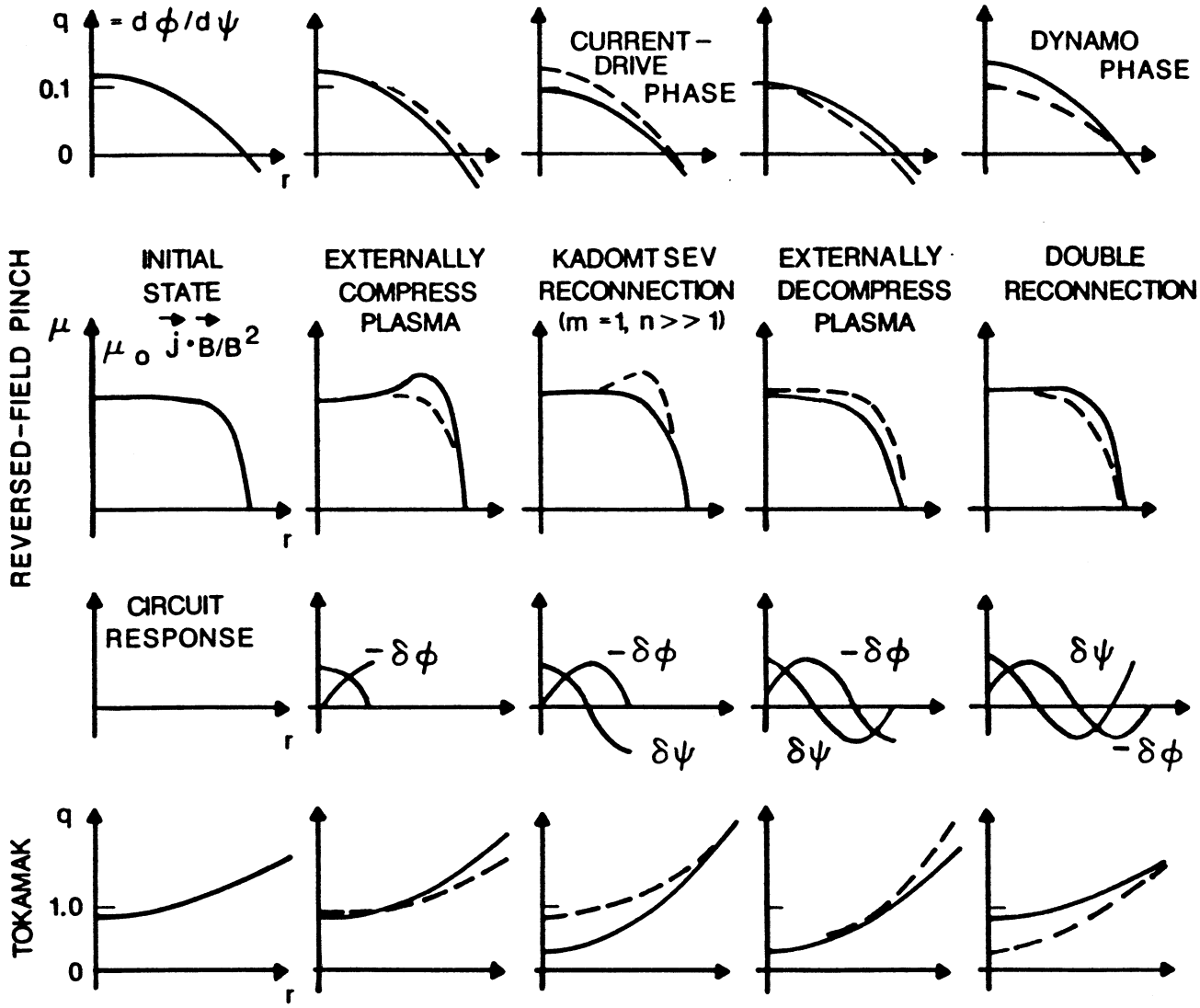


Fig. 4.6.-2. Schematic representation of OFCD for RFPs and tokamaks in terms of a q-profile evaluation.

the external toroidal flux, $\Phi$, will result in more negative F values (i.e., deeper reversal); this deeper reversal appears as a compression phase in Fig. 4.6.-2. The plasma under these conditions is unstable to a series of resistive MHD modes with a poloidal mode number m = 1 and high toroidal mode numbers, n. These instabilities drive a magnetic reconnection process, sometimes referred to as Kadomtsev reconnection, in a flattening of the central portion of the q profile and increasing the poloidal flux [69,70]. The magnetic reconnection process may also occur during the compression phase, and need not be a distinct phase, as is shown in Fig. 4.6.-2. The plasma is then decompressed as the external circuits approach the end of a period; the external poloidal flux is increasing, and the toroidal flux is decreasing at this point in the OFCD cycle. With the value of q at the plasma edge reset to the initial value, the plasma then relaxes by means of a double reconnection [70] (i.e., dynamo effect) into the initial near-minimum-energy state.

An analogous series of q profiles is shown for comparative purposes in Fig. 4.6.-2 for a tokamak. The major difference between the RFP and the tokamak is the process whereby poloidal flux is created on axis; Kadomtsev magnetic reconnection creates poloidal flux in an RFP, whereas it destroys poloidal flux in a tokamak. An as yet unspecified process, therefore, is required to create poloidal flux on axis in a tokamak. The application of OFCD to tokamaks, therefore, requires the identification of a flux-generating process. A scheme for increasing poloidal flux on axis has been proposed [71]. This scheme requires tailored ECRH heating to create an off-axis current channel; a non-monotonic q profile results. The Kadomtsev reconnection process (m = 1, n = 1) will return a monotonic q profile.

4.6.1.2. Bootstrap Current (BC)

Neoclassical theory predicts the existence of a "bootstrap current" caused by radial diffusion. An expression for this bootstrap current density is given by [72]

$$j_{BC} = - \frac{\varepsilon^{1/2}}{B_\theta} \left( \frac{\partial p}{\partial r} \right) , \qquad (4.6.-1)$$

where $\varepsilon \equiv r_p/R_T$ is the inverse aspect ratio. The high $\beta$ that characterizes the RFP suggests a large bootstrap current, but the high aspect ratio will tend to

reduce the effect. As an example, the following approximation to the RFP design-point equilibrium is assumed: $p(r)/p_o \simeq 1 - (r/r_p)^2$ with $p_o \simeq 6$ MPa, $B_\theta \simeq \mu_o I_\phi/2\pi r = \mu_o j_\phi r/2 \simeq 5.9$ T, and $\varepsilon^{1/2} \simeq 0.4$ . For these conditions, Eq. 4.6.-1 results in a bootstrap current density of $j_{BC} \simeq 1.4$ MA/m$^2$ or a total of $\pi r_p^2 j_{BC} = 1.6$ MA of toroidal current ($\pi r_p^2 = 1.13$ m$^2$) as compared to the required $I_\phi \simeq 18$ MA for the design point. Significantly steeper pressure gradients and lower aspect ratios would be required to make the bootstrap current a significant contributor, if it exists at all. Bootstrap current is not treated as a serious possibility for TITAN.

4.6.1.3. Alfvén-Wave (AW) Current Drive

Of all the proposed forms of RF current drive, the compressional Alfvén wave is by far the most efficient, out-performing the LH wave by about a factor of two on an ampere per watt basis. For Alfvén-wave current drive, Ehst [73] gives

$$P_{RF}^{AW} = 8.9\times10^{-20} \frac{I_\phi R_T n}{T} , \qquad (4.6.-2)$$

whereas Fisch and Karney [74] give

$$P_{RF}^{AW} = 1.5\times10^{-20} \frac{I_\phi R_T n}{T \beta^{1/2}} , \qquad (4.6.-3)$$

where $\beta$ is the local beta value and T is in units of keV. Both Eqs. (4.6.-2) and (4.6.-3) are based on consideration of waves with $k_\parallel > k_\perp$. For a special Alfvén wave in which $k_\perp >> k_\parallel$ (a condition which can easily be accomplished in tokamaks) a detailed calculation by Li [75] gives

$$P_{RF}^{AW} = 7.5\times10^{-20} \frac{I_\phi R_T n}{T} . \qquad (4.6.-4)$$

For the $I_\phi \simeq 18$ MA TITAN reactor design, these three relations respectively

result in 137, 73, and 115 MW of RF power required for the steady-state current drive system.

The main problems with the Alfvén-wave current drive revolve around trapped-particle effects in toroidal geometry and possible resonance with and damping of the wave by fast alpha particles. In principle, particles with speeds comparable to the Alfvén velocity, $v_A$, resonate with the wave and drain energy from it. The desirable condition is for the fast electrons to resonate with the wave and absorb all of the wave momentum since these electrons are not very collisional. However, in a typical RFP reactor $v_A \simeq 2v_\alpha(300\ \text{keV})$ and $v_A \simeq v_\alpha(1.2\ \text{MeV})$, where $v_\alpha(E_\alpha)$ is the velocity of an alpha-particle with energy $E_\alpha$; a part of the alpha-particle distribution, therefore, will resonate with the wave. Most of the wave energy and momentum absorbed by the alpha particles will, in turn, be passed onto the bulk electron population which is highly collisional and produces less current as compared to the case where all of the wave momentum is absorbed by the fast electrons in the first place. The net impact of the alpha particles is, therefore, to decrease the Alfvén-Wave current-drive efficiency.

Trapped-particle effects in toroidal geometry present a much more serious problem for low-aspect-ratio systems. Generally, the Alfvén waves have low phase velocity and, therefore, interact most strongly with electrons precessing slowly around the torus (these electrons have $v_\perp >> v_\parallel$). Such particles are precisely those which are most susceptible to trapping in banana orbits. Fisch and Karney advance [74] arguments that the trapped-particle effects would not impair the Alfvén wave drive. Ultimately, however, this question would have to be resolved by experiment. The trapped-particle effects are expected to be especially strong in systems like the ATR/ST [76], but are ignorable in high aspect ratio stellarators (aspect ratio, A = 14) and should also be ignorable in a typical RFP reactor (A ≃ 6-8).

#### 4.6.1.4. Lower-Hybrid (LH) Current Drive

The LH wave has been proven experimentally to be an effective means of current drive in tokamaks, and, in fact, has been used in PLT [70] to start the tokamak without the use of OHCs. Lower-hybrid drive experiences no problem with resonating alpha particles or trapped-particle effects, but it does have a density limit set by $\omega_{ce} > \omega_{pe}$. This condition can be expressed as $\beta < 0.008\ T(\text{keV})$, where $\beta$ is the local value, and is marginally satisfied by the TITAN baseline design. Lower-hybrid current drive, therefore, should be possible,

provided care is taken in the detailed design of the system. Lower-hybrid waves can be easily launched from waveguides and have been launched with intensities up to 150 $MW/m^2$. The main problem with LH drive is that of efficiency. Peng [78] gives the following expression for the drive power:

$$P_{RF}^{LH} = 13.5\times10^{-20} \frac{I_\phi R_T n}{T} , \qquad (4.6.-5)$$

where T is again in units of keV, while Fisch and Karney give [74]

$$P_{RF}^{LH} = 0.93\times10^{-20} I_\phi R_T n . \qquad (4.6.-6)$$

The results of applying these relationships to the $I_\phi$ = 18 MA baseline design give $P_{RF}^{LH}$ = 207 and 286 MW, respectively. It can be seen that the LH wave is less efficient than the Alfvén wave as applied to the RFP.

4.6.1.5. Relativistic Electron Beams (REB)

Reference 79 presents detailed analysis and design for a REB current-drive system for the FED-A fusion device. Those calculations indicate that the current-drive power for such a system can be taken approximately as

$$P^{REB} = 2I_\phi^2 R_p , \qquad (4.6.-7)$$

where $R_p$ is the plasma resistance. Applying Eq. (4.6.-7) to the TITAN reactor with $I_\phi \simeq$ 18 MA results in a current drive system with 16 MW of REB power, consistent with a 1.6-MJ pulse energy and an interpulse period of 0.1 s. The REB current drive has been demonstrated experimentally on several tokamaks and has been used successfully for start-up without the use of OH coils [80].

Although the low-power requirement makes REBs attractive, a number of obstacles to implementation can be identified. Firstly, the REB current-drive system involves the repeated firing of megavolt capacitor banks, giving rise to questions of reliability when applied to a commercial reactor. Secondly, theory indicates that the REB current will only penetrate a few centimeters into the plasma, leading to a hollow current profile. Deeper penetrations can be

achieved if very high voltages (~ 50 MV) can be used. A combination of REB to provide current in the outer plasma with Alfvén-Wave drive to provide current at the plasma core may offer some power savings, albeit at the cost of additional complexity. One hope in dealing with the hollow current profile is that the REB-created currents will diffuse rapidly into the plasma core through anomalous processes or be transported into the central plasma through MHD activities.

### 4.6.2. OFCD Plasma/Circuit Modeling

Of the current drive options summarized in Sec. 4.6.1, the OFCD system was chosen for further evaluation. This choice was based on the projected efficiency of the drive, its relative simplicity, and the uniqueness of this scheme to the RFP. A plasma/circuit model for OFCD was then used to identify and assess the potential design, power engineering, and magnetics problems. This section summarizes this effort.

#### 4.6.2.1. Model

Little analysis and design beyond that described in Ref. 53 are available to describe OFCD systems for either RFP experiments or reactors. This section develops and applies a methodology by which future engineering evaluations of OFCD can proceed. In developing and evaluating a global picture of OFCD, the circuit parameters, definitions, and approach summarized in Table 4.6.-I are used to arrive at an OFCD equation. Note that the brackets (<>) throughout this section denote time-averaged quantities with the exception of the magnetic fields, with $\langle B_\phi \rangle$ being a spatial average and $\bar{B}_\phi$ being a time average.

In order to implement OFCD in the RFP, the external toroidal and poloidal-field circuits are oscillated about steady state values . The plasma is described in terms of K, $\Phi$, and $W_M$, and the relationship between these parameters and the circuit variables (i.e., resistances, inductances, currents, voltages) constitutes the overall current-drive model. The time dependence of K, $\Phi$, and $W_M$ results directly from the Maxwell equations:

$$\frac{dK}{dt} = 2\Phi V_\phi - 2 \int \eta \vec{j}\cdot\vec{B}\, dV \,, \qquad (4.6.-8)$$

$$\frac{d\Phi}{dt} = + V_\Theta \,, \qquad (4.6.-9)$$

TABLE 4.6.-I

SUMMARY OF DEFINITIONS AND NOTATION USED TO MODEL OSCILLATING-FIELD CURRENT DRIVE (OFCD)

| Definition | Parameter |
|---|---|
| Toroidal voltage on plasma | $V_\phi$ |
| Toroidal current in plasma | $I_\phi$ |
| Poloidal voltage applied to toroidal-field coil | $V_\theta = \partial\Phi/\partial t \equiv \dot{\Phi}$ |
| Poloidal current flowing in external conductor | $I_\theta$ |
| Plasma resistance | $R_p$ |
| Magnetic helicity | $K = \frac{1}{\mu_o} \int \vec{A}.\vec{B} \; dV$ |
| Toroidal flux | $\Phi = 2\pi \int_0^{r_w} B_\phi(r)\, r\, dr$ |
| Total field energy within conducting shell | $W_M = \int (B^2/2\mu_o)\, dV$ |
| Vacuum toroidal inductance | $L_o = \mu_o r_p^2/2R_T$ |
| Inverse aspect ratio | $\varepsilon = r_w/R_T$ |
| Average toroidal field within shell | $\langle B_\phi \rangle = \Phi/\pi r_w^2$ |
| Reversal parameter | $F = \bar{B}_\phi(r_w)/\langle B_\phi \rangle = L_o I_\theta/\Phi$ |
| Pinch parameter | $\Theta = \bar{B}_\theta(r_w)/\langle B_\phi \rangle = L_o I_\phi/\varepsilon\Phi$ |

$$\frac{dW_M}{dt} = I_\phi V_\phi - I_\theta V_\theta - \int \eta \vec{j}\cdot\vec{j} \; dV \; , \qquad (4.6.\text{-}10)$$

$$\vec{E} = \eta\vec{j} - \vec{v}\times\vec{B} \quad (E_\phi = \eta j_\phi - \alpha B_\phi) \; , \qquad (4.6.\text{-}11)$$

where a positive Faraday's Law convention for the toroidal circuit is used in Eq. (4.6.-9); this convention orients $\Phi$ in the same direction as $I_\phi$. The last expression (4.6.-11) gives an Ohm's law corrected for the plasma dynamo effect. Defining the plasma energy and "helicity" resistances, $R_p$ and $R_p'$, respectively, by

$$R_p \equiv \frac{1}{I_\phi^2} \int \eta \, \vec{j}\cdot\vec{j} \, dV \ , \qquad (4.6.-12a)$$

$$R_p' \equiv f_A \, R_p \equiv \frac{1}{\Phi \, I_\phi} \int \eta \, \vec{j}\cdot\vec{B} \, dV \ , \qquad (4.6.-12b)$$

the plasma helicity and energy equations become

$$\frac{dK}{dt} = 2\Phi(V_\phi - I_\phi f_A R_p) \ , \qquad (4.6.-13)$$

$$\frac{dW_M}{dt} = I_\phi V_\phi - I_\Theta V_\Theta - I_\phi^2 R \ . \qquad (4.6.-14)$$

The factor $f_A \equiv R_p'/R_p \equiv (2\Theta/r_p R_p) \int (\eta/\mu) \, \vec{j}\cdot\vec{j} \, dV$ is the ratio of energy resistivity to "helicity" resistivity and $f_A = 1$ for the Bessel-function model (i.e., for the special case of $\beta = 0$ and $\mu(r) \equiv \mu_o \vec{j}\cdot\vec{B}/B^2$ equal to a constant). It is readily seen from either Eq. (4.6.-8) or (4.6.-13) that if the time-averaged $\langle dK/dt \rangle$ is to equal zero during an OFCD oscillation period, the dissipation term (the power to be supplied to the plasma to maintain the plasma current) must be equal to the time-averaged $2\langle \Phi V_\phi \rangle$. Thus, $\Phi$ and $V_\phi$ should be nominally in phase; or, $V_\phi$ and $V_\Theta \simeq \dot{\Phi}$ should be out of phase by $90^\circ$.

The plasma magnetic energy, $W_M$, can be written in terms of plasma and circuit parameters as

$$W_M = \frac{1}{2} L_p \, I_\phi^2 + \frac{\Phi^2}{2L_o} \ . \qquad (4.6.-15)$$

The plasma inductance, $L_p$, is a function of the field profiles and, for example, can be derived using the BFM (i.e., $\mu(r)$ = constant). Combining Eqs. (4.6.-9), (4.6.-14), and (4.6.-15) leads to the following expression for the toroidal voltage around the plasma, $V_\phi$:

$$V_\phi = I_\phi R_p + \left(L_p + \frac{\Theta}{2}\frac{dL_p}{d\Theta}\right)\dot{I}_\phi + \left(\frac{1 - F}{\varepsilon\Theta} - \frac{\varepsilon\Theta^2}{2L_o}\frac{dL_p}{d\Theta}\right) V_\Theta \ . \qquad (4.6.-16)$$

Equation (4.6.-16) shows that if a) the coupling of fields is sufficiently strong to make $L_p$ a function of $\Theta$, and b) if a mechanism exists to allow the plasma near-minimum-energy state to relax to some point in F-$\Theta$ space (Fig. 4.6.-1) on a time scale, $\tau_R$, then oscillations of $V_\phi$ and $V_\Theta$ in proper phase at a frequency less than $\sim 2\pi/\tau_R$ can give a net time-averaged current, $\langle I_\phi \rangle$, with $\langle V_\phi \rangle = 0$ (i.e., no net flux change).

The OFCD equation (4.6.-16) can be used to determine the flux changes, field oscillations, and power flows associated with OFCD as applied to the RFP. In order to solve Eq. (4.6.-16), the plasma inductance, $L_p$, its derivative with respect to the pinch parameter, $dL_p/d\Theta$, and the plasma resistance, $R_p$, must be known. These quantities depend on the field profiles and the relationship between F and $\Theta$. The plasma resistance, $R_p$, used in Eq. (4.6.-16) is a function of the field profiles through the factor $g_{OHM}$ as:

$$R_p = 2\, g_{OHM} \frac{\eta}{\varepsilon^2 R_T} \ , \qquad (4.6.-17)$$

where $\eta$ is the classical resistivity evaluated at the average plasma temperature. The profile factor, $g_{OHM}$, is often referred to as the resistance "anomaly" factor, a name that can be misleading in that as given above $g_{OHM}$ for $Z_{eff} = 1$ is a measure of the extended current path resulting from the "screwing-up" of the high-pitch field lines.

The special case of the BFM is amenable to analytic solution and is reproduced here. Using the BFM field profiles [i.e., $B_\Theta(r) \propto J_1(\mu r)$ and $B_\phi(r) \propto J_0(\mu r)$] and equating the total magnetic energy stored within the plasma to $L_p I_\phi^2/2$ gives the following expression for $L_p$:

$$L_p = \frac{2L_o}{\varepsilon^2}\left[1 + \frac{(2F + 1)(F - 1)}{2\Theta^2}\right] \ , \qquad (4.6.-18)$$

where $F = \Theta J_0(2\Theta)/J_1(2\Theta)$ for the BFM; included in Eq. (4.6.-15), and hence, in Eq. (4.6.-18), is the energy needed to compress an initially uniform toroidal flux into the $B_\phi(r) \propto J_0(\mu r)$ distribution. The purely poloidal inductance for the BFM is

$$L_{p\Theta} = \frac{2W_{B\Theta}}{I_\phi^2} = \frac{L_o}{\varepsilon^2}\left[1 + \frac{F}{\Theta^2}(F - 1)\right] . \qquad (4.6.-19)$$

For the BFM and a flat temperature distribution, $g_{OHM}$ is given by

$$g_{OHM} = 2(\Theta^2 + F^2) - F . \qquad (4.6.-20)$$

For the BFM model without deep reversal ($\Theta < 1.6$), $g_{OHM}$ typically is ~ 3.

For more realistic models of the $\mu$ profile (e.g., modified-Bessel-function model), the field profiles should generally be calculated numerically. An example is a preliminary model described in Appendix A of Ref. 53. The MHD pressure balance, $\vec{j}\times\vec{B} = \nabla p$, can be used to specify the current density parallel and perpendicular to the magnetic field:

$$\vec{j}_{\parallel} = \mu\vec{B} . \qquad (4.6.-21a)$$

$$\vec{j}_{\perp} = \frac{\nabla p \times \vec{B}}{B^2} , \qquad (4.6.-21b)$$

$$\nabla \times \vec{B} = \mu_0 \vec{j} = \mu_0 (\vec{j}_{\parallel} + \vec{j}_{\perp}) , \qquad (4.6.-21c)$$

where $\mu(r) = \mu_0 \vec{j}.\vec{B}/B^2$ and the last equation is the Ampere's Law. For given $\mu$ and pressure profiles, Eqs. (4.6.-21) can be solved to find the magnetic field and current density profiles. For one-dimensional axisymmetric system, these equations can be expressed in cylindrical co-ordinates as:

$$-\frac{\partial B_\phi}{\partial r} = \mu_o j_\Theta = \mu B_\Theta + \mu_o \frac{\partial p}{\partial r}\frac{B_\phi}{B^2} \qquad (4.6.-22a)$$

$$\frac{1}{r}\frac{\partial}{\partial r}(rB_\Theta) = \mu_o j_\phi = \mu B_\phi - \mu_o \frac{\partial p}{\partial r}\frac{B_\Theta}{B^2} \quad . \tag{4.6.-22b}$$

These equations are solved for field and current-density profiles by specifying T(r), n(r), $\mu$(r) and the following constraints:

$$\beta_\Theta = \frac{\int_0^{r_p} p\ 2\pi r\ dr}{\pi\ r_p^2\ B_\Theta^2(r_p)/2\mu_0} \quad , \tag{4.6.-23a}$$

$$I_\phi = \int_0^{r_p} j_\phi\ 2\pi r\ dr \quad . \tag{4.6.-23b}$$

The resulting profiles then are used to determine $g_{OHM}$, F, $L_p$, and $dL_p/d\Theta$ for use in the OFCD equation (4.6.-16).

The poloidal and toroidal circuit equations coupled through Eq. (4.6.-16) can be solved numerically for $I_\phi$ once driver functions, such as those given below, are selected for $\Phi$ and $V_\phi$.

$$\Phi = \Phi_o + \delta\Phi \cos \omega t \quad , \tag{4.6.-24a}$$

$$V_\Theta = \dot{\Phi} = \delta\Phi\ \omega \sin \omega t \quad , \tag{4.6.-24b}$$

$$V_\phi = \delta V_\phi \cos \omega t \quad . \tag{4.6.-24c}$$

The constraint that the time-averaged helicity is constant ($\langle dK/dt \rangle = 0$) can be used to establish limits on the magnitude of the field oscillations required to sustain a given toroidal plasma current. If the ohmic dissipations for both the induced and driven cases are similar, and if the induced case is characterized by $\Phi_o$ and $V_{\phi o}$, then dK/dt for the driven case is given by Eq. (4.6.-13) with $V_{\phi o} \equiv I_\phi R_p$. Hence,

$$\frac{dK}{dt} \simeq 2\Phi(V_\phi - V_{\phi o}) \quad . \tag{4.6.-25}$$

Using the driver functions given by Eqs. (4.6.-24), the time average of dK/dt for the driven case is

$$- \langle dK/dt \rangle = \delta\Phi\delta V_\phi + 2\Phi_o V_{\phi o} \quad . \tag{4.6.-26}$$

For $\langle dK/dt \rangle \simeq 0$, the following condition on the amplitudes of the toroidal flux and voltage oscillation results:

$$\left(\frac{\delta\Phi}{\Phi_o}\right)\left(\frac{\delta V_\phi}{V_{\phi o}}\right) \simeq - 2 \quad . \tag{4.6.-27}$$

Given that toroidal flux oscillations much above $\delta\Phi/\Phi_o \simeq 0.02\text{-}0.03$ are expected to impact seriously the RFP configuration (i.e., loss of toroidal-field reversal), the AC toroidal voltage needed to drive a DC toroidal current with $\langle dK/dt \rangle \simeq 0$ can be 6-10 times greater than the voltage needed to sustain an inductively driven RFP.

To assess the tradeoff between $\delta\Phi/\Phi_o$, $\delta V_\phi/\langle I_\phi f_A R_p \rangle$, $\omega$, $\delta I_\phi/\langle I_\phi \rangle$, and reactive power, the plasma OFCD equations must be solved in conjunction with a realistic circuit model. In a simplified form, Fig. 4.6.-3 illustrates two independent circuits coupled through the RFP plasma. A circuit representation of the poloidal-field (PF) and toroidal-field (TF) circuits coupled through the OFCD equation (4.6.-16), and the F-$\Theta$ diagram is shown in Fig. 4.6.-4, where the subscript "H" refers to "helicity"-drive, and current elements designated with "L" refer to liner or blanket elements. Figure 4.6.-5 schematically illustrates the oscillating or reactive power flows in terms of a simplified model, with the power $P_\Omega$ being dissipated therein. Of the reactive power or "Poynting" vectors flowing across the plasma surface, $P_p^*$, the quantity $P_L$ is dissipated in the liner surrounding the plasma and the reactive power $P_H^* \ll P_p^*$ actually must be managed by the helicity drive circuits. The remaining reactive power, $\simeq P_p^* - P_H^* - P_L$, is stored in the external plasma inductance, and may be subject to further dissipative loss, depending on a yet-to-be-resolved arrangement of

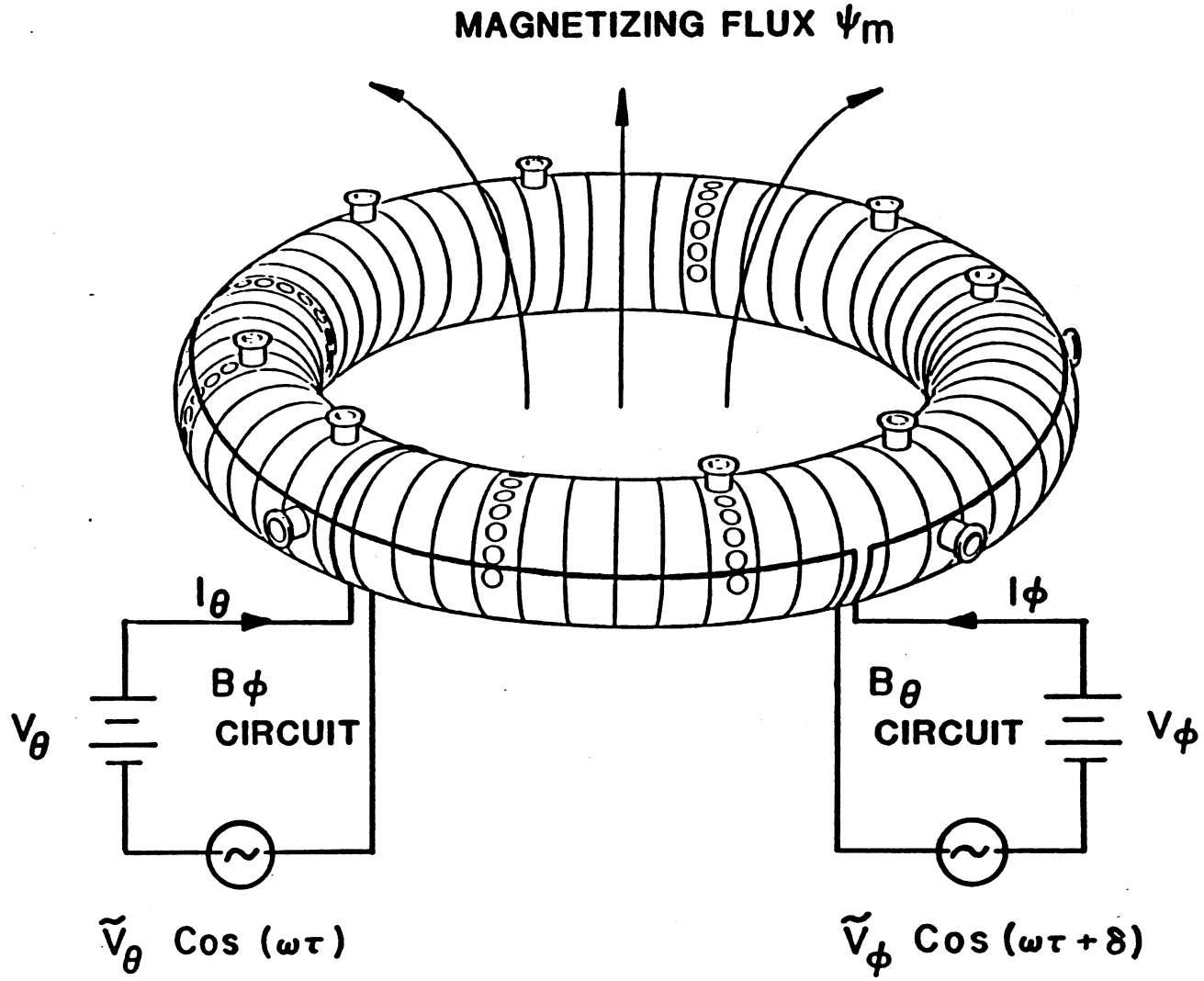


Fig. 4.6.-3. Schematic diagram of OFCD circuits coupled through the RFP plasma.

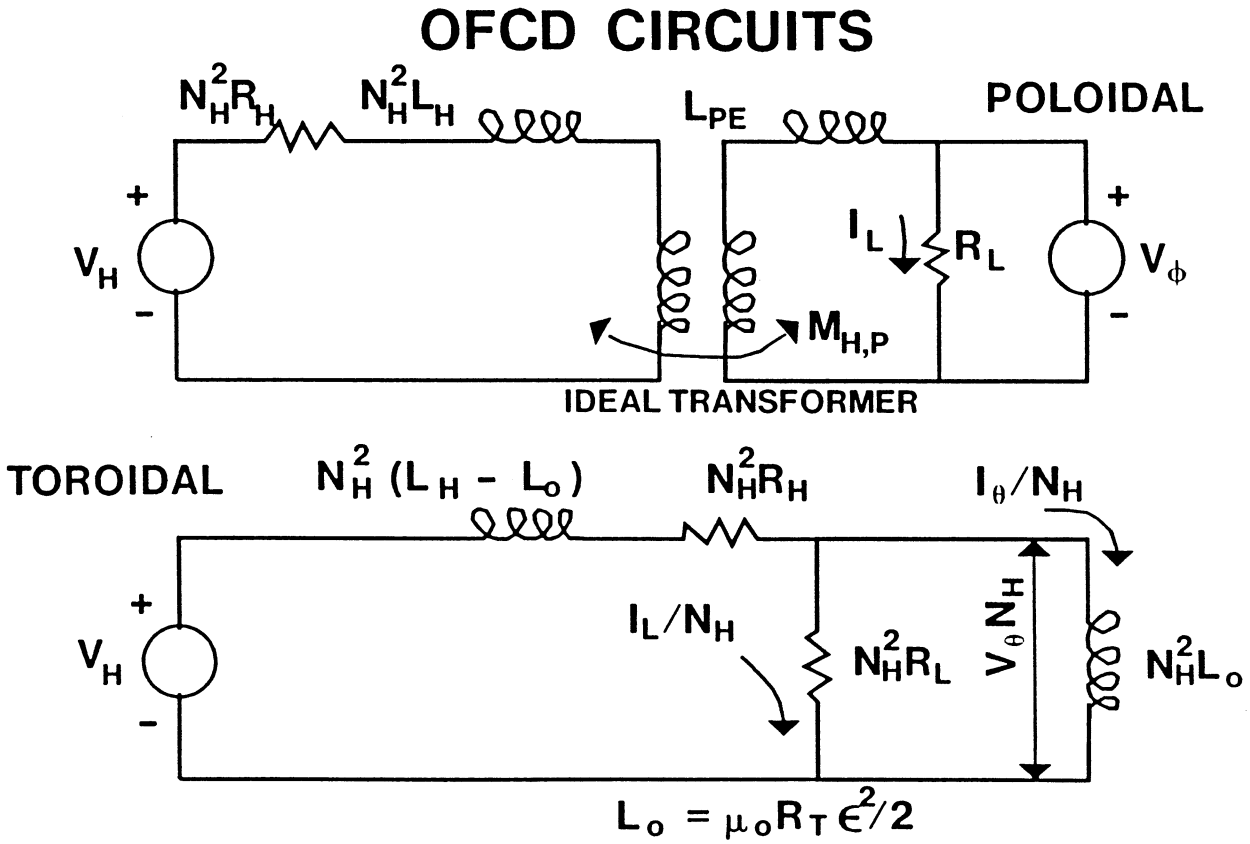


Fig. 4.6.-4. OFCD circuit diagram. The subscript "H" refers to "helicity"-drive, and current elements designated with "L" refer to liner or blanket elements.

conducting paths in the immediate vicinity of the reactor torus. Of the $P_H^*$ reactive power handled by the OFCD circuit, the amount $P_H$ is dissipated therein. Thus, the total real power that must be supplied to sustain the RFP current, $I_\phi$, is $P_H + P_L + P_\Omega$. Figure 4.6.-5 defines a number of plasma and circuit Q-values and current-drive efficiencies.

The calculational algorithm developed to solve simultaneously and parametrically the plasma and circuit OFCD equations is shown schematically in Fig. 4.6.-6. Input parameters include all plasma profiles determined from the solution of the MHD Eqs. (4.6.-21), geometry, F-Θ oscillation point, key plasma parameters, and all helicity-circuit parameters. The highly non-linear set of partial differential equations is solved for $\langle dI_\phi/dt \rangle = 0$ under the following constraints

- $\langle dI_{H\phi}/dt \rangle = 0$ (no net flux in the circuit),
- $\langle dK/dt \rangle = 0$ (constant average helicity),
- Total energy balance,
- $E_\phi \simeq E_\Theta$ around the plasma.

These four conditions give a unique OFCD design point for a given set of input variables about which sensitivity studies have been made, with the constraint that $E_\phi/E_\Theta \simeq 1$ being relaxed somewhat to allow variations in $\delta\Phi/\Phi_o$.

4.6.2.2. Parametric Results

The model shown in Fig. 4.6.-6 has been evaluated through single-point variations of poloidal beta, $\beta_\Theta$, plasma temperature, T, OFCD frequency, $\omega$, toroidal flux swing, $\delta\Phi/\Phi_o$ (i.e., $E_\Theta/E_\phi$), and liner resistance, $R_L = \eta_L(R_T/\delta_T r_w)$. Table 4.6.-II gives the basecase TITAN parameters about which sensitivity studies were made.

A key parameter of interest is the reactive power required to sustain in steady state the parameters listed on Table 4.6.-II. Figure 4.6.-7 shows the dependence of reactive power in both poloidal and toroidal circuits, $P_{H\phi}^*$ and $P_{H\Theta}^*$, respectively, as well as the associated Poynting-vector power flows past the plasma surface, $P_{p\phi}^*$ and $P_{p\Theta}^*$, respectively. As $\beta_\Theta$ is increased, the required plasma current is decreased for a given fusion power and plasma dimension. Typically, $\delta\Phi/\Phi_o \simeq 0.016$, $\delta V_\phi/I_\phi R_p \simeq 460$, and $\delta I_\phi/I_\phi \simeq 0.006$ for this case of a highly resistive liner ($\eta_L \simeq 100$ μΩ m and $\delta = 1$ mm).

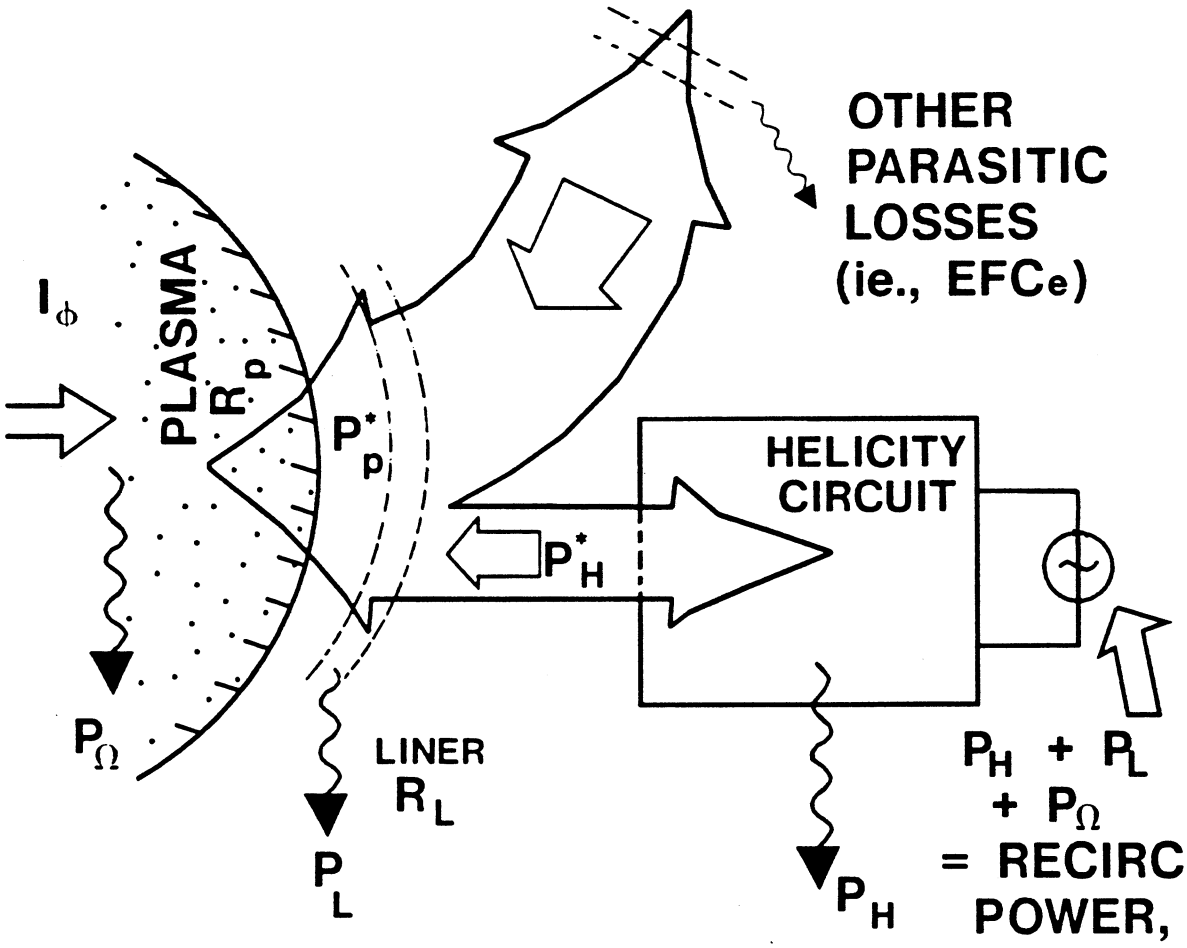


$$Q_p = P^*_p / P_\Omega$$

$$Q_H = P^*_p / (P_L + P_H)$$

$$Q'_H = P^*_H / P_H$$

$$\frac{I_\phi}{P_{CD}}(A/W) = \frac{I_\phi / P_\Omega}{1 + Q_p / Q_H}$$

$$I_\phi / P_{CD} = \frac{I_\phi / P_\Omega}{1 + Q_p / Q_H}$$

Fig. 4.6.-5. OFCD circuit/plasma global power flows.

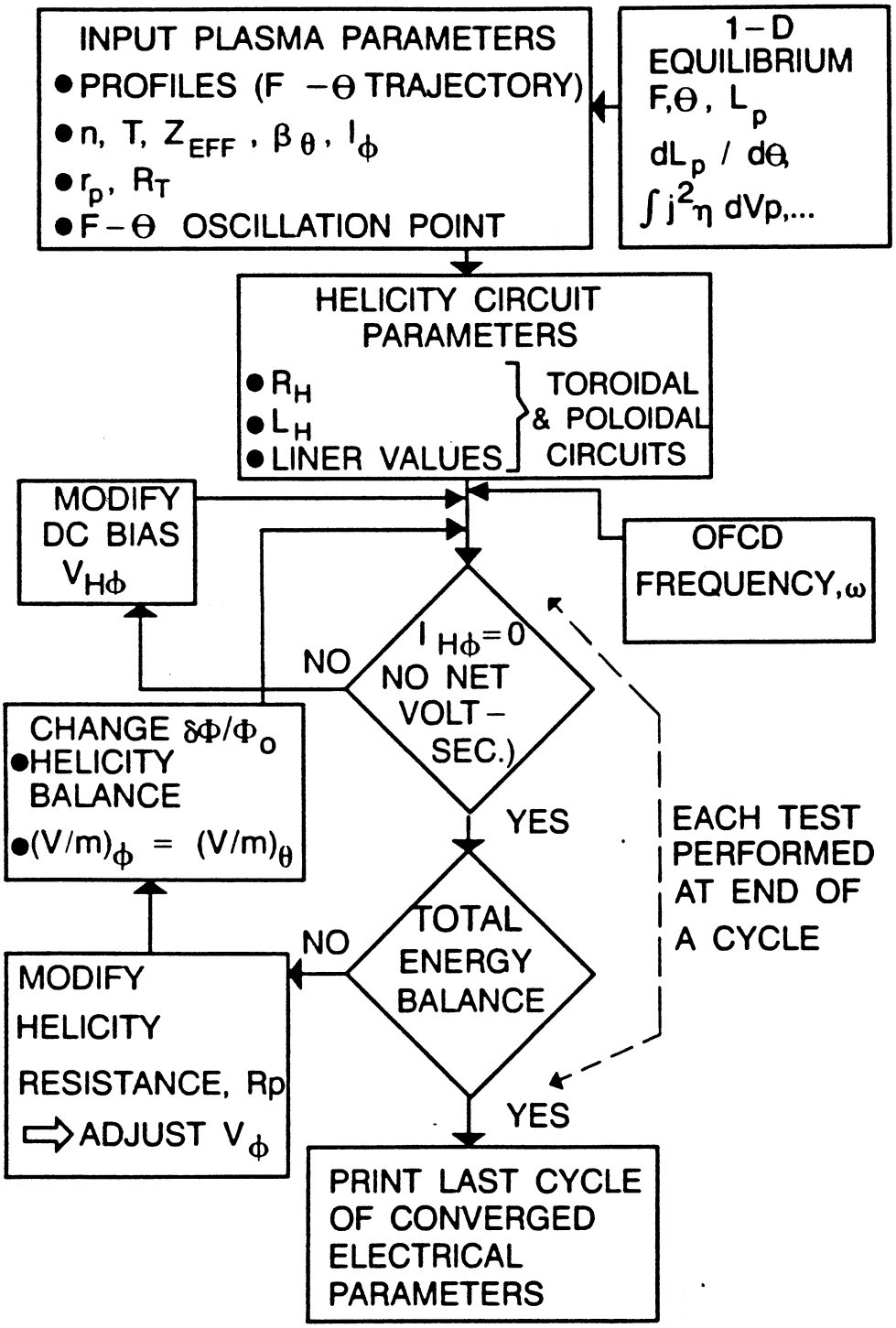


Fig. 4.6.-6. The algorithm used to solve OFCD plasma/circuit equations.

TABLE 4.6.-II

BASECASE TITAN OFCD PARAMETERS

| | |
|---|---|
| Minor radius, $r_p$ (m) | 0.61 |
| Major radius, $R_T$ (m) | 3.96 |
| Current, $I_\phi$ (MA) | 18-22[a] |
| Poloidal beta, $\beta_\theta$ | 0.1-0.2 |
| Density, n ($10^{20}$ $m^{-3}$) | 4.-8. |
| Temperature, T (keV) | 10.-20. |
| Profile exponents, $\nu$ , $f = 1 - (r/r_p)^\nu$ | |
| • $\mu(r)/\mu(0)$ | 8. |
| • $T(r)/T(0)$ | 4. |
| • $n(r)/n(0)$ | 2.5 |
| Shell/liner parameters | |
| • Minor radius, $r_w$ (m) | 0.66 |
| • Thickness, $\delta_L$ (m) | 0.001 |
| • Resistivity, $\eta_L$ ($\Omega$ m) | $10^{-4}$ |
| OFCD Parameters | |
| • Frequency (Hz) | 60 |
| • Flux-swing, $\delta\Phi/\Phi_o$ | 0.016 |
| • $E_\phi/E_\theta \simeq (V_\phi/2\pi R_T)/(V_\theta/2\pi r_p)$ | 1.0 |

(a) Underline value gives basecase.

As the plasma resistance is decreased for higher operating temperature, the required OFCD reactive power decreases, as is shown on Fig. 4.6.-8. The toroidal-flux and plasma current swing are also shown. Figure 4.6.-9 gives the dependence of reactive power, $\delta\Phi/\Phi_o$, and $\delta I_\phi/I_{\phi o}$ on drive frequency, with the plasma energy change per cycle decreasing with increased frequency (less dissipation over a shorter period), giving the relative insensitivity of reactive power to frequency change. The variation of reactive powers and current swing on the toroidal flux swing is shown in Fig. 4.6.-10, where the $\delta\Phi/\Phi_o$ variation was caused by varying $E_\theta/E_\phi$ away from the basecase value of unity. It is seen from the viewpoint of minimizing plasma current variations, plasma reactive power, and (most importantly) the helicity-circuit reactive power ($P^*_{H\phi}$+ $P^*_{H\theta}$), that an optimal value of $\delta\Phi/\Phi_o$ in the range 0.02 - 0.03 is indicated. Also shown on Fig. 4.6.-10 is the region where toroidal-field

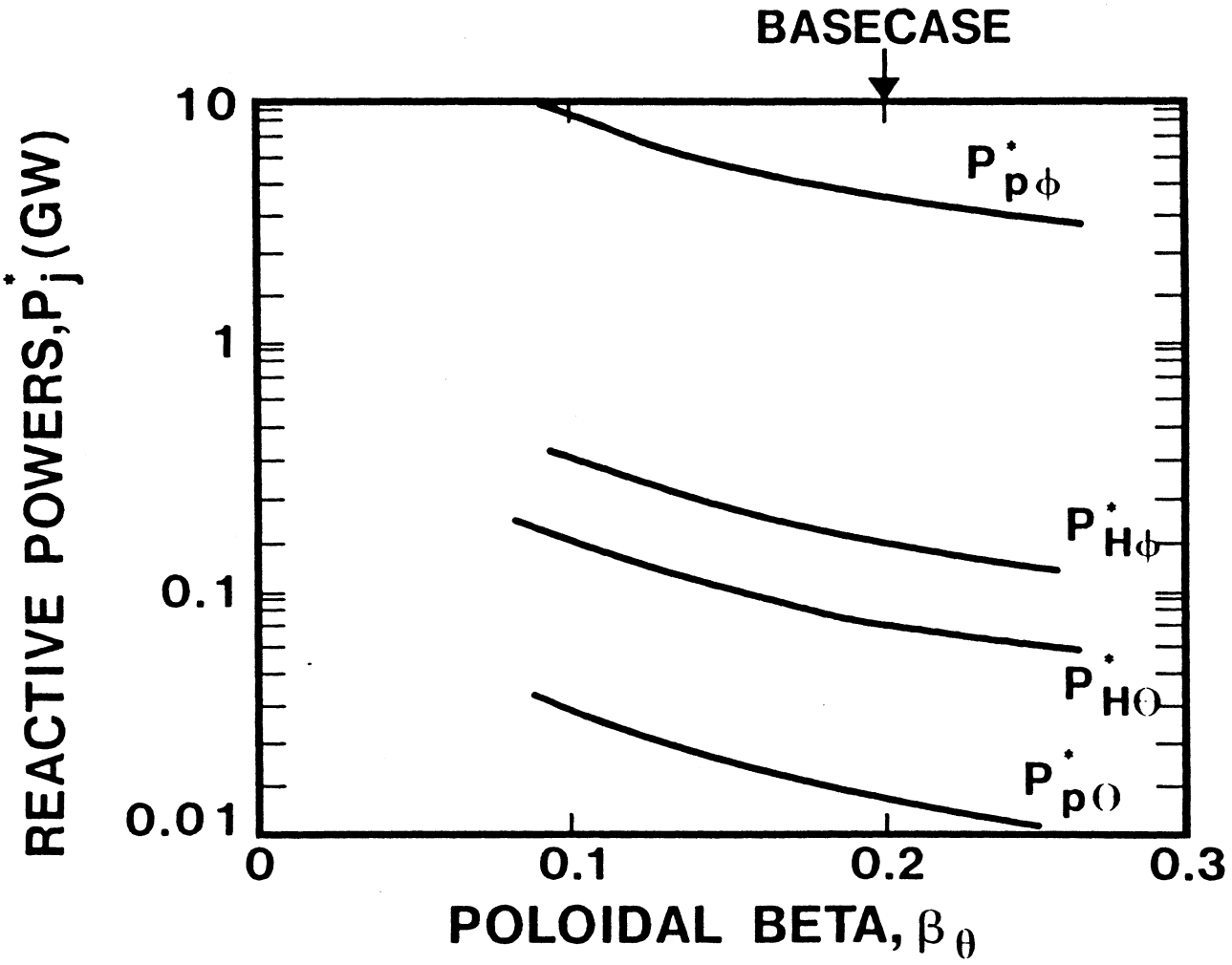


Fig. 4.6.-7. Dependence of OFCD reactive powers on poloidal beta.

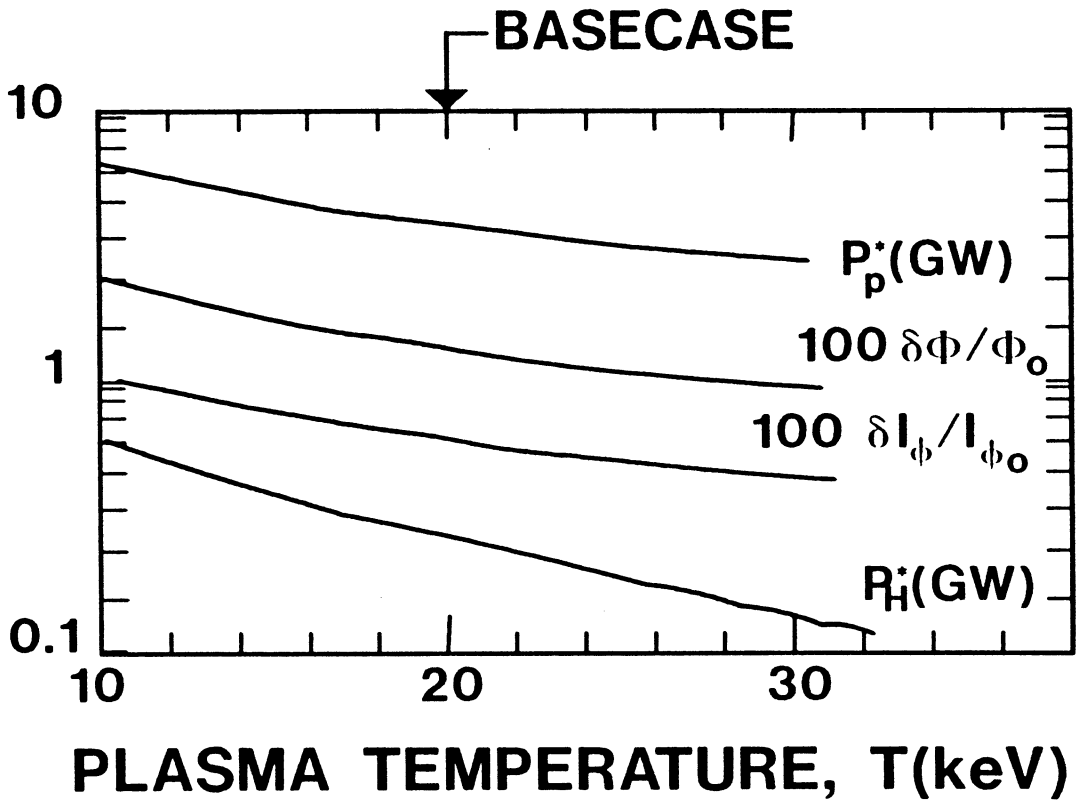


Fig. 4.6.-8. Dependence of OFCD reactive power, toroidal flux change, and plasma current variation on average plasma temperature.

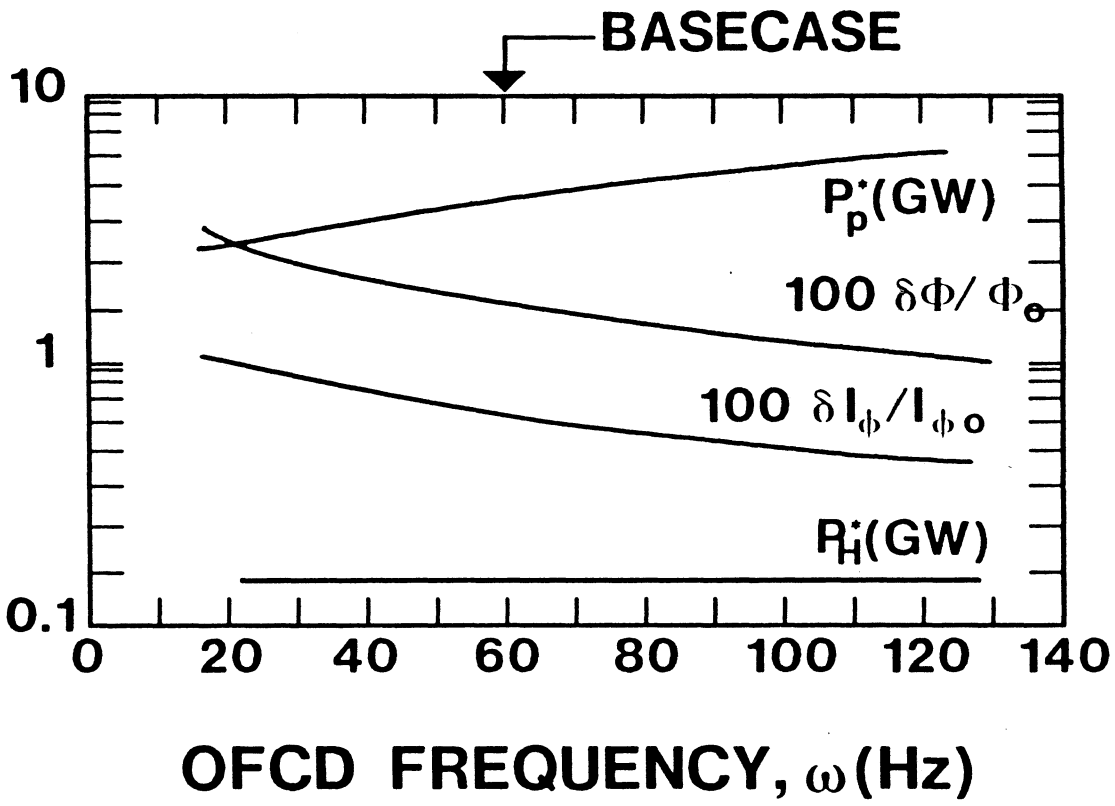


Fig. 4.6.-9. Dependence of OFCD reactive power, toroidal flux change, and plasma current swing on drive frequency.

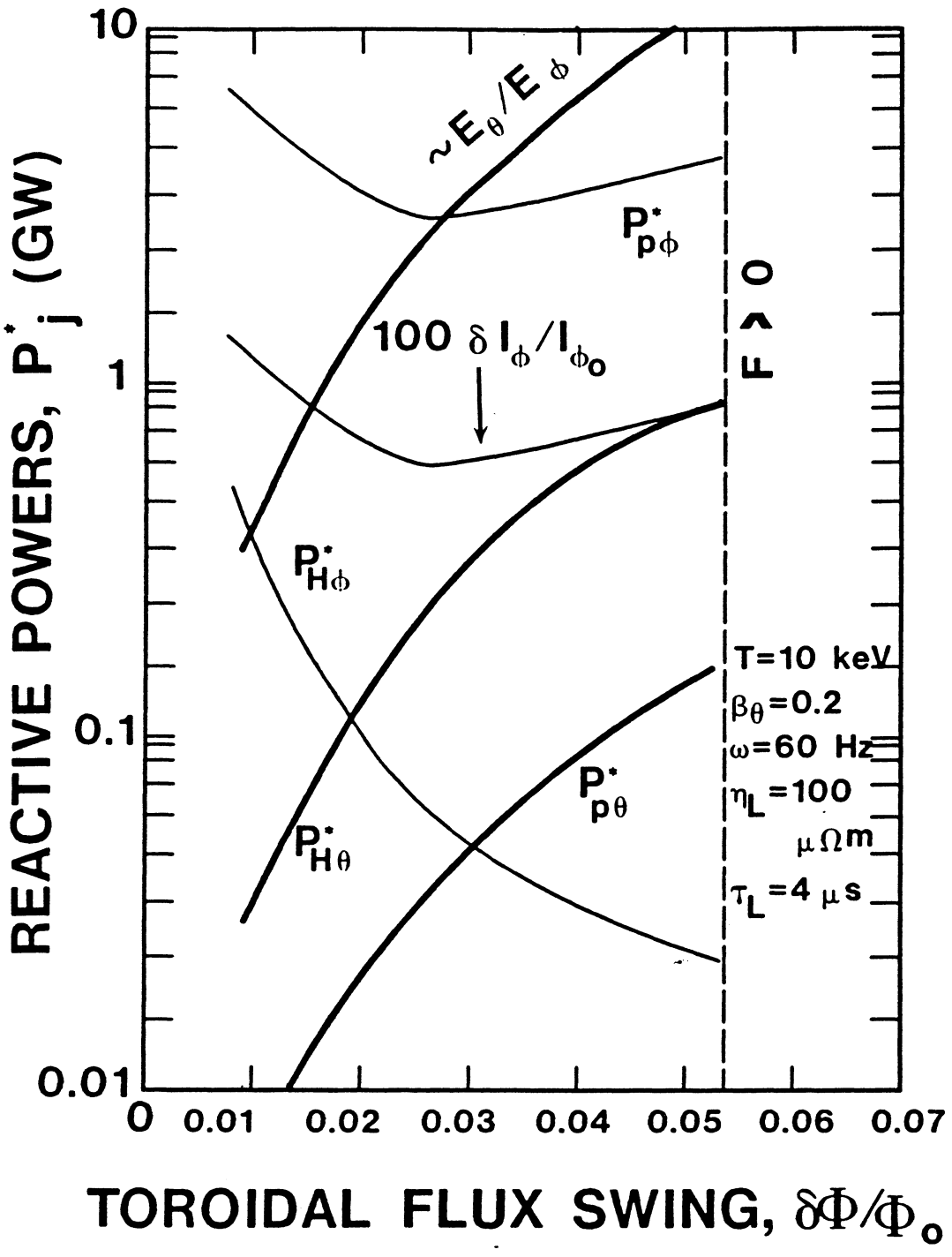


Fig. 4.6.-10. Reactive powers, relative electric fields, $E_\theta/E_\phi$, and plasma current swing as a function of the toroidal flux swing.

reversal is lost ($F > 0$). Lastly, Fig. 4.6.-11 gives the dependence of key OFCD parameters on the liner resistivity, with the point where the liner dissipation equals the plasma dissipation ($P_L = P_\Omega \simeq 8$ MW) being at $\eta_L \simeq 0.2$ $\mu\Omega$ m ($\eta_{cu} \simeq 0.018$ $\mu\Omega$-m). For the shell dimensions assumed (Table 4.6.-II), the time constant amounts to $\tau_L \simeq 7$ ms and the ohmic power density is ~ 100 MW/m$^3$ or ~ 50% of the local nuclear-heating power density for the $I_w \simeq 18$ MW/m$^2$ Strawman design.

4.6.2.3. Interim Conclusions

Although the foregoing models and analysis represent the first attempt to integrate circuit effects into the OFCD plasma modeling, the TITAN layout must be evolved further in other respects before a clear-cut assessment of design, power engineering, and magnetics problems can be made. This work remains for the next phase of the TITAN study. Nevertheless, the following interim observations and conclusions can be made.

- Inclusion of OFCD distorts wave forms and generates phase shifts, giving rise to complications, in that three iterative steps are required.

  - no net circuit volt-seconds, which requires an iteration on $V_{H\phi}$ (bias).

  - if $\frac{\delta\Phi}{\Phi_o} \cdot \frac{\delta V_\phi}{f_A I_\phi R_p} > 2$ an iteration for helicity balance is required.

  - circuit/plasma energy balance requires iteration on $f_A = R_p/R_p'$.

- Small plasma current swings ($\delta I_\phi/I_\phi \simeq 0.02$) are sufficient to drive steady-state currents in the 18-20 MA range with resistive powers in the plasma of ~ 8-10 MW.

- Large power flow past plasma surface (20-30 MJ at a frequency of 60 Hz), but the real power consumption is 8-10 MW.

- Total/circuit reactive power ratio is ~ 25, with $P^*_{p\phi} \simeq 4$ GW and $P^*_{H\phi} \sim 170$ MW; shielding of OHC/EFC may be required.

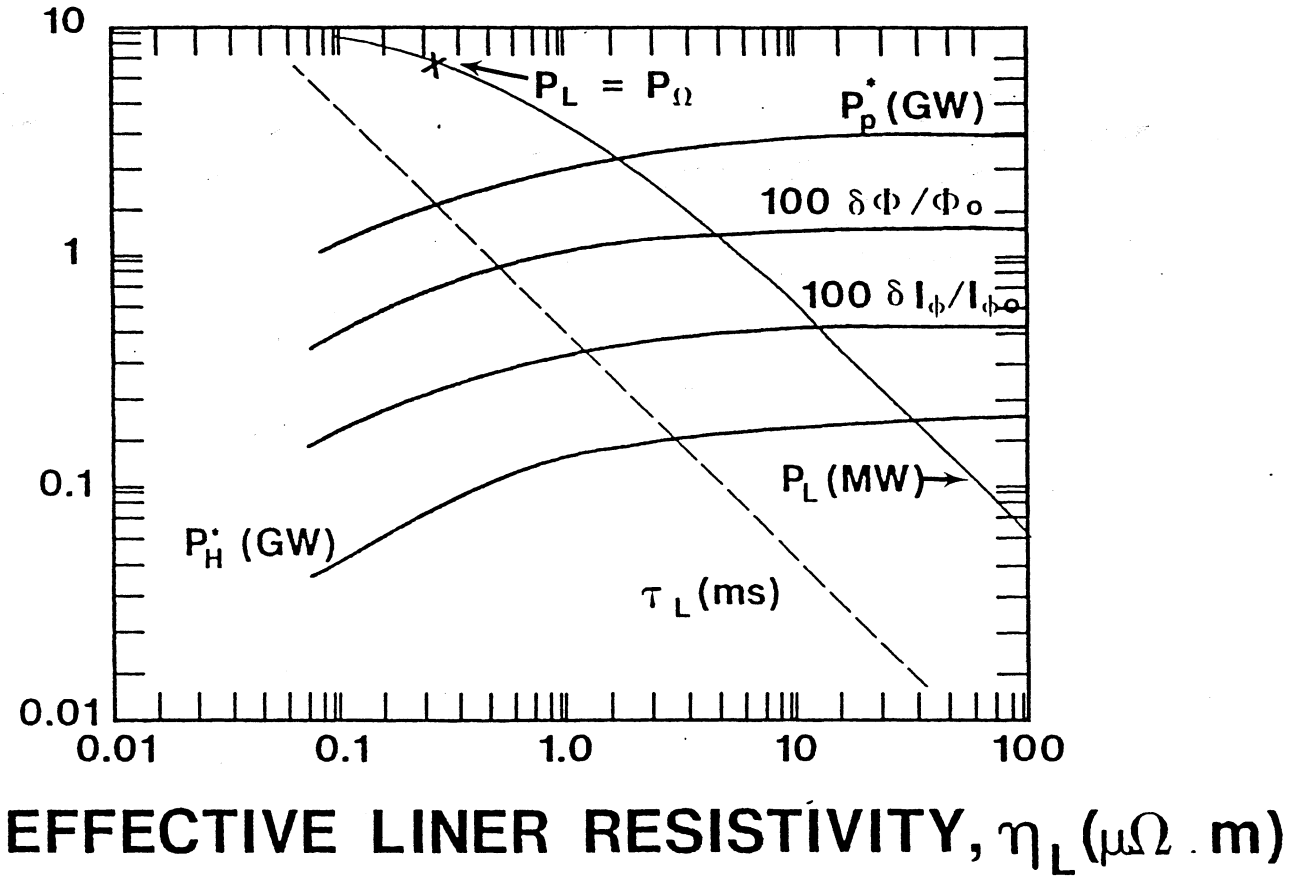


Fig. 4.6.-11. Dependence of OFCD reactive powers, liner dissipative powers, and flux and current swings on the liner resistivity ($\eta_L$ = 100 $\mu\Omega$ m base case).

- Liner resistance, $R_L \geq 2$ m$\Omega$ ($\tau_L < 1.3$ ms) is required to hold $P_L \leq P_\Omega \sim 8$ MW ($\sim 80$ MW/m$^3$ of liner). A larger $\tau_L$ leads to ohmic power density that exceeds nuclear heating ($\geq$ 200-300 MW/m$^3$). The design of an actual "shell" (i.e., liquid-metal cooled blanket, first-wall, shields, supports, gaps, penetrations) that gives required $R_L$ or $\eta_L$ may be a crucial issue.

- Energy flow across plasma surface (20-30 MJ) is small, but not negligible, compared with plasma kinetic energy ($\sim$ 10%). For example, the basecase conditions ($n = 4.35 \times 10^{20}$ m$^{-3}$, $T = 20$ keV, $r_p = 0.60$ m, $R_T = 3.9$ m, $p = 4.2$ MJ/m$^3$, $V_p = 27.7$ m$^3$), gives a total stored kinetic energy of $W_p = 230$ MJ. However, the energy flow associated with OFCD is negligible (1-2%) compared with plasma magnetic energy in that $\beta \simeq \beta_\Theta/2 \simeq 0.1$ and $W_B \simeq (2/3)W_p/\beta \simeq 1{,}530$ MJ. Finally, transfer occurs on a time scale ($\sim$ 60 Hz) that is 5-10% of $\tau_E$.

## 4.7. ONE-DIMENSIONAL CORE PLASMA SIMULATIONS

### 4.7.1. Model

A one-dimensional RFP plasma burn code, RFPBURN [81], has been used for

TABLE 4.7.-I

SUMMARY OF KEY FEATURES OF RFPBURN

- The code follows the time-dependent, cylindrical plasma evolution of ion and alpha-particle densities, ion and electron temperatures, and poloidal and axial (toroidal) magnetic fields.

- Physics constraints include Ohm's law, radial pressure balance and local quasi-neutrality.

- Physical terms include conduction, diffusion, convection, resistive dissipation, fusion reactions, impurity radiation based on a coronal equilibrium model, a volumetric ion source and/or a pellet injection model, and finally, a simple dynamo model which conserves helicity and allows the RFP configuration to be maintained in steady state.

- Boundary conditions consist of six regularity conditions at the origin ($r = 0$) and six wall conditions which include the toroidal magnetic field, the toroidal voltage, and either extrapolation endpoint or pedestal conditions on the densities and temperatures.

- Global plasma particle and energy balance is followed and used to check particle and energy conservation.

studying transport and other 1-D effects in the bulk plasma of the TITAN RFP reactor. Table 4.7.-I summarizes the key features of the RFPBURN code.

While the zero-dimensional plasma/circuits code BURN described in Sec. 4.5. is the main tool used to examine RFP reactor transients, RFPBURN supplements the 0-D model by examining 1-D aspects of local transport assumptions, impurity radiation with beta limits, pellet refueling, dynamo, and current drive. Additionally, RFPBURN can be coupled to the edge-plasma models to provide self-consistent core/edge-plasma boundary conditions. The 1-D results reported herein include: a) simulation of the parametric systems analysis design points and b) examination of a means to enhance radiative over transport losses in order to reduce erosion of the plasma-interactive components.

### 4.7.2. Results

For TITAN applications, RFPBURN has been used to study steady state burn conditions. The results are compared in Table 4.7.-II with the 0-D steady-state code results given in Sec. 4.5., and good agreement is found when in the 0-D model, flatter plasma density and temperature profiles are used relative to the Bessel-function profiles (Figs. 4.7.-1 and 2). The assumed transport coefficients are given by Eqs. (4.7.-1) to (4.7.-4) with $g(r) = 1$ and $\beta_{\theta c} = 0.19$ .

Experimental evidence on ZT-40M suggests that RFPs can operate at a soft beta limit [44,45], as discussed in Sec. 4.3. This characteristic of the RFP is in marked contrast with other confinement schemes such as the tokamak, where increasing the impurity content would increase the total energy loss rate and degrade the plasma pressure. Enhanced radiation from a (high) beta-limited plasma is important because it permits first-wall designs to receive a higher average (but more uniform) heat flux and to minimize the divertor (or limiter) power loads, thereby optimizing the overall design for the maximum power density while maintaining realistic engineering constraints on all systems.

The RFPBURN [81] one-dimensional transport model has been used to examine some of the properties of a beta-limited and radiation-dominated reactor-grade plasma. The radiation model assumes coronal equilibrium with the impurity density of the $j^{th}$ species, $n_j$, being specified by means of an impurity fraction, $f_j \equiv n_j/n_i$, where $n_i$ is the DT ion density. In order to incorporate a

TABLE 4.7.-II

COMPARISON OF 0-D AND 1-D PLASMA SIMULATION DESIGN POINT

| Parameter | 0-D | 1-D |
|---|---|---|
| Plasma minor radius, $r_p$ (m) | 0.6 | 0.6 |
| Plasma major radius, R (m) | 3.9 | 3.9 |
| Plasma average ion density, $n_i$ ($10^{20}$ $m^{-3}$) | 4.35 | 4.66 |
| Density peaking, $n_{i0}/n_i$ | 1.80 | 1.73 |
| Alpha-particle fraction, $n_\alpha/n_i$ | 0.053 | 0.042 |
| Ion temperature, $T_i$ (keV) | 20.0 | 20.7 |
| Ion-temperature peaking, $T_{i0}/T_i$ | 1.22 | 1.37 |
| Electron temperature, $T_e$ (keV) | 20.0 | 19.5 |
| Electron-temperature peaking, $T_{e0}/T_e$ | 1.22 | 1.19 |
| Global particle confinement time, $\tau_p$ (s) | 0.96(b) | 0.88 |
| Global energy confinement time, $\tau_E$ (s) | 0.24(b) | 0.29 |
| Lawson parameter, $n_i\tau_E$ ($10^{20}$ $s/m^3$) | 1.04 | 1.35 |
| Poloidal beta(a), $\beta_\theta$ | 0.221 | 0.218 |
| Plasma toroidal current, $I_\phi$ (MA) | 17.8 | 17.9 |
| Ohmic power in plasma, $P_\Omega$ (MW) | 8.0 | 8.1 |
| Fusion power, $P_F$ (GW) | 2.26 | 2.37 |
| Profile factors: | | |
| • DT reactivity, $g_{DT}$ | 1.43 | 1.28 |
| • Ohmic dissipation, $g_\Omega$ | 3.45 | 2.99 |
| • Bremsstrahlung, $g_{BR}$ | 1.33 | 1.24 |

(a) Includes thermalized alpha particles.

(b) Based on the empirical scaling (Sec. 5.2.1.) $\tau_{Ee} = C_\nu I_\phi^\nu r_p^2$ ($\nu = 1$, $C_\nu = 0.05$) and $\tau_p = 4\tau_{ce}$.

soft beta limit in a one-dimensional formulation, the transport coefficients were assumed with the following form:

$$K_e = K_{\perp e}^{cl} f(\beta_\theta) \qquad (4.7.-1)$$

$$K_i = K_{\perp i}^{cl} + K_e/4 \qquad (4.7.-2)$$

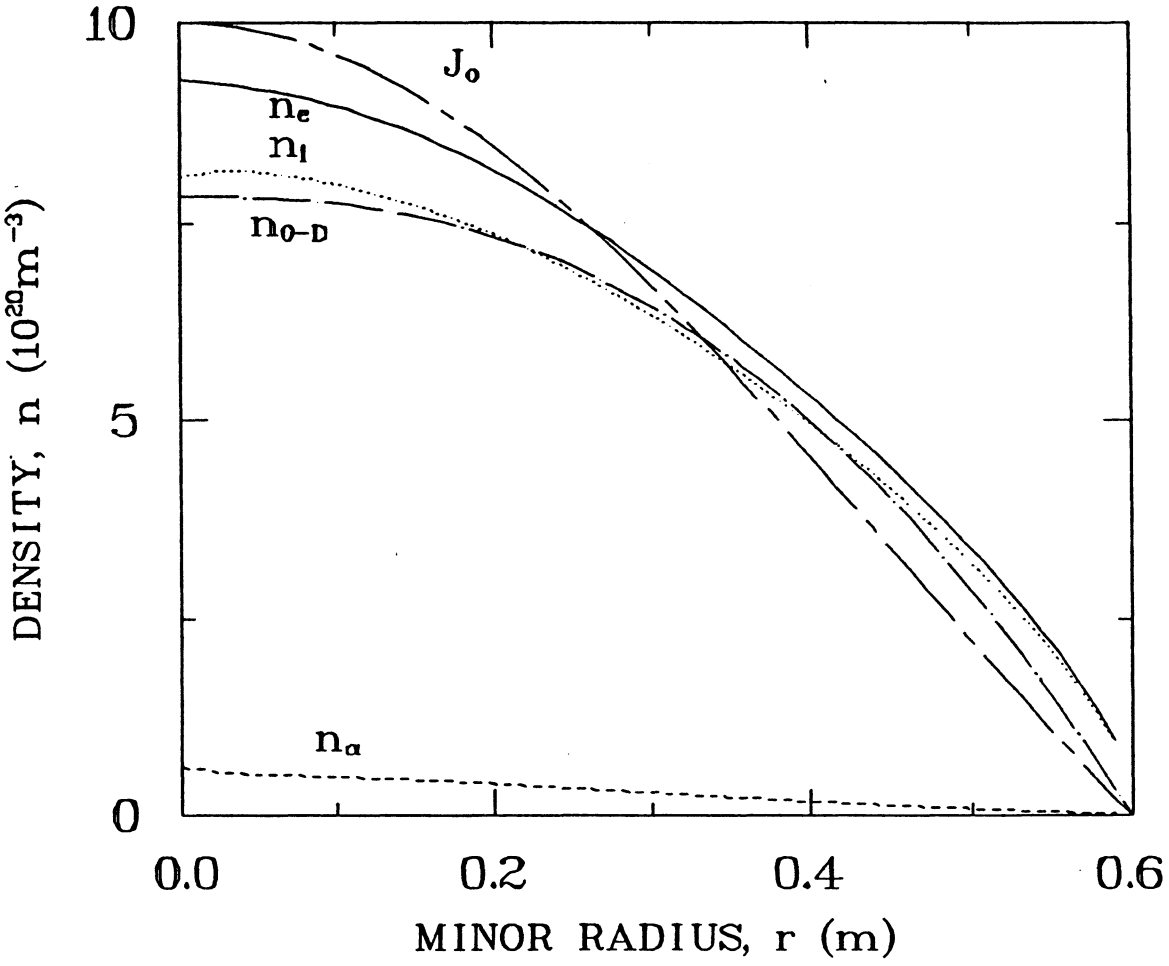


Fig. 4.7.-1. Comparison of O-D and 1-D radial density profiles.

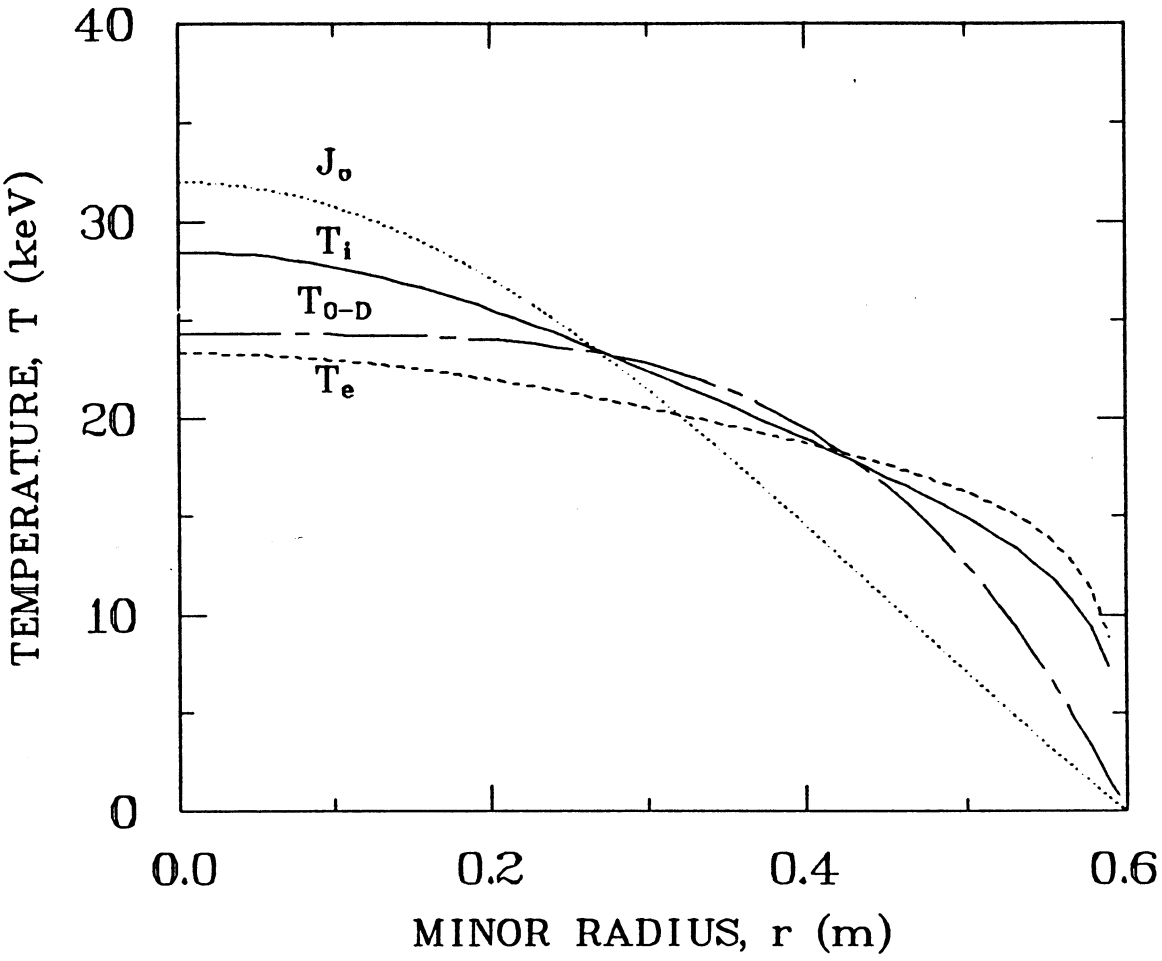


Fig. 4.7.-2. Comparison of O-D and 1-D radial temperature profiles.

$$D = D^{cl} [1 + 0.1f(\beta_\theta)] \qquad (4.7.-3)$$

where $K_\perp^{cl}$ and $D^{cl}$ are classical values of the cross-field thermal conductivity and particle diffusivity, and the following function $f(\beta_\theta)$ is used to model the observed soft beta limit:

$$f(\beta_\theta) = \begin{cases} 1 , & \beta_\theta \leq \beta_{\theta c} \\ \exp\left[\left(\frac{\beta_\theta}{\beta_{\theta c}}\right)^{15} - 1\right] \times g(r) , & \beta_\theta > \beta_{\theta c} \end{cases} \qquad (4.7.-4)$$

where,

$$g(r) = \begin{cases} 1 , & r > 0.84r_p \text{ or } \beta(0) \leq 0.11 \\ 1 + 10\left[1 - \left(\frac{r}{0.84r_p}\right)^2\right] . & \beta(0) > 0.11 \end{cases} \qquad (4.7.-5)$$

Here, the exponential factor represents the poloidal beta limit. The parabolic factor represents an enhanced internal transport and excludes highly peaked temperature profiles caused by highly-localized radiation losses. Such a factor would have a physical basis either if rapid transport occurs in the plasma core, possibly resulting from large scale m = 1 current-driven tearing modes, or if the global beta limit results from local beta limits. The model utilizes boundary conditions at $r_p$ which include the toroidal magnetic field and the toroidal loop voltage as well as extrapolation endpoint conditions for the density and temperatures.

The following computational results pertain to a typical RFP reactor plasma (listed in Table 4.7.-III), but are not to be taken as the most recent TITAN design parameters. The required impurity fraction for a given radiation

TABLE 4.7.-III

REACTOR CONDITIONS OF THE BETA-LIMITED 1-D TRANSPORT STUDY

| | |
|---|---|
| Plasma minor radius, $r_p$ (m) | 0.715 |
| Plasma major radius, $R_T$ (m) | 3.93 |
| Plasma toroidal current, $I_\phi$ (MA) | 18.0 |
| Plasma average ion density, $n_i$ ($10^{20}$ $m^{-3}$) | 8.67 |
| Critical poloidal beta, $\beta_{\theta c}$ | 0.19 |

TABLE 4.7.-IV

STEADY-STATE PLASMA PARAMETERS COMPUTED FROM THE 1-D MODEL

| Impurity | -- | C | Xe | U |
|---|---|---|---|---|
| $Z_j$ | -- | 12 | 54 | 92 |
| $f_j$ | 0.0 | $4\times10^{-2}$ | $1\times10^{-4}$ | $3\times10^{-5}$ |
| $Z_{eff}(0)$ | 1.04 | 2.0 | 1.3 | 1.15 |
| $\tau_E^{NR}$(s) | 0.64 | 7.9 | 1.2 | 1.8 |
| $\tau_E$(s) | 0.25 | 0.53 | 0.35 | 0.35 |
| $P_\alpha$(MW) | 336 | 233 | 306 | 321 |
| $f_{RAD}$ | 0.12 | 0.76 | 0.71 | 0.81 |

fraction is illustrated in Fig. 4.7.-3. Table 4.7.-IV summarizes key results for different plasma impurities.

For no impurities other than a ~4% alpha particle ash, a minimum $f_{RAD}$ = 0.12 is obtained. While low-Z impurities such as carbon can radiate the necessary power, a high impurity level ($f_j$ = 0.04) is required. For a given plasma beta and plasma current, such a large impurity level changes the shape of the plasma profiles and thus the fusion (alpha-particle) power, $P_\alpha$, as shown in Table 4.7.-IV. However, slight increases in $I_\phi$ result in large increases in $P_\alpha$, and therefore, design powers can be easily recovered with moderate (5%) increases in $I_\phi$. The fusion power can also be increased by trading off density with temperature. Such optimizations can best be done at the 0-D level of analysis. Also, the rather high value of $Z_{eff}$ = 2 for the carbon impurity would double the current-drive power requirements.

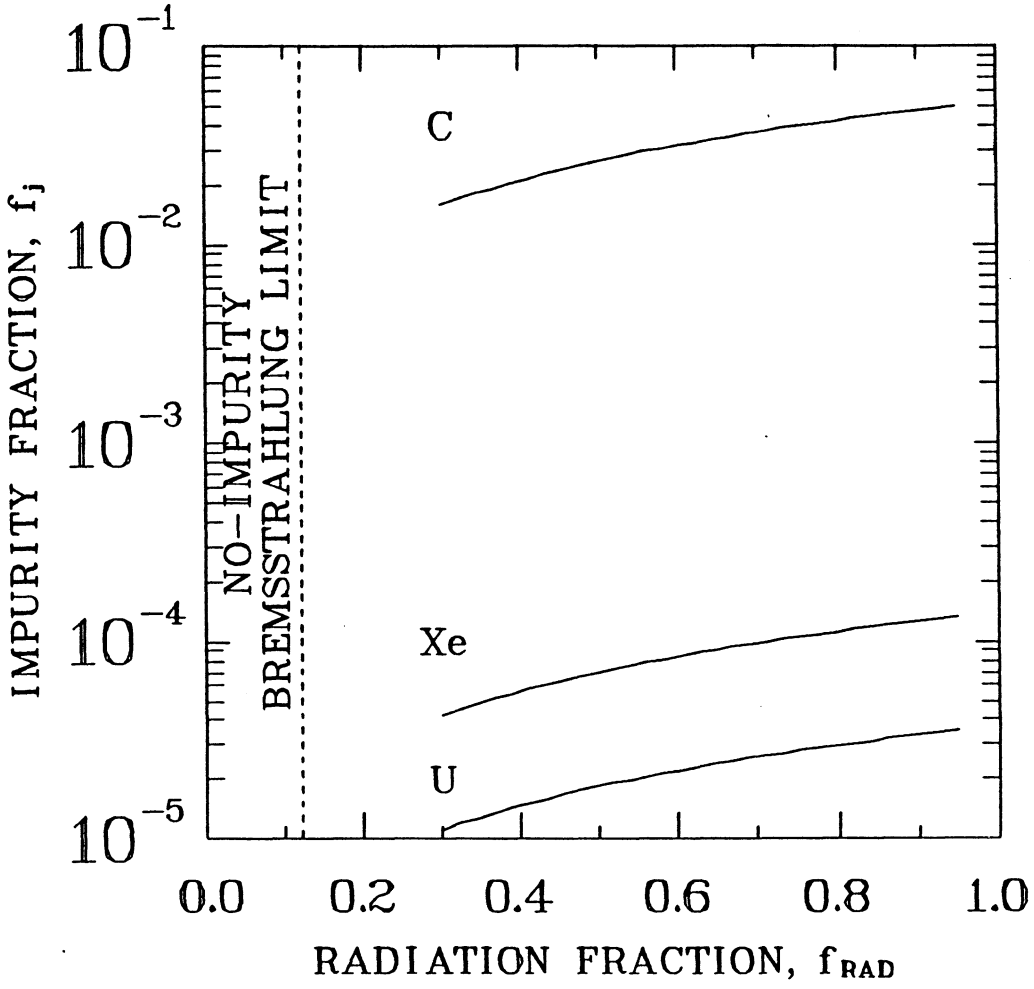


Fig. 4.7.-3. Impurity fraction versus radiation fraction for different impurities.

High-Z impurities such as xenon require a much smaller impurity concentration and produce lower values of $Z_{eff}$ (e.g., $Z_{eff}(0) = 1.3$ for Xe and the $Z_{eff}$ decreases with radius as $T_e$ decreases). Therefore, the high Z impurities are favored for enhancing the plasma radiation fraction.

The profiles of plasma parameters found by these 1-D simulations are uncertain since local transport is not known. But the highly localized radiative losses in the outer regions of the plasma are not expected to drastically change the plasma profiles if a local beta limit or some other source of rapid transport in the plasma core exists. It is noted that if the transport in the plasma core is too low, then high radiation losses at the plasma edge could result in a temperature collapse of the entire plasma column as the cold, radiating edge propagates inward.

Listed below are the major unknowns associated with assuming beta limits for RFP reactors. Even though a few of these issues may be partially addressed by 1-D analysis, the majority of the unknowns will require experimental demonstration at reactor conditions and, therefore will remain unknown for some time.

- $\beta$-limited confinement scaling in the reactor plasma regime.
- Limit on the local beta.
- The level and mechanism of the intrinsic transport.
- The collapse of the temperature profile due to impurity injection.
- The interaction of competing profile affects (e.g., refueling, alpha-particle transport, $T_i$:$T_e$:n split).
- The impact of the impurities on the edge-plasma and the wall (e.g., sputtering, wall buildup, vacuum and tritium systems).
- The effects of the impurities on the start-up transient.

Based on both experiment and theory, it appears feasible that RFP reactors can exhibit a soft $\beta$ limit. Such a $\beta$ limit was assumed in choosing the ZT-H experimental parameters [44]. If such $\beta$ limits exist, it may be possible to

adjust $f_{RAD}$ to any level between 0.12 and 0.95 with only a minor increase (10-30%) in plasma resistance by injecting high-Z impurities into the plasma core. Only small variations in the impurity fraction are required to significantly vary $f_{RAD}$. In practice, the maximum operating $f_{RAD}$ will be determined by the level of intrinsic transport. If the intrinsic transport mechanisms are classical, then the $f_{RAD}$ upper limit could be higher than 0.99. Finally, it is noted that the impurity fraction of Xe required for $f_{RAD} = 1$ in the plasma core is two orders of magnitude smaller than that required for $f_{RAD} = 1$ in the divertor chamber.

## 4.8. SUMMARY OF PHYSICS ISSUES AND FUTURE DIRECTIONS

The main physics areas that remain to be resolved before a viable commercial reactor can be based on the RFP are listed in Table 4.8.-I and summarized in the following subsections. Figure 4.8.-1 compares these issues and options with other confinement schemes, with the areas of transport, start-up and equilibrium/stability being combined under the general heading of plasma control.

### 4.8.1. Transport

The microscopic energy and particle confinement in present-day RFPs remain largely unknown, with global energy confinement for ohmically-heated discharges showing a dependence of the form $\tau_E \propto I_\phi^\nu$, where $\nu$ is in the range 0.8-1.5 and $I_\phi$ is the toroidal plasma current.

Simple energy balance on an ohmically heated plasma and the assumption of constant $I_\phi/N$ lead to the following expression:

$$\tau_{ce} = C_\nu \, I_\phi^\nu \, r_p^2 \, f(\beta_\theta) \ , \qquad (4.8.-1)$$

where $C_\nu$ is a fitting constant that is dependent on $\nu$, a soft beta limit has been assumed (prescribed by $f(\beta_\theta)$), and the global energy loss is generally ascribed to anomalous electron losses. In performing TITAN fusion core simulations, it is generally assumed that $\nu \simeq 1$, the ion particle confinement time, $\tau_{pi}$, equals four times $\tau_{ce}$, and the RFP operates at a beta limit with $f(\beta_\theta) = (\beta_{\theta c}/\beta_\theta)^m$ ($m$ = 6-8 and $\beta_{\theta c} \simeq 0.20$).

TABLE 4.8.-I

SUMMARY OF KEY PHYSICS ISSUES FOR THE RFP REACTOR

- Transport
  - Current, size, and beta scaling
  - Field errors, ripple, non-axisymmetry, magnetic islands
  - Radiative, beta-limiting, and intrinsic transport
- Heating
  - Efficient start-up and maximum use of dynamo
  - Ohmic to alpha-particle heating transition
  - Anomalous ion heating (start-up)
- Equilibrium and Stability
  - Control of terminations
  - Role of conducting shell (gaps)
  - Active (long-term) feedback
- start-up
  - Efficient breakdown and RFP formation ($E_\phi$, $B_v$, $B_{\phi o}$, $\tau_R$, $P_o$, ...)
  - Slow ramp-up to ohmic ignition
- Current drive (OFCD)
  - Management of reactive power (plasma, circuit)
  - Impact on dynamo
  - Impact on impurity control
  - Drive coils (location and impact on equilibrium control)
  - Alternatives
- Impurity control (divertor or limiter)
  - Value of the radiation fraction
  - Impact of non-axisymmetry
  - Particle loads (energy, power)
  - Pumping efficiency
  - Lifetime (erosion)
  - Heat load (peaking, asymmetries)
  - Magnetics (divertor)
    - -- connection length
    - -- flux compression/expansion
- Fueling
  - Edge-plasma refueling
  - Pellet penetration

Together, these assumptions and the sensitivity of the reactor design to these assumptions form the essential issues for plasma transport and confinement. Specifically, the size range of present-day RFPs is insufficient to establish a firm $r_p^2$ dependence, although a theoretical basis for such a dependence exists. Next, if the $I_\phi$ dependence of $\tau_{ce}$ is weaker than $\nu \simeq 0.8$, the impact during start-up on the OHC system becomes a concern. Finally, the RFP is assumed to operate at a beta limit. The transition of this beta-limited plasma scaling from ohmic to alpha-particle heating represents another unknown. As shown in Sec. 4.7.2., the RFP soft-beta limit permits operation with high radiation fractions. However, the level of intrinsic transport in the core plasma establishes an upper limit on $f_{RAD}$ and becomes an important issue.

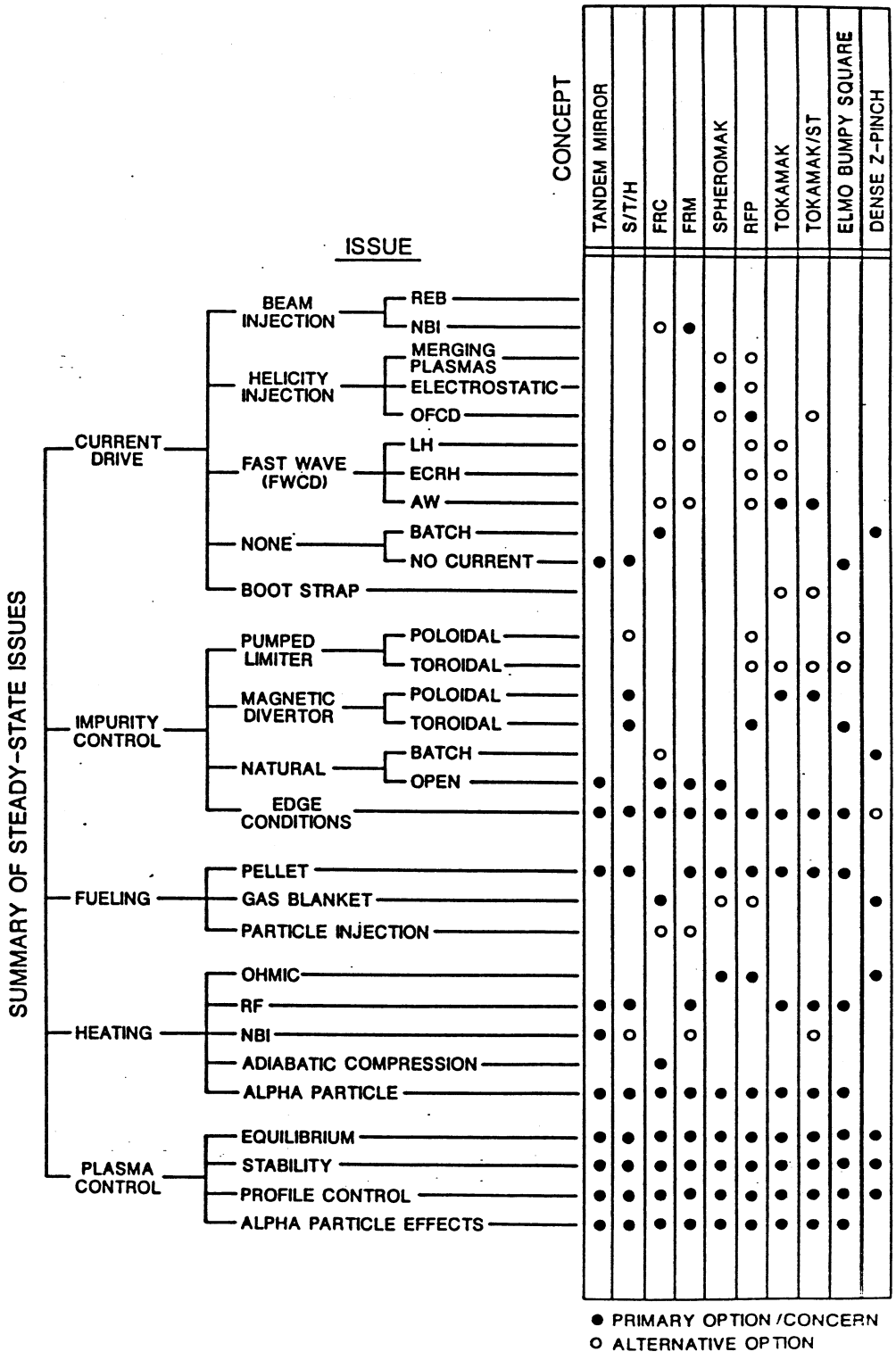


Fig. 4.8.-1. Summary of main physics issues and options for the RFP reactor and comparison with other confinement systems. Transport, start-up and equilibrium/stability are combined under plasma control.

Transport and confinement associated with non-intrinsic mechanisms related to magnetic islands, created by large-amplitude, (but high toroidal mode number) radial components of the magnetic field resulting from divertor coils or inadequately designed TFC sets, are also a concern that can generally be alleviated by careful design procedures. Furthermore, the nonuniformity of first-wall thermal heat load becomes a consideration in the context of maximum allowable field errors or ripples. This peaking of the first-wall heat load must be offset against the effect that island size has on the peak heat fluxes in the divertor, in that larger islands reduce peak heat fluxes in this region. From the viewpoint of electron runaway, the streaming parameter, $v_{TH}/v_D \propto (I_\phi/N)\ T_e^{1/2}$, must be monitored during early RFP formation/start-up, but becomes a minor consideration during the subsequent heating, ignition, and burn phases.

In summary, the developing RFP experimental database on transport and the observed strong current (or current-density) dependence is encouraging for an ohmically-heated and alpha-particle-sustained plasma. Furthermore, high-$f_{RAD}$ plasmas have been achieved in the laboratory, albeit the level of intrinsic transport and its scaling in these relatively low-temperature (300-500 eV) experiments are not known. The dimensional and beta dependence of confinement remains to be resolved, but most causes for degraded confinement in present experiments seem, in principle, to be under design control (e.g., field errors, wall interactions).

### 4.8.2. Heating

The plasma current density and resistivity envisaged for the RFP reactor, as for the experiment, generate a local ohmic power density that in magnitude cannot be matched by any form of auxiliary heating. The adoption of ohmic heating as the primary heating method, therefore, does not represent an intrinsic issue, but instead is related more to the previously described issue of transport and confinement. The currents that provide the intense ohmic heating in the RFP also provide the primary poloidal confining field at the plasma edge. The transition from the start-up ohmic heating in the outer regions of the core plasma to the more central alpha-particle heating expected during ignition and OFCD-sustained burn represents an uncertainty, particularly with respect to the relaxation time scale and overall efficacy of the RFP dynamo and its response to the OFCD.

In connection with start-up, it is becoming evident that the use of the dynamo to build-up the internal toroidal field is desirable to minimize the TFC power, energy, and stress during formation and the early start-up. Application of ohmic heating on a subsequent slow ramp that minimizes poloidal-flux consumption also represents an area where further optimization of the heating cycle is needed.

The degree of anomalous ion heating, as observed in some present-day RFP experiments, can also aid greatly in the early formation phases. As indicated earlier, the changing heating and $\mu$ profiles as the plasma moves from the ohmic-heating domain (8 MW and 0.3 $MW/m^3$ average heating at steady state, 56 MW and 2 $MW/m^3$ peak) to the alpha-particle heating phase (453 MW and 16.4 $MW/m^3$ average) with OFCD represents uncharted territory.

In summary, strong ohmic heating represents the hallmark of poloidal-field-dominated systems in general and the RFP in particular. While the combination of heating and confinement has distinct advantages in reducing system cost and complexity for both the commercial reactor and the experiment, the inability to separate heating and transport does reduce the information available from a given experiment. Nevertheless, it seems unlikely that auxiliary heating would ever compete or be used in the reactor, although some advantages of local heating and profile control by non-ohmic means may exist.

### 4.8.3. Equilibrium and Stability

Global stability has been expressed in the reactor study in terms of a beta limit, as is observed in many RFP discharges, and equilibrium is accurately described by the usual Shafranov theory. Probably the issues having the largest uncertainty and impact on the FPC engineering design are the need and constraints of a conducting shell that fits closely to the plasma.

The thickness (time constant) of this shell may impact the blanket tritium-breeding ratio and peak heat flux allowed and its geometry and uniformity dictate the degree and shape of gaps and penetrations. Also, the eddy currents induced in the shell affect the start-up transients and OFCD performance (field errors, power losses, phase shifts). In addition, the standoff distance between the plasma-core edge and the conducting first-wall shell establishes the maximum thickness of the scrape-off layer, and therefore, strongly impacts the characteristics of the plasma in the scrape-off layer and the efficacy of the divertor (open or closed) impurity-control scheme.

Another aspect of equilibrium and stability is the abrupt termination of the plasma current, which represents an area where better understanding and control is required, although great progress has been made. Given that the reactor plasma kinetic energy under steady-state burn conditions is ~ 150 MJ (1.5 $MJ/m^2$) and the magnetic-field energy amounts to 1.6 GJ, the means of current-termination control that have worked so well in present-day experiment (density control, toroidal-field ramp-down at constant reversal parameter, F) must be extended to the reactor regime. The impact of alpha-particle-driven plasma oscillations on transport (both fuel and ash), stability, beta limits, and the overall RFP dynamo is largely unknown.

In summary, the near-minimum-energy RFP has proven grossly stable and easily held in equilibrium, with local instabilities generally leading to turbulence, reduced plasma quiescence, and a general reduction in the confinement properties, rather than gross disruptions. Hence, like heating, equilibrium and stability are more closely associated with transport and confinement, rather than presenting a serious threat to the global plasma integrity (i.e., gross plasma disruption in present tokamak experiments).

### 4.8.4. Start-up

The TITAN study has examined the formation and start-up constraints for the reactor and their impact on the steady-state subsystem designs. For the first time, a wide range of experimental data and observed (but not necessarily fully understood) formation/start-up constraints have been applied to the reactor design.

There are similar limits on $E_\phi/P_o$ ($\geq 10^4$ V/m Torr) for both RFPs and tokamaks. Since filling-density limits for good RFP formation (i.e., adequate reversal, minimized poloidal-flux consumption) are higher than for tokamaks, higher values of $E_\phi$ are required to form the RFP. An initial current risetime in the range $\tau_{Ro}$ = 10-100 ms to achieve an initial (target) RFP of $I_\phi \simeq$ 0.2-0.4 MA with an expenditure of 3-30 Wb of poloidal-flux is suggested for an efficient matched-mode operation (i.e., constant toroidal flux). These parameters would be achieved using flux and energy expenditures determined by extrapolating the minimum RFP conditions derived from ZT-40 to a reactor which involves some level of uncertainty. This target-RFP plasma would then be subjected to a relatively fast current ramp (8-10 MA in a few seconds) to achieve 5-6 keV plasma and to minimize resistive poloidal-flux consumption. This fast ramp would be the result of a bipolar swing of the back-biased OHC. A

slower current ramp ($\geq$ 10 s) to ignition and burn ($I_\phi$ = 18-20 MA) would then be driven directly from the power grid.

The main issues remaining to be verified by subsequent experiment (RFX, ZT-H) include: a) scaling of minimum RFP conditions with $j_\phi$, $I_\phi$, $r_p$, etc.; b) the degree of electron runaway allowed upon formation; c) density control during RFP formation and during both fast (~ 1 s or ~ 10 MA/s) and slow ($\geq$ 10 s or 1 MA/s) current ramp-ups; d) optimal conditions for both burn-through upon RFP formation and subsequent mounting the $n\tau$ barrier just prior to ohmic ignition; e) the phasing of OFCD and impurity control systems during start-up, with the possibility of an OFCD assist to ignite and to reduce OHC design constraints (e.g., stresses); and f) the efficacy and power required of the EFC system, particularly during the early start-up phases. This last concern may require separate equilibrium control coils (resistive), located closer to the plasma, which could also provide EFC trim during OFCD.

In summary, the start-up procedure can have a strong impact in designing the steady-state RFP reactor, particularly the constraints imposed by the RFP formation and fast ramp-up (~ 1 s or ~ 10 MA/s) phases. Fortunately, a broad base of experimental evidence is available to contribute to the quantitative design of this aspect of the TITAN RFP, and most indications are favorable for achieving the ohmically ignited reactor burn at this time. During the formation and early start-up phase, power requirements, eddy-current generation, and equilibrium control may present some concerns.

### 4.8.5. Current Drive

Because of the higher resistance plasma and smaller physical size, an inductively pulsed compact RFP reactor would be sustained for a shorter period than a pulsed tokamak (100s versus 1,000s of seconds). Although not examined in detail, an inductively pulsed RFP must strive for reduced plasma resistance by increased minor radius and decreased major radius to an extent where superconducting TFCs and PFCs must be considered. A compact, high-power-density RFP reactor requires an efficient current-drive system.

Steady-state current drive by the phased oscillation of poloidal and toroidal fields (OFCD) has been adopted for the TITAN reactor design. Although some experimental and theoretical basis exist, substantial current driven by OFCD has not yet been demonstrated in the laboratory and, therefore, represents a main issue for the TITAN design. Given that the OFCD principle can be fully

demonstrated experimentally, the design of OFCD coils (e.g., location, sizes) and associated circuitry remains to be completed.

The drive coils can be located outside the FPC and can probably be incorporated as a subset of the main coil windings. Large reactive power flows across the plasma surface; however, the perturbation to the plasma (as measured in terms of field energy, magnetic field and current fluctuations, and fusion-power oscillations) is small. The impact of the driving field oscillations on the RFP dynamo, MHD behavior, and beta remain as unresolved issues. In addition, the maintenance of plasma equilibrium during the OFCD cycle, the impact of reactive power flows on the EFC, and overall energy balance remain to be resolved.

In summary, OFCD represents a large uncertainty for the compact RFP reactor, although preliminary experimental results from ZT-40 are encouraging [5,6]. Given that the OFCD principle of helicity injection is eventually proven in hotter RFP plasmas, several technological issues regarding the efficient application of OFCD to the reactor have to be examined. While this low-frequency (50-60 Hz) but high-reactive-power system appears to be achievable at a reasonable cost, the greatest concern at present is the losses related to eddy currents produced by the interactions of the drive-field with surrounding coils and structures. Furthermore, the requirements of the EFC system in maintaining gross equilibrium in the presence of OFCD have yet to be determined. An assessment of these uncertainties, however, must await a better resolved FPC design.

### 4.8.6. Fueling and Impurity Control

#### 4.8.6.1. Fueling

The high densities required for a compact RFP reactor make the fueling more difficult. Gas-puffing will probably not penetrate beyond the separatrix and pellet injection, therefore, is required. Deep pellet penetration into the center of the plasma, as for tokamaks, requires very high injection velocities (> 50-100 km/s). Pellet ablation by energetic alpha particles may further increase the injection velocity.

The strong poloidal currents flowing in the outer regions of the RFP also create the complication of curved pellet trajectories and a difficulty for these pellets to reach the plasma center. The generally high level of inner-plasma turbulence in RFPs, however, may allow low-penetrating pellets and near-edge

refueling to supply sufficient fuel to the plasma core. Thus, for an RFP, deep pellet penetration is not a likely requirement.

4.8.6.2. Impurity control

Given that an inductive batch-burn mode of operation is not possible for the economic, compact reactor concepts being examined by the TITAN study, an active means of impurity control is a major requirement for the design. Arrays of poloidal pump limiters or poloidally "symmetric" toroidal-field magnetic divertors are being considered, and the concerns of limiter erosion and possible plasma contamination have resulted in a focus on the magnetic divertor. As for OFCD, the viability of the magnetic divertor for the RFP must be based primarily on computational models, although a stronger experimental database exists from tokamak experiments that can better guide the edge-plasma modeling effort.

The main issues in this area with respect to the magnetics are the impact of introducing magnetic field pitch minima near the divertor coils and the creation of magnetic islands. With respect to the former, since a magnetic island (i.e., the separatrix) cannot reconnect through a coil, the potential stability problem related to pitch minima should not be a concern near the divertor. The impact of magnetic islands on transport, on the other hand, can be minimized through careful coil design.

The plasma models of the scrape-off layer indicate that high peak heat loads are to be expected on the divertor target and the injection of high-Z impurities into the divertor chamber has been investigated in order to cool radiatively the divertor plasma and reduce the peak heat load. A high impurity fraction ($\geq$ 1 % of the electron density for xenon) is required for this purpose, and it is essential that the impurity remains confined in the divertor with no contamination of the core plasma. Entrainment of the impurities in the background plasma flow may not be effective if the strong recycling at the divertor target near the separatrix creates a local reversal of the flow (as observed in fully two-dimensional edge-plasma models), tending to drive the impurities out of the divertor. In this case the feasibility of impurity injection for enhanced radiation in the divertor chamber would be seriously in doubt. In addition to this concern, a large uncertainty exists in the modeling of impurities in the scrape-off layer in terms of the lack of accurate data for the radiative cooling rate of high-Z impurities at low plasma temperatures.

A problem with the closed divertor chamber configuration is that compression of magnetic flux and poloidal asymmetries in the field-line density

lead to an additional peaking factor in the divertor heat load. A more open divertor configuration alleviates this effect considerably, although the proximity of the divertor plate to the core plasma in this case raises the possibility of interaction between the divertor and core plasma.

A quasi two-dimensional edge-plasma model, incorporating an analytic neutral particle model at the divertor target is being used to investigate the issues raised above. Radiation from high Z impurities in the scrape-off layer (arising from the injection of impurities into the core plasma to increase the radiation fraction in that region as well as from possible injection into the divertor) will also be included more fully in estimating the divertor heat loads. The open divertor configuration will be examined in detail, with particular emphasis placed on the transport of neutral particles in this geometry.

In summary, a wide range of active impurity-control schemes is available for the RFP, including high wall coverage (~ 50%) poloidal pumped limits, and a range of toroidal magnetic divertor configurations. Focus has been placed on magnetic divertors to control the edge-plasma characteristics and protect the first wall from erosion. A range of options exist to operate with a highly radiating core plasma and edge-plasma conditions that reduce heat flux peaking and wall erosion. The models needed to describe these processes are necessarily two-dimensional and, therefore, represent a development item. Preliminary indications are that a number of self-consistent solutions to the toroidal divertor impurity control scheme exist. These options primarily in the context of the open divertor configuration will be pursued during the design phase. In all cases, the compact RFP reactor approach requires a large fraction ($f_{RAD} > 0.8$) of the alpha-particle power to be radiated uniformly to the first wall and impurity control surfaces facing the plasma.

## REFERENCES


1. H. A. Bodin, R. A. Krakowski, and O. Ortolani, "The Reversed Field Pinch: from Experiment to Reactor," Fusion Tech. 10, (1986) 307.

2. J. B. Taylor, "Relaxation of Toroidal Plasma and Generation of Reversed Magnetic Fields," Phys. Rev. Lett. 33 (1974) 1139.

3. J. B. Taylor, "Relaxation of Toroidal Discharges," Proc. 3rd Topical Conf. on Pulsed High-Beta Plasmas, Abingdon (Sept. 1975), Pergamon Press, London (1976) 59.

4. C. W. Barnes, et al., to be published, Phys. Fluids, 29, (1986).

5. K. F. Schoenberg, C. J. Buchenauer, R. S. Massey, J. G. Melton, R. W. Moses, Jr., R. A. Nebel, and J. A. Phillips, "F-Θ Pumping and Field Modulation Experiments on a Reversed Field Pinch Discharge," Phys. Fluids 27 (1984) 548.

6. K. F. Schoenberg, C. P. Munson, D. A. Baker, R. F. Gribble, R. W. Moses, P. G. Weber, R. A. Nebel, and R. F. Scardovelli, "Oscillating-Field Current Drive Experiments on the ZT-40M RFP," Bull. Am. Phys. Soc. 31 (1986) 1547.

7. I. B. Bernstein, E. A. Frieman, M. D. Kruskal, and R. M. Kulsrud, "An Energy Principle for Hydromagnetic Stability Problems," Proc. Royal Soc. 244 (1958) 17.

8. V. D. Shafranov, "Plasma Equilibrium in a Magnetic Field, " Reviews of Plasma Physics, Consultant Bureau, New York, 2 (1966) 103.

9. B. R. Suydam, "Stability of Linear Pinch," Proc. of the 2nd United Nations Int. Conf. on the Peaceful Uses of Atomic Energy, Geneva (Sept. 1958), United Nations, Geneva 31 (1958) 157.

10. C. Mercier, "A Necessary Criterion for the Hydrodynamic Stability for an Axisymmetric Plasma," Nucl. Fusion 1 (1960) 47.

11. D. C. Robinson, "High-β Diffuse Pinch Configurations," Plasma Phys. 13 (1971) 439.

12. I. H. Hutchinson, "Plasma Resistance Studies in HBTX1A Reversed-Field Pinch," Proc. 11th European Conf. on Controlled Fusion and Plasma Physics, Aachen (Sept. 1984), European Physcial Soc. 1 (1983) 151.

13. D. C. Robinson, "Tearing-Mode-Stable Diffuse-Pinch Configurations," Nucl. Fusion 18 (1978) 939.

14. J. W. Conner and J. B. Taylor, "Resistive Fluid Turbulence and Energy Confinement," Phys. Fluids 27 (1984) 2676.

15. D. D. Schnack, E. J. Caramana, and D. C. Barnes, "Simulation of Current Ramp Operation in the Reversed-Field Pinch," Bull. Am. Phys. Soc. 30 (1985) 1399.

16. M. G. Rusbridge, "A Model of Field Reversal in the Diffuse Pinch," Plasma Phys. 19 (1977) 499.

17. M. G. Rusbridge, "Field line Reconnection and Density Fluctuations in ZETA," Plasma Phys. 22 (1980) 331.

18. A. R. Jacobsen and R. W. Moses, "Non-local DC Electrical Conductivity of a Lorentz Plasma in a Stochastic Magnetic Field," Phys. Rev. A 29 (1984) 3335.

19. Z. G. An, et al., "Role of Multiple Helicity Non-Linear Interaction of Tearing Modes in Dynamo and Anomalous Thermal Transport in Reversed Field Pinch," Proc. 10th Int. Conf. Plasma Phys. and Controlled Nuclear Fusion Research, London (Sept. 1984), IAEA, Vienna 2 (1985) 231.

20. S. Briguglio, F. Romanelli, G. Vlad, "Current Driven Drift Waves as a

Possible Mechanism for Dynamo Effect and Transport in Reversed Field Pinches," Nucl. Fusion 26 (1986) 1293.

21. D. C. Robinson and R. E. King, "Factors Influencing the Period of Improved Stability in ZETA," Proc. 3rd Int. Conf. on Plasma Phys. and Controlled Nucl. Fusion Res., Novosibirsk (Aug. 1968), IAEA, Vienna, 1 (1969) 263.

22. A. Buffa, et al., "First Results from the ETA-BETA-II RFP Experiment," Proc. 9th European Conf. on Controlled Fusion and Plasma Phys., Oxford (Sept. 1979), Culham Laboratory (1979) 544.

23. V. Antoni, et al., "Studies on High-Density RFP Plasmas in the ETA-BETA-II Experiment," Proc. 9th Int. Conf. on Plasma Phys. and Controlled Nucl. Fusion Res., Baltimore, MD (Sept. 1982), IAEA, Vienna, 1 (1983) 619.

24. V. Antoni, et al., "Reversed Field Pinch Plasma with Current Flat-Top in ETA-BETA-II," Proc. 10th Int. Conf. on Plasma Phys. and Controlled Nucl. Fusion Res., London (Sept. 1984), IAEA, Vienna, 2 (1985) 487.

25. K. Ogawa, et al., "Experimental and Computational Studies of Reversed-Field Pinch on TPE-1R(M)," Proc. 9th Int. Conf. on Plasma Phys. and Controlled Nucl. Fusion Res., Baltimore, MD (Sept. 1982), IAEA, Vienna, 1 (1983) 575.

26. Y. Hirano, T. Shimada, Y. Maejima, K. Ogawa, "Improved Stability Period in High-Current-Density Operation of Reversed-Field Pinch of ETL-TPE-1R(M)," Nucl. Fusion 22 (1982) 1613.

27. D. A. Baker, et al., "Performance of the ZT-40M Reversed-Field Pinch with an Inconel Liner," Proc. 9th Int. Conf. on Plasma Phys. and Controlled Nucl. Fusion Res., Baltimore, MD (Sept. 1982), IAEA, Vienna, 1 (1983) 587.

28. D. A. Baker, et al., "Experimental and Theoretical Studies of the ZT-40M Reversed-Field Pinch," Proc. 10th Int. Conf. on Plasma Phys. and Controlled Nucl. Fusion Res., London (Sept. 1984), IAEA, Vienna, 2 (1985) 439.

29. R. S. Massey, et al., "Status of the ZT-40M RFP Experimental Program," Proc. 6th Topical Meeting on the Tech. of Fusion Energy, San Francisco (Mar. 1985), Fusion Tech. 8 (1985) 1571.

30. H. A. B. Bodin, et al., Proc. 9th Int. Conf. on Plasma Phys. and Controlled Nucl. Fusion Res., Baltimore, MD (Sept. 1982), IAEA, Vienna, 1 (1983) 641.

31. P. Carolan, et al., "New Results from HBTX1A Reversed Field Pinch," Proc. 10th Int. Conf. on Plasma Phys. and Controlled Nucl. Fusion Res., London (Sept. 1984), IAEA, Vienna, 2, (1985) 449.

32. T. Tamano, et al., "Pinch Experiments in OTHE," Proc. 9th Int. Conf. on Plasma Phys. and Controlled Nucl. Fusion Res., Baltimore, MD (Sept. 1982), IAEA, Vienna, 1 (1983) 609.

33. T. Tamano, et al., "High Current, High Beta Toroidal Pinch Experiments in OTHE," Proc. 10th Int. Conf. on Plasma Phys. and Controlled Nucl. Fusion Res., London (Sept. 1984), IAEA, Vienna, 2 (1985) 431.

34. I. H. Hutchinson, et al., "The Structure of Magnetic Fluctuations in HBTX1A Reversed-Field Pinch," Nucl. Fusion 24 (1984) 59.

35. V. Antoni and S. Ortolani, "Characteristic of the Magnetic-Field Fluctuations in the ETA-BETA-II Reversed Field Pinch Experiment," Plasma Phys. 25 (1983) 799.

36. D. Brotherton-Ratcliffe, C. G. Gimblett, and I. H. Hutchinson, "Analysis of Internal Magnetic Fluctuations in HBTX1A Reversed Field Pinch," Culham Laboratory Report CLM-P742 (1985).

37. R. J. La Haye et al., "Measurements of Magnetic-Field Fluctuations in the OTHE Toroidal Pinch," Phys. Fluids 27 (1984) 2576.

38. G. A. Wurden, "Soft X-ray Array Results on ZT-40M Reversed Field Pinch," Phys. Fluids 27 (1984) 551.

39. V. Antoni and S. Ortolani, "Magnetic Field Fluctuation Studies on ETA-BETA-II," Proc. of the Workshop on Mirror-Based and Field-Reversed Approaches to Magnetic Fusion, Varenna (Sept. 1983), Monobypia Franchi, Perugia 2 (1984) 97.

40. A. R. Jacobsen and M. G. Rusbridge, "Observed Mechanism of Termination in ZT-40M Reversed Field Pinch," Los Alamos National Laboratory Report LA-9589-MS (Nov. 1982).

41. A. Newton, "Controlled RFP ramp-down," Culham Laboratory (to be published, 1986).

42. B. Alper, et al., "RFP Confinement Studies in ETA-BETA-II," Proc. 12th European Conf. on Controlled Fusion and Plasma Phys., Budapest (Sept. 1985), European Phys. Soc. 1 (1985) 578.

43. P. G. Weber, et al., "Results from the Los Alamos RFP Experiments," Proc. 12th European Conf. on Controlled Fusion and Plasma Phys., Budapest (Sept. 1985), European Physical Soc. 1 (1985) 570.

44. P. Thullen and K. Schoenberg (Eds.), "ZT-H Reversed Field Pinch Experiment Technical Proposal," Los Alamos National Laboratory Report LA-UR-84-2602 (1984) 26-28.

45. M. M. Pickrell, J. A. Phillips, C. J. Buchenauer, T. Cayton, J. N. Downing, A. Haberstich et al., "Evidence for a Poloidal Beta Limit on ZT-40M," Bull. Am. Phys. Soc. 29 (1984) 1403.

46. R. L. Hagenson, R. A. Krakowski, C. G. Bathke, R. L. Miller, M. J. Embrechts, N. M. Schnurr, et al., "Compact Reversed-Field Pinch Reactors (CRFPR): Preliminary Engineering Considerations," Los Alamos National Laboratory Report LA-10200-MS (August 1984).

47. D. Steiner, R. C. Block, and B. K. Malaviya, "The Integrated-Blanket-Coil Concept Applied to the Poloidal Field and Blanket Systems of a Tokamak Reactor," Fusion Tech. 7 (1985) 66.

48. J. M. Greene, J. L. Johnson, and K. E. Weimer, "Tokamak Equilibrium," Phys. Fluids 14 (1971) 671.

49. V. S. Mukhovatov and V. D. Shafranov, "Plasma Equilibrium in a Tokamak," Nucl Fusion 11 (1971) 605.

50. R. W. Moses, Jr., and J. K. Ballou, "Inductive Shielding for Pulsed Energy Storage Magnets," IEEE Transactions on Magnetics MAG-11 (1975) 493.

51. W. R. Smyth, Static and Dynamic Electricity, McGraw-Hill Book Company, NY (1939).

52. R. L. Spencer, "Magnetic Islands and Stochastic Field Lines in the RFP," Proc. RFP Theory Workshop, Los Alamos, NM (April 29 - May 2, 1980), Los Alamos National Laboratory Report LA-8944-C (Jan. 1982) 129.

53. C. Copenhaver, R. A. Krakowski, N. M. Schnurr, R. L. Miller, C. G. Bathke, R. L. Hagenson, et al., "Compact Reversed-Field Pinch Reactors (CRFPR): Fusion-Power-Core Integration Study," Los Alamos National Laboratory Report LA-10500-MS (Aug. 1985).

54. P. Thullen (ed.), "ZT-40U: Conceptual Design of a 2-MA Reversed-Field Pinch Experiment," Los Alamos National Laboratory document LA-UR-83-1375 (1983).

55. R. Hancox, R. A. Krakowski, and W. R. Spears, "The Reversed-Field Pinch Reactor Concept," Nucl. Eng. and Res. 63 (1981) 251.

56. R. A. Krakowski, R. L. Hagenson, N. M. Schnurr, C. Copenhaver, C. G. Bathke, and R. L. Miller, "Fusion-Power-Core Integration Study for the Compact Reversed-Field Pinch Reactor (CRFPR): A Follow-On Study," Nucl. Eng. and Design (to be published, 1986).

57. J. A. Phillips, L. C. Burkhardt, A. Haberstich, R. B. Howell, J. C. Ingraham, E. M. Little, K. S. Thomas, R. G. Watt, "ZT-40M Current Risetime Study," Los Alamos National Laboratory Report LA-9717-MS (October 1983).

58. P. Thullen (Compiler), "CPRF Specifications," Los Alamos National Laboratory Report LA-UR-85-3338 (March 1986).

59. C. G. Bathke, R. A. Krakowski, R. L. Miller, K. A. Werley, "Ignition, Burn, and Technology Tests in Reversed-Field Pinches," Los Alamos National Laboratory Report (to be published, 1987).

60. A. Kellman, E. Lazzaro, P. Noll, F. C. Schveller, and P. Thomas, "Breakdown Conditions in JET," Bull. Am. Phys. Soc. 30 (1985) 1524.

61. F. Engelmann, N. Fujisawa, B. B. Kadomtsev, V. I. Pistunovich, J. A. Schmidt, M. Sugihara, "Physics Design Basis, International Tokamak Reactor, Phase One," IAEA, Vienna (1982) 127.

62. R. G. Watt and J. N. Downing, "Pre-ionization Studies in ZT-40M," Los Alamos National Laboratory Report LA-9163-MS (February 1982).

63. J. A. Phillips, private communication, Los Alamos National Laboratory (August 1986).

64. D. J. BROWN, M. G. BELL, and J. CONNRAD, Proc. 10th Symp. on Eng. Probs. of Fusion. Res., IEEE No. 83CH/916-6-NPS (1983) 1233.

65. D. A. Baker, L. W. Mann, and K. F. Schoenberg, Nuc. Fusion 23 (1983) 380.

66. M. K. Bevir and J. W. Gray, "Relaxation, Flux Consumption and Quasi Steady State Pinches," Proc. RFP Theory Workshop (April 28 - May 2, 1980), Los Alamos National Laboratory Report LA-8944-C (January 1982) 186.

67. J. B. Taylor, "Relaxation and Magnetic Reconnection in Plasma," Rev. Mod. Phys. 58 (1986) 741. Also UKAEA Culham Laboratory Report CLM-P76 (December 1985).

68. R. Nebel, private communication, Los Alamos National Laboratory (1980).

69. D. D. Schnack, E. J. Caramana, and R. A. Nebel, "Three-Dimensional

Magnetohydrodynamic Studies of the Reversed-Field Pinch," Phys. Fluids 28 (1985) 321.

70. E. J. Caramana, R. A. Nebel, and D. D. Schnack, "Nonlinear, Single-Helicity Magnetic Reconnection in the Reversed-Field Pinch," Phys. Fluids 26 (1983) 1305.

71. H. P. Furth, "Non-ideal Magnetohydrodynamic Instabilities and Toroidal Magnetic Confinement," Phys. Fluids 28 (1985) 1595.

72. R. Gross, Fusion Energy, p. 118, Wiley and Sons, NY.

73. D. A. Ehst, J. N. Brooks, Y. Cha, K. Evans, Jr., A. Hassaein, S. Kim, et al., "Tokamak Burn Cycle Study," Argonne National Laboratory Report FPP/TM-178 (November 1983).

74. N. J. Fisch and C. F. F. Karney, "Current Generation with Low Frequency Waves," Phys. Fluids 24 (1981) 27.

75. Yan Ming Li, "Alfvén Waves in the Presence of Alpha Particles - Stability, Heating, and Current Drive," Doctoral Dissertation, University of Texas at Austin, 1984.

76. R. L. Miller, R. A. Krakowski, C. G. Bathke, C. Copenhaver, N. M. Schnurr, A. G. Englehardt, T. J. Seed, and R. M. Zubrin, "Advanced Tokamak Reactors Based on the Spherical Torus (ATR/ST): Preliminary Design Considerations," Los Alamos National Laboratory Report LA-10740-MS (June 1986).

77. R. A. Demirkhanov, A. G. Kirov, L. F. Ruchko, and A. V. Sukachev, "Generation of Steady-State Currents and Transfer Control in a Toroidal Magnetic Trap due to Alfvén Waves," JETP Letters 33 (1981) 28.

78. Y-K. M. Peng, "Spherical Torus, Compact Fusion at Low Field," Oak Ridge National Laboratory Report ORNL/FEDC-84/7 (January 1985).

79. D. A. Ehst, "Relativistic Electron Beam Current Drive," in "FED-A, An Advanced Performance FED Based on Low Safety Factor and Current Drive,"

Y-K. M. Peng, P. H. Rutherford, et al., Oak Ridge National Laboratory Report ORNL/FEDC-83/1, Sec. 4.5. (August 1983).

80. A. Mohri, K. Narihara, Y. Tomita, T. Tsuzuki, M. Hasegawa, and K. Ikuta, "Experiment on Plasma Confinement by Long-Lived Intense Relativistic-Electron-beam Ring," IAEA 8th Int. Conf. on Plasma Phys. and Cont. Nucl. Fusion Res., Brussels, I (1980) 511.

81. K. A. Werley, "Stable Alfven Wave Dynamo Action in the Reversed Field Pinch," Ph.D. Thesis, Nucl. Eng. Program, Univ. of Ill. (1984).

82. G. A. Wurden, private communication, Los Alamos National Laboratory (1986).